ADMITTANCE CHARACTERISTICS OF MIS AND SIS STRUCTURES

ADMITTANCE CHARACTERISTICS OF METAL-INSULATOR-SEMICONDUCTOR (MIS) AND SEMICONDUCTOR-INSULATOR-SEMICONDUCTOR (SIS) STRUCTURES

By

VICTOR ALBERT KEITH TEMPLE, B.Sc., M.Eng.

A Thesis
Submitted to the School of Graduate Studies
in Partial Fulfilment of the Requirements
for the Degree
Doctor of Philosophy

McMaster University
February 1972

DOCTOR OF PHILOSOPHY (1972)
(Physics)

McMASTER UNIVERSITY
Hamilton, Ontario

TITLE: Admittance Characteristics of Metal-Insulator-Semiconductor (MIS) and Semiconductor-Insulator-Semiconductor (SIS) Structures

AUTHOR: Victor Albert Keith Temple, B.Sc. (Eng. Phys., U. of Man.),
M. Eng. (Elec., McMaster University)

SUPERVISOR: Professor J. Shewchun

NUMBER OF PAGES: xiii, 180

SCOPE AND CONTENTS:

This work presents theoretical calculations of some of the most important electrical characteristics of thin film, insulator-dominated semiconductor devices. Solutions of prespecified accuracy for an a.c. transmission line model of the semiconductor in such configurations as the MIS (Metal-Insulator-Semiconductor) structure and the SIS (Semiconductor-Insulator-Semiconductor) structure are given. Together with an accurate solution of the d.c. bias problem, exact C-V (Capacitance-Voltage) and G-V (Conductance-Voltage) characteristics can be found at any frequency. SRH (Shockley-Reed-Hall) impurity centres and surface states have been included in both the d.c. and a.c. solutions. In addition, accurate studies of the low temperature dopant impurity response can be made since the d.c. solution uses full Fermi integrals over arbitrary densities of states with the impurity dopant band treated like an SRH centre for the a.c. solution.

In non-equilibrium situations, such as those which occur with the application of light or carrier injection by tunnelling, the a.c.

solution requires active elements in the transmission line model but the transmission line can still be solved to a prespecified accuracy provided an accurate solution of the d.c. bias problem can be found. In this thesis the d.c. solution for the case of light-induced pair production is considered under the assumption of bulk controlled d.c. quasi Fermi level shifts. Thus the accuracy of the related a.c. conductance and capacitance solutions is dependent on the reliability of this assumption.

The detailed treatment of the a.c. admittance of the MIS structure is justified by its technological importance and fundamental insight gained on impurity centre and surface state effects.

The other work presented in this thesis is devoted to a study of a new thin film device structure, the SIS diode. First, the a.c. admittance characteristics for the thick insulator case are predicted to a prespecified accuracy. Then a simple treatment for part of the SIS d.c. tunnelling problem is done to qualitatively predict the effects of such parameters as doping density, temperature and insulator thickness on current-voltage characteristics. Finally, a simple generalization of the a.c. transmission line to include the effects of tunnelling is given which allows accurate solution for the a.c. admittance of tunnelling SIS diodes if the complete d.c. non-equilibrium problem can be accurately solved.

Practical application of the thick-insulator SIS diode will undoubtedly stem from its wide range of interesting low and

high frequency response characteristics. Among the most interesting of these characteristics is a bell-shaped high frequency C-V response previously unobserved in other two terminal devices.

An interesting negative resistance feature, which partly resembles the negative resistance region of the p-n junction tunnel diode, is analyzed for the degenerate SIS p-i-n thin insulator structure. While the thick insulator SIS device has recently been fabricated and the bell-shaped high frequency response experimentally observed, experimental verification of the tunneling characteristics of the SIS diode has as yet not been fully realized.

ACKNOWLEDGMENTS

Dedicated to Carol, Shannon and Merilee

I want to express my appreciation to my supervisor, Dr. J. Shewchun, for his guidance and editorial efforts in producing this thesis.

I thank fellow students, R. Clarke, E. Jones and P. Swart for providing contact with experiment.

I am also grateful for the financial support provided by the National Research Council of Canada.

TABLE OF CONTENTS

LIST OF FIGURES

Figure Page

LIST OF TABLES

CHAPTER I

INTRODUCTION

The aim of this work was to provide theoretical support for experimental thin film, insulator dominated semiconductor device studies. The first part of this thesis, Chapter II, deals with the solution of what will be called the "d.c. problem". Under thermal equilibrium, and with thick oxides preventing sizable d.c. currents, this reduces to a solution of Poisson's equation. An improved solution of Poisson's equation is presented with an application to the low frequency C-V analysis of the usual MIS (Metal-Insulator-Semiconductor) and to the little known SIS (Semiconductor-Insulator-Semiconductor) structures.(1)

The second part of this thesis, Chapters III and IV, deals with the "a.c. problem" and presents an exact solution of the small signal a.c. admittance of both the MIS and SIS devices. This is accomplished by the use of an electrically equivalent model of the small signal a.c. transport equations, ie. a transmission line. This approach was first proposed by C. T. Sah(2) with the first general and accurate solutions given by Temple and Shewchun.(3) Several interesting features are considered in this part including the effect of SRH (Shockly-Reed-Hall) generation -- recombination centre effects, some low temperature ($\sim 50°K$), high doping density effects and finally one or two examples of a non-equilibrium system with light stimulated hole-electron pair creation. Naturally the important effects of surface states at the interface and charge in oxide (insulator) have been included in both the d.c. and a.c. solutions.

The third part of this thesis, Chapters V and VI, gives a simple derivation of the various d.c. tunnelling currents in the SIS thin insulator structure modelled after solutions available (or suggested) for the MIS Case. The tunnelling program can be solved in either the W.K.B. or the wave function matching (WFM) modes and includes surface state tunnelling. MIS tunnelling currents can be calculated as a special case but no I-V curves will be given here as a number of such calculations have been previously published. The solution is necessarily simple to allow calculation of d.c. tunnel current dependence on such parameters as temperature, doping density, and insulator thickness. Hence the characteristics presented in Chapter VI cannot be expected to give much more than a qualitative prediction SIS tunnel diode behavior. Nonetheless, the calculations do include such refinements as a simple two band model for barrier propagation, image force barrier modification and semiconductor space charge region tunnelling.

Chapter VII presents a modification of the a.c. transmission model of both the MIS and SIS structure to include tunnelling paths through the insulator. As in the thick insulator case, the a.c. C-V and G-V characteristics can be calculated to a prespecified accuracy provided a complete and accurate solution of the d.c. problem can be obtained. No such solution is available. Hence no thin insulator C-V and G-V a.c. characteristics are given. Note however, that for d.c. tunnelling currents too small to appreciably disturb the semiconductive charge densities, one might use the approximate solution described in Chapters V and VI to establish the required transmission line element values.

CHAPTER II

THE D.C. BIAS PROBLEM AND THE LOW FREQUENCY MIS AND SIS C-V CHARACTERISTICS

1. Introduction to the D.C. Problem

MIS C-V characteristics have been extensively used in the investigation of interface surface surface states(4,7-9,17-20). By comparing experimental admittance curves with curves calculated from the solution of the ideal device, the properties of the insulator semiconductor interface can be inferred.

When a given static voltage is applied across the device, a portion of this voltage appears across the oxide and the remainder across the semiconductor. The voltage across the semiconductor results in energy band bending in the semiconductor which is a maximum at the insulator-semiconductor interface and zero in the bulk semiconductor for a sufficiently long semiconductor. The corresponding charge density variations must obey Poisson's equation for the semiconductor in thermal equilibrium.

Although MIS characteristics have been extensively studied, the methods employed in solving Poisson's equation for these MIS theories have varied considerably in accuracy and generality. None have been extended to other insulator capacitor systems such as the SIS system.

In Chapter II of this thesis, an improved solution of Poisson's equation is discussed and both MIS and SIS curves are obtained using this method.

The most widely used solution of Poisson's equation is that of Kingston and Neustadter(13). Their solution is applicable to bandgap materials with a uniform doping density and assumes that: 1) all impurity sites are ionized and 2) the hole and electron concentrations can be approximated by Boltzmann statistics. By using the intrinsic Debye length, semiconductor distance is made dimensionless and the results are given as families of curves showing the field-potential and potential-distance relationships. Each impurity concentration requires a separate curve. Several authors(14-16) have extended this solution in various ways, but all have used uniformly doped semiconductors with the same two assumptions as Kingston and Neustadter.

The solution used in this work makes those assumptions unnecessary by using the full Fermi statistics for the electron, hole, and impurity bands. It is now possible to obtain an accurate solution of Poisson's equation for the class of doped materials in which the assumption of all impurity sites ionized was invalid. The present technique yields solutions which are valid over a greatly extended range of applied voltage since it can handle the situation with the valence or conduction bands bent through the Fermi level.

In addition, since hole and electron densities are obtained by integration over the respective bands, one can use actual densities of states rather than the usual parabolic approximation. Other positive features of this solution include the following.

(i) Preset accuracy over all ranges of d.c. bias where the d.c. current does not greatly affect the equilibrium condition.

(ii) The inclusion of Fermi statistics and a density of states in the conduction and valence bands. This includes band tailing effects using the equations and procedures as outlined in reference 25 and covers such cases as occur in degenerate semiconductors where the majority carrier and impurity bands merge into a single band.

(iii) Applicability at any temperature provided the correct energy band parameters are available.

(iv) The inclusion of any number of impurity bands each having an arbitrary density of states and obeying Fermi statistics. In this thesis each impurity band will be either Lorentzian (specified by central energy, line width, and density of states) or Gaussian(25). If Gaussian, the density of states function is given in terms of the impurity density by an equation of the form(25).

$$g(E) = A \exp (-E-E_{imp})^2/2\sigma^2 \qquad (1)$$

where σ is the Gaussian variance in eV, and E_{imp} the energy of the impurity band in eV.

(v) The inclusion of any number of surface state bands at the oxide-semiconductor interface and the inclusion of any amount of fixed or static charge at arbitrary distances into the oxide.

The importance of allowing for an impurity band density of states and Fermi statistics will be evident in Chapter III, Section 6, where several low temperature, high doping density structures are considered. It will be seen that, at low temperatures, the capacitive contribution due to impurity band charging and may result in a discernable impurity band capacitance bump.

A further generalization of the d.c. solution to include any number of impurity bands was influenced by the problems associated with the cadmium sulfide MIS system which is reported to have at least nine densely populated impurity trap levels(31) in addition to donor and acceptor levels.

The first sections of this chapter briefly describe the solution method and then tests it be examining several MIS systems with various surface-state distributions, semiconductor impurity concentrations, and temperatures.

The last sections of this chapter give results for several SIS systems for different surface-state distributions and impurity concentrations. Naturally, the low-frequency C-V curves are more complicated than the corresponding MIS curves and, therefore, less useful as an investigative tool for surface phenomena. However, as parametric capacitors, such devices may be of significant importance since their responses can be quite different both at low and high frequencies from the normal MIS capacitor. In addition, with thin insulators one might expect to find SIS tunneling behavior(12) which would be interesting enough in itself to warrant the extra effort required in making an SIS device.

2. Solution of Poisson's Equation

Analysis of nonmetallic capacitors at one stage or another requires the solution of Poisson's equation,

$$\frac{d^2\psi(x)}{dx^2} = \frac{e\rho(x)}{\epsilon kT}, \tag{2}$$

where $\psi = -eV/kT$ is a convenient unit of band bending or electrostatic potential, ρ is the charge density, ϵ is the dielectric constant, and e is the electronic charge.

Given the densities of states $g_i(E)$ and $g_j(E)$ of the electron and hole bands with Fermi functions f_i and f_j, then for band bending $\psi(x)$ at distance x from the interface, the total charge density can be written as

$$\rho(x) = \sum_i \rho_i + \sum_j \rho_j + \rho_{imp} \tag{3}$$

where i sums over conduction bands and j over valence bands, and ρ_{imp} is the charge density of the ionized impurity. $\rho(x) = 0$ establishes the position of the Fermi level for zero applied bias.

Writing the charge in the i^{th} band as an integration over energy, the total conduction band contribution to the charge density ρ_c becomes

$$\rho_c(x) = -e \sum_i \int g_i(E) f_i(E,\psi) dE. \tag{4}$$

Similarly, the total valence band contribution to the charge density ρ_v becomes

$$\rho_v(x) = e \sum_j \int g_j(E) f_j(E,\psi) dE. \tag{5}$$

Finally, the total charge density for the impurity bands can be written as

$$\rho_{imp} = e \sum_i \int g_i(E) f^i_{imp}(E,\psi) dE. \tag{6a}$$

For a system in the depletion region equation 6a generally can be approximated as

$$\rho_{imp}(x) = e \sum_i N^i_{imp}(x) \tag{6b}$$

where $N^i_{imp}(x)$ is the impurity concentration expressed as a polynomial in x of the i^{th} impurity level.

In the semiconductor system, the expression for the charge density ρ is sufficiently complex that the only general specified-accuracy solution is the numerical one(1-4). However, regions of exact analytic solution do exist(5), and to keep computer time and core storage to a minimum and improve accuracy, these should be used wherever appropriate, and then joined by numerical solutions over regions where their accuracy fails.

Hence analytic solutions of Poisson's equation are established in three regions.

Region 1:

$$\rho = \rho_{imp}(x) \tag{7}$$

where $\rho_{imp}(x)$ is given in equation (6b).

Region 2:

$$\rho = k_1 \exp[-k_2\psi(x)], \tag{8a}$$

Region 3:

$$\rho = k_1 \exp[+k_2\psi(x)], \tag{8b}$$

with k_1 real and k_2 real and positive.

Region 1 is the usual depletion region where the charge density can be closely approximated by the impurity doping density. For the region of band bending where this approximation is accurate, $\psi(x)$ is then obtained by integrating ρ twice.

Regions (2) and (3) are regions of moderate accumulation or inversion where the Fermi functions in the valence or conduction band integrals (3) and (4) can be represented by exponentials, and the charge density contribution from the ionized impurity is small enough to be neglected. Thus in regions (2) and (3) the charge density can be represented by a single exponential with the closed-form solutions given by Hauser and Littlejohn(5) as in (9):

$$\psi(x) = \frac{1}{k_2} \ln \{A^2 \sec^2[A(B+\sqrt{|k_1|}\; x)]\} \tag{9a}$$

$$\psi(x) = \frac{1}{k_2} \ln \{A^2 \operatorname{csch}^2[A(B+\sqrt{|k_1|}\; x)]\} \tag{9b}$$

Where the charge density cannot be approximated by (7) and (8), a form of numerical solution is required. For example, in a p-type semiconductor, regions of numerical solution are used:

1) In heavy inversion where the conduction band is close enough to the Fermi level (or below the Fermi level) to invalidate the exponential approximation to the conduction band Fermi functions.
2) Between the inversion and depletion regions where the charge density is the sum of an exponential function (of voltage) contribution from the conduction band and a constant due to the ionized impurities.
3) As the impurity band passes through the Fermi level, the ionized impurity charge contribution may require the full Fermi function in a heavily doped material. (Note that should numerical region

(3) be required it will often coincide with numerical region (4) below.)

4) At flatband when the contributions of the hole, electron, and impurity bands yields a complicated expression for charge density which requires numerical solution.

5) In heavy accumulation where the valence band is near or below the Fermi level.

In these regions of numerical solution, the charge density ρ is approximated by a staircase function, and ψ is obtained by integrating twice. In such a joining region, ψ is continuous with a continuous first derivative. It is in fact composed of a series of parabolas, each increasing the band bending ψ by an amount $e/\eta kT$ where η is a large integer. By setting the value of η, the accuracy in the joining region can be prescribed, and by increasing the width of the joining region, the upper bounds of the error introduced by using charge approximations (1), (2), or (3) can be lowered.

3. Low Frequency MIS Capacitence

To calculate the value of capacitance, a value of interface band bending $\psi(0)$ must first be assumed. The $\psi(x)$, $x = 0$ to $x \to \infty$ which satisfies this boundary condition is found by solving Poisson's equation. Knowing $\psi(0)$, the charge in an arbitrary surface-state distribution can be calculated and Gauss's law can be invoked to find the field in the insulator, and thus infer the net voltage across the device. The resultant expression for the net voltage V_m

and the net charge Q_m on the metal are given by (10) and (11) below.

$$V_m = -\frac{kT}{e}\psi(0) - \frac{t}{\epsilon_I}\left\{-\epsilon_s\frac{kT}{e}\psi_x(0) + Q_{SF}(\psi(0))\right\} \qquad (10)$$

where ψ_x is $d\psi/dx$, Q_{SF} is the net surface-state charge, and t is the oxide thickness.

$$Q_m = \left\{-\epsilon_s\frac{kT}{e}\psi_x(0) + Q_{SF}(\psi(0))\right\} . \qquad (11)$$

At frequencies where the charge redistribution can follow the superimposed a.c. signal, the small-signal a.c. capacitance at d.c. bias V_m can finally be written as

$$C = \frac{\frac{dQ_m}{dx}}{\frac{dV_m}{dx}} = \left.\frac{\left\{\frac{e}{kT}\frac{dQ_{SF}}{d\psi}\psi_x - \epsilon_s\psi_{xx}\right\}}{\psi_x + \frac{t}{\epsilon_I}\left\{\frac{e}{kT}\frac{dQ_{SF}}{d\psi}\psi_x - \epsilon_s\psi_{xx}\right\}}\right|_{x=0} \qquad (12)$$

where ψ_{xx} is $d^2\psi/dx^2$.

Note that a correction must be made to (10) if the work function of the metal ϕ_m and the electron affinity X_s of the semiconductor differ. In that case the applied voltage V_A is given by

$$V_A = V_m - \phi_m + X_s \tag{13}$$

with (11) and (12) unchanged.

MIS capacitance curves as calculated by (12) are presented for different temperatures, different doping densities, and different surface-state distributions. Although band structure effects enter in the expressions for the charge densities of electrons and holes through the density of states functions, they effect only the high band-bending portions of the curve where the low-frequency capacitance is nearly that of the oxide alone, and hence are relatively insensitive to band details of the semiconductor. Thus the C-V curves presented in this section will be for a single parabolic valence band and a single parabolic conduction band. Only at very low temperatures and for sufficiently large band bending would capacitance calculations require all the band details as given in energy band calculations$^{(6-8)}$.

Typical curves using the calculation technique described are shown in figs. 1 and 2 using the parameter values of Table 1. These parameters are used throughout unless otherwise specified.

Figure 1 shows the ideal surface-state-free capacitance-voltage curve at different doping densities and different temperatures. Fig. 2 shows the effects of several types of surface-state distributions.

The inserts in fig. 2 give the surface-state density as a

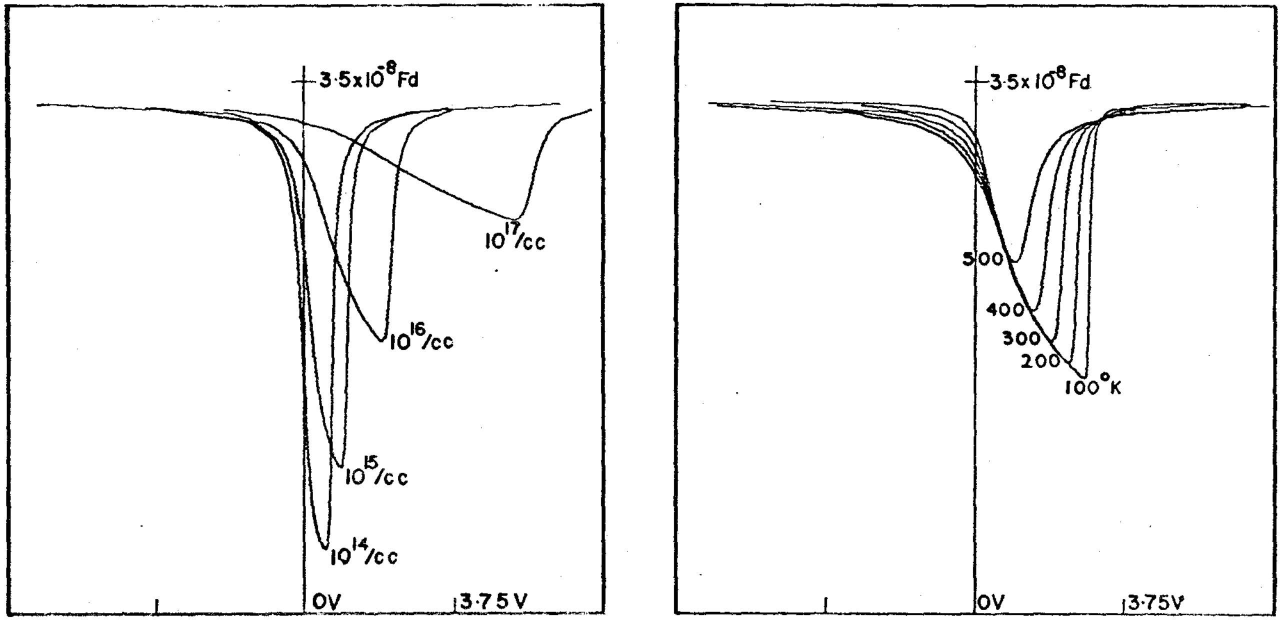

(a) (b)

Figure 1 Ideal, Surface State Free, MIS C-V Curves for p-type Semiconductor (See Table 1 for other semiconductor data).

(a) as a function of impurity concentration at T = 300° K

(b) as a function of temperature for an impurity concentration of 10^{16}/cc.

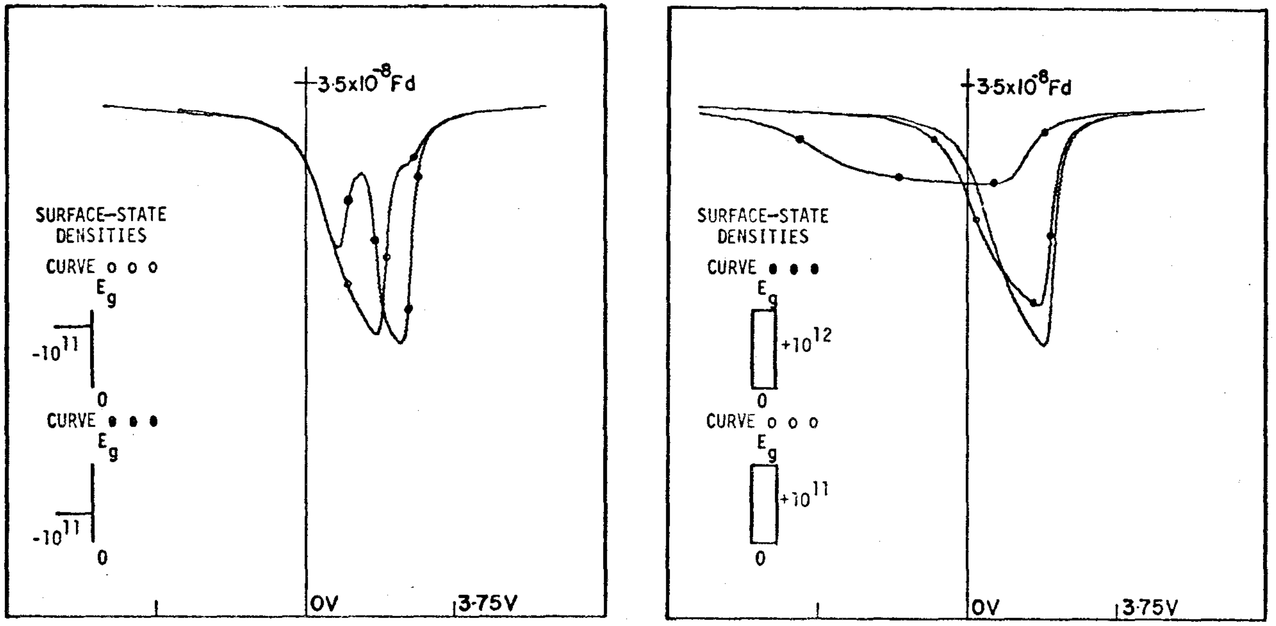

(a)

(b)

Figure 2 MIS C-V Curves for p-type Semiconductor Including Surface States (See Table 1 for other semiconductor data).

(a) for monoenergetic surface state distributions.

(b) for constant surface state distributions. The undesignated curve is the ideal surface state free case.

TABLE 1

Semiconductor Parameter Values

$t = 1000\ \mathring{A}$

$T = 300°K$

$m_e^* = 1.075$

$m_h^* = 0.596$

$\varepsilon_I = 3.82$

$\varepsilon_s = 11.7$

$X_s = \phi_m = 0$

$E_{gap}(T) = 1.106 + (300-T)\ 3.6 \times 10^{-4}$

Area = 1 cm^2

Acceptor energy = 0.045 eV above valence band

Donor energy = 1.061 eV above valence band

Dopant density = $10^{16}/cm^3$

Specified accuracy = 0.5 percent

function of energy across the bandgap. These surface-state distributions were limited to monoenergetic, constant, Gaussian functions of energy, or combinations of these three. All Gaussian distributions have a half width of 0.05 eV and are centred 0.1 eV from either the conduction band or the valence band. The numbers on the inserts refer to total number of states in a distribution. If an interface has no surface states, its surface-state profile is omitted.

Note that the curves of figs. 1 and 2 are in no sense unusual (see, for example, (7)). This points out the fact that in many semiconductor systems of interest, the Boltzmann approximation and the assumption of complete dopant ionization lead to relatively small errors in the C-V curve, chiefly because the ideal low-frequency capacitance is relatively insensitive in high accumulation or inversion. However, even in these cases where the capacitance is reasonably accurate, the interface voltage $\psi(0)$ is greatly affected by the Boltzmann approximation. This, in turn, can lead to substantial errors in calculating surface-state charge(2) and in calculating tunnelling currents through thin oxides.(47)

4. Low Frequency SIS Capacitance

While MIS structures have been studied in detail, little or no work has been done on the SIS system, presumably because it is not related to a major semi conductor device as the MIS system is related to the field effect transistor. Nevertheless, the SIS may have applications as a parametric capacitor and it certainly presents an interesting possibility as a tunneling device$^{(12)}$.

The method of solution for the SIS device is to arbitrarily select a value of interface bending at interface 2 in semiconductor 2($x = 0$ to $x = \infty$), as in fig. 3. Then, using an assumed density of surface states, the interface 2 surface charge is calculated, as well as the field in the oxide. After a number of iterations, a value of band bending at interface 1 is found which, upon calculating the surface-state charge, gives the same value of field in the oxide. Band-bending functions $\psi_2(x)$, $0 < x < \infty$, and $\psi_1(y)$, $-\infty < y < -t$ are manipulated to give low frequency SIS capacitance.

The net voltage across the device and the net charge on either semiconductor are given in (14) and (15):

$$V = \frac{kT_1}{e}\,\psi_1 - \frac{kT_2}{e}\,\psi_2 + \frac{t}{\epsilon_1}\left\{\epsilon_{S2}\,\frac{kT_2}{e}\,\psi_{2x} - Q_{SF2}\right\}\Bigg|_{\substack{x = 0\\ y = -t}} \tag{14}$$

where subscript 1 denotes semiconductor 1 and subscript 2 denotes semiconductor 2;

$$Q_1 = \left\{\epsilon_{S1}\,\frac{kT_1}{e}\,\psi_{1y} + Q_{SF1}\right\}\Bigg|_{y = -t} \tag{15a}$$

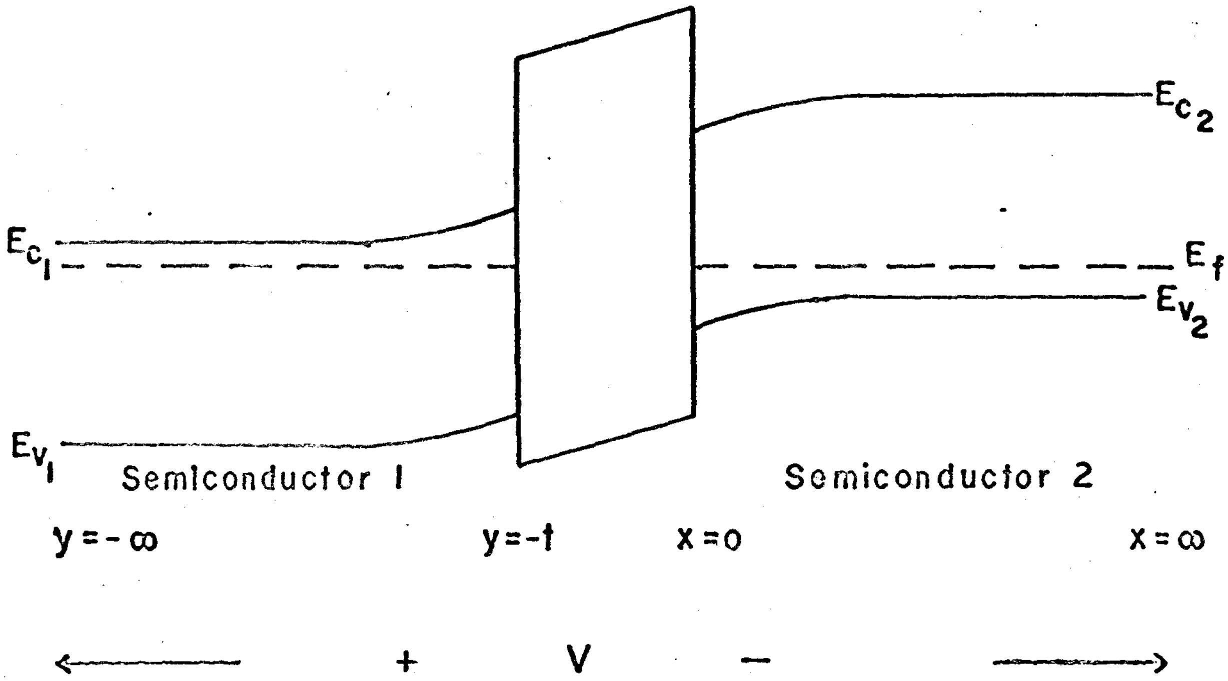

Figure 3 Energy Band Diagram of an SIS System

$$Q_2 = \left\{ -\epsilon_{S2} \frac{kT_2}{e} \psi_{2x} + Q_{SF2} \right\} \Bigg|_{x = 0} \tag{15b}$$

where ψ_{1y} represents $d\psi_1/dy$ and ψ_{2x} represents $d\psi_2/dx$.

At low frequencies the capacitance can be written as

$$C = + \frac{dQ_1}{dV} = - \frac{dQ_2}{dV} = - \frac{dQ_2/dx}{dV/dx} \tag{16}$$

or as

$$C = \frac{\left\{ \frac{dQ_{SF2}}{d\psi} \psi_{2x} - \frac{kT_2}{e} \epsilon_{S2} \psi_{2xx} \right\}}{- \frac{kT_1}{e} \psi_{1y} \frac{dy}{dx} + \frac{kT_2}{e} \psi_{2x} + \frac{t}{\epsilon_I} \left\{ \frac{dQ_{SF2}}{d\psi} \psi_{2x} - \frac{kT_2 \epsilon_{S2}}{e} \psi_{2xx} \right\}} \Bigg|_{\substack{x = 0 \\ y = -t}} \tag{17}$$

where the condition $dQ_1 = -dQ_2$ is required to define dy/dx. Thus the final expression for the low-frequency SIS capacitance becomes

$$C = \frac{\left\{ \frac{dQ_{SF2}}{d\psi} \psi_{2x} - \frac{\epsilon_{S2} kT_2}{e} \psi_{2xx} \right\}}{\frac{kT_1}{e} \psi_{1y} \left\{ \frac{-\epsilon_{S2} \frac{kT_2}{e} \psi_{2xx} + \frac{dQ_{SF2}}{d\psi} \psi_{2x}}{\epsilon_{S1} \frac{kT_1}{e} \psi_{1yy} + \frac{dQ_{SF1}}{d\psi} \psi_{1y}} \right\} + \frac{kT_2}{e} \psi_{2x} + \frac{t}{\epsilon_I} \left\{ \frac{dQ_{SF2}}{d\psi} \psi_{2x} - \frac{\epsilon_{S2} kT_2}{e} \psi_{2xx} \right\}} \Bigg|_{\substack{x=0 \\ y=-t}} . \tag{18}$$

Given electron affinities X_{S1} and X_{S2} in volts, (14) must be modified to give the applied voltage V_A as

$$V_A = V - X_{S1} + X_{S2}. \tag{19}$$

Figures 4-6 show a series of typical C-V characteristics for a number of different SIS devices. Again the physical parameters are those given in Table 1, unless otherwise indicated.

The notation F_1 and F_2 or F_{12} indicates points on the curve at which semiconductor 1, semiconductor 2, or both semiconductors simultaneously reach flatband condition.

Defining inversion as that point at which the minority carrier density equals that of the ionized dopant, the inversion points on the C-V curve are marked by letter I with the appropriate subscript. Since the figures are rather crowded, these points are marked only on one or two curves (inversion points in fig. 4 and flatband points in fig. 5(b)). As before, surface-state density profiles are shown in the figure inserts.

Figure 4 shows C-V curves in the absence of surface states. In fig. 4(a), semiconductor 1 was n type and varied in doping density from 10^{15} to $10^{17}/\text{cm}^3$. In both cases semiconductor 2 was n type with doping density of $10^{16}/\text{cm}^3$.

Except where the dopants are of opposite type and differ in impurity concentration by less than a factor of five, the C-V

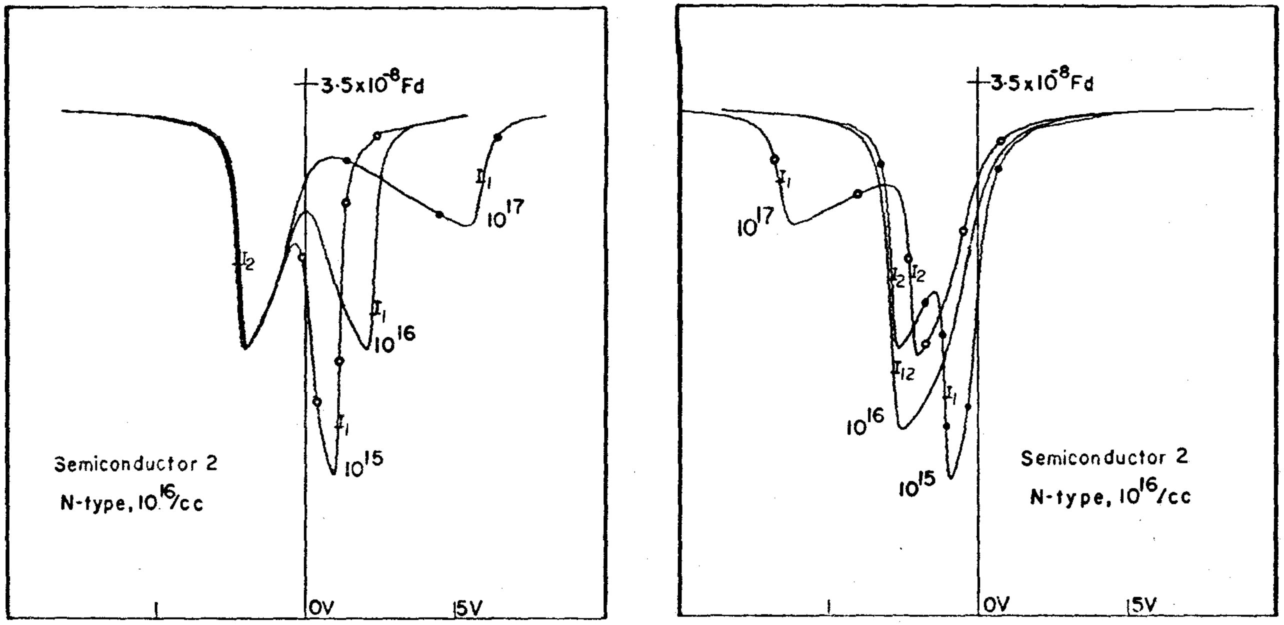

(a) (b)

Figure 4 SIS C-V Curves as a Function of Doping Density, No Surface States (See Table 1 for other semiconductor data).

(a) Ideal n-i-n C-V curves for varying doping density of semiconductor 1 as shown.

(b) Ideal p-i-n C-V curves for varying doping density of semiconductor 1 as shown.

curves exhibit not one, but two depletion regions. In the n-i-n case, one semiconductor must be in depletion-inversion when the other is in accumulation. This results in two depletion minima separated by a region of higher capacitance where both semiconductors are near flatband. Naturally, this would indicate a high-frequency response which leaves only the center maxima where there is a relatively large number of majority carriers in both semiconductors. This type of C-V response has not been observed to date in two-terminal passive devices and is an extremely interesting electronic circuit element. The p-i-n case is more like the conventional MIS capacitor. Both semiconductors are in depletion-inversion and in accumulation at the same time. The depletion minima in fig. 4(b) stand out separately when the doping densities differ by a factor of five or more. The deep narrow depletion well of the lightly doped semiconductor stands out clearly at one end of the broad shallow depletion well of the heavily doped semiconductor. The high-frequency response in this case will lower only the inversion side of the curve and will leave the accumulation side unaffected, much like the conventional MIS frequency response.

Figure 5 and 6 give a selection of SIS C-V curves for various surface-state densities. Fig. 5 shows the effect of surface states at one interface and fig. 6 shows the effect of surface states at both interfaces. For simplicity, the interface 1 surface states in both figs. 5 and 6 were assumed to be monoenergetic. In fig. 6 where surface states were assumed at both

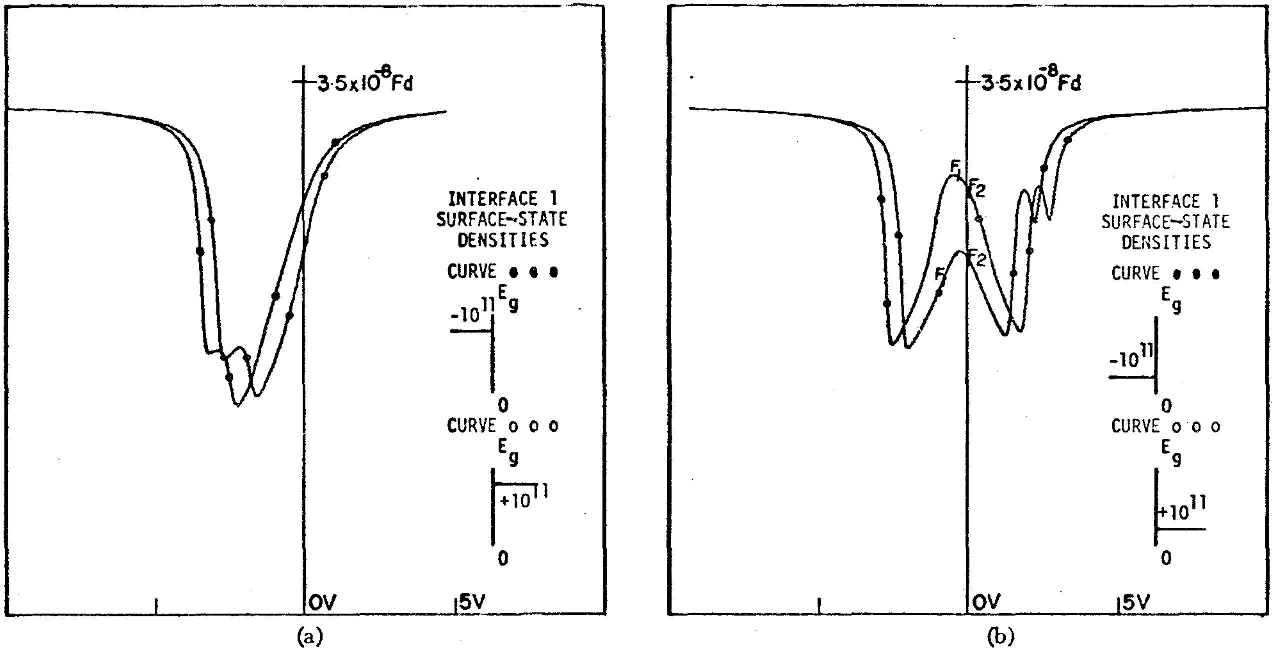

Figure 5 SIS C-V Curves for Surface States at One Insulator Interface (See Table 1 for semiconductor data).

(a) p-i-n capacitance (b) n-i-n capacitance

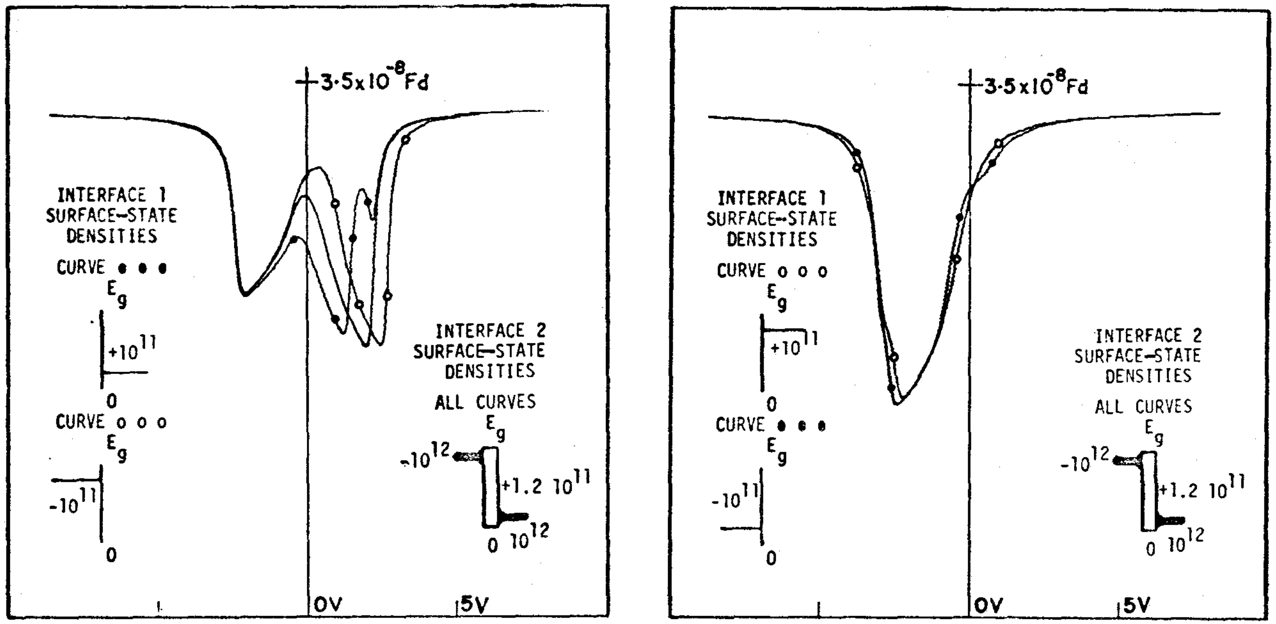

(a) (b)

Figure 6 SIS C-V Curves for Surface States at Both Insulator Interfaces (see Table 1 for semiconductor data).

(a) n-i-n capacitance. The undesignated curve has no surface states at interface 1.

(b) p-i-n capacitance.

interfaces, the distribution of states at interface 2 consisted of a continuum of positive or neutral states totaling 1.2×10^{11} states/cm^2 plus two Gaussian distributions of opposite type each containing 10^{12} states/cm^2.

As in the MIS case, the curves are shifted along the voltage axis by charged surface states with a surface-state capacitance peak which is prominent if the surface-state energy is sufficiently far from the conduction and valence bands. Unlike the MIS device, the voltage range required from accumulation to inversion is considerably greater with lower capacitance minima for the same doping density, particularly in the p-i-n case. This is also true in the surface-state free case.

Figures 5(b) and 6(a) show another interesting feature present only in the SIS structure. The inclusion of surface states at one interface shifts the relative position of the two depletion minima on the C-V curve. This results in the depletion regions of the n-i-n C-V curves (figs. 5(b) and 6(a)) being either more or less resolved, depending on the sign of charged states. For example, surface states of the same charge as the ionized impurity will tend to separate the depletion minima and enhance the center maximum, while surface states of opposite charge will move the minima closer together and reduce the center maximum. This effect is most clearly seen in fig. 6(a) where the undesignated curve with no surface states at interface 1 has a center maximum of intermediate height and resolution.

The C-V curves of figs. 5(a) and 6(b) are for the p-i-n structure with an equal impurity density on each side. Hence, the depletion minima overlap and only one can be seen. Naturally, this minimum is deeper and broader than a corresponding MIS depletion minimum. The bump in the depletion minima of the curves in fig. 5(a) is not due to surface-state capacitance, but is due to the fact that the surface-state charge at interface 1 has slightly separated the depletion minima.

5. Summary

In Chapter II a solution of Poisson's equation has been developed of specified accuracy using full Fermi functions for the hole, electron, and impurity bands. This renders unnecessary the assumptions of Boltzmann statistics and full impurity ionization required by previous authors (13-16).

The solution has been programmed in Fortran IV and, on a CDC 6400 computer, requires 30 seconds to generate 120 points on an MIS C-V curve and 60 seconds to generate 120 points on an SIS curve. For an accuracy of 0.5 percent, a core storage of 40,000 is desirable. It has been used to give accurate MIS and SIS low-frequency C-V curves at different temperatures, different doping densities, and for different surface-state distributions.

The technique was tested on several MIS systems and then applied to various SIS devices. It was found that the n-i-n device displayed C-V curves unlike the usual MIS curves. Two depletion regions stand out about a center maximum. This center maxima can be strengthened or reduced by the presence of surface states. In the p-i-n case where the doping densities differ by a factor of five or more, a deep narrow depletion minimum can be seen superimposed on a broad shallow minimum. Again surface states have the effect of shifting their relative positions on the C-V curve.

This work predicts an interesting high-frequency response for the n-i-n structure, namely a bell-shaped C-V curve. This type of C-V response has not been observed to date in other two-terminal passive devices, and may lead to SIS applications as a new type of parametric capacitor.

CHAPTER III

EXACT A.C. ADMITTANCE OF THE MIS DIODE

1. Introduction to the MIS A.C. Solution

The MIS structure has been widely studied in both its basic role in modern semiconductor applications and as an important tool in investigating the electronic properties of the semiconductor, the oxide and the interface region. Many researchers have made important contributions to the theory of the MIS device. Still, the greatest need to date has been for an accurate and general solution of the semiconductor behaviour over the complete d.c. bias and a.c. frequency ranges based on rigorous derivation from first principles and it is this problem that has motivated the work presented here in Chapter III.

The usual experimental procedure is to apply a d.c. bias across the device and then superimpose a small amplitude a.c. voltage at radian frequency ω . The complex a.c. admittance at that frequency and applied bias is read on an admittance bridge. Since these measurements can generally be made at various temperatures, there exists a wealth of data with which to characterize the device.

In addition, studies can be made by doping the semiconductor, altering the surface state density by surface treatments, ranging the oxide thickness, or varying the work function difference through choice of the metal. Often other effects can be obtained by illuminating the semiconductor with light or by carrier injection from a third contact.

A complete and accurate theoretical treatment of the MIS system is important for two reasons. First it allows one to predict the electrical characteristics of new MIS devices. Secondly, it should be able, in conjunction with careful experiment, to clarify or define the physics of the device. In this respect, the application most often seen in the literature has been principally that of defining the surface state density with either the conductance method(17), the integration method(18) (where the interface potential, ψ_s, is determined by integrating $\frac{1 - C(V)}{C_{ox}}$), the temperature method(19) (where ψ_s and the surface state charge change with temperature), or the differential method (where one graphically differentiates the experimental high frequency C-V curve).

The first part of such a study, the solution of the electrostatic problem given a d.c. bias, is not a formidable one provided that the semiconductor is at or near thermal equilibrium. The solution of Poisson's equation defines the charge densities and electric field at any point in the system and these are sufficient to calculate the complex a.c. admittance at $\omega = 0^+$.

Most solutions described in the literature, however, are restrictive to some extent by assuming complete ionization of all dopants and generally using Boltzmann statistics. The first assumption puts a joint condition on the impurity density and the impurity band energy and the second assumption precludes an accurate knowledge of the band bending at the insulator-semiconductor (IS) interface when it is within 4 or 5 kT of the bandgap edges. An improved solution of prespecified accuracy which avoids these assumptions was discussed in Chapter II.

The second part requires a solution of the charge redistribution under the influence of the small amplitude a.c. signal applied across the device. This involves the solution of two interdependent sets of nonlinear differential equations to give the a.c. hole and electron currents at any point in the semiconductor.

There are a number of approximate treatments of this problem which give excellent results over certain frequency and voltage regions, depending, of course, on the restrictions already imposed by the d.c. solutions. The simplest of these gives the so-called high frequency response of the imaginary (capacitance) part of the a.c. admittance by assuming complete response of the majority carriers and no response for the minority carriers(2). The lower frequency limit of this range is generally controlled by generation-recombination processes. For semiconductor systems with little generation and recombination this "high" frequency range can run from a lower limit as small as 0.1 Hertz to an upper limit of more than 10^{10} Hertz depending chiefly on impurity doping densities and temperature.

In terms of device applications, frequency independent capacitance over a large range is a desirable feature and, therefore, materials with low recombination-regeneration properties are important. At the same time, however, the complex admittance may have considerable frequency dependence since the a.c. conductance, principally due to surface states (at least in this frequency range), is strongly frequency dependent and may be fairly large.

Much of the physical information concerning the semiconductor obtainable from the device is generated in the low frequency range in which the minority carriers go from complete response to no response. A number of lumped parameter electrical models(17,4,21,35) have been derived to apply in this region. In most of these a single constant parameter is used to describe the minority carrier generation-recombination and this parameter is obtained after the experiment has been performed. This lumped parameter approximation works rather well, it seems, for low to medium recombination rates but still suffers from two faults. First,as an approximation to a very complicated mechanism, its reliability is doubtful particularly at elevated temperatures and moderate to high recombination rates. Second, it is a parametric model as opposed to one derived from first principles. In this respect, it is distinctly less useful as a method of predicting the response of other systems or, in conjunction with experiment, of yielding useful information on the physics of the materials in the structure.

Sah et al$^{(2)}$ have presented a transmission line circuit model which is an exact analog of the small signal transport equations in the semiconductor. Surface states and different types of generation-recombination effects can be explicitly represented in the model including the Shockley-Read-Hall (SRH) type which be considered in this paper. To date, there has been little exploitation of this exact model and no general, rigorous solutions, although it has been applied in various approximations to several systems$^{(2,21,24)}$. Chapter III of this thesis presents the first general and exact solution of this model yielding frequency, surface state, SRH centre, and temperature effects, as well as an example of a nonequilibrium solution with light stimulated SRH processes. To take advantage of the various features of the d.c. solution, the model as presented in Sah's paper will be generalized to take into account the Fermi statistics of the charge carriers and the a.c. response of the dopant impurity band.

In the following sections the a.c. model will be presented with various modifications and, some results, obtained through its exact solution, will be presented. Note that these results will concentrate on areas where an exact solution from first principles is most useful and where models now available are most prone to error. This will include: (1) minority carrier response in the low frequency range as a function of temperature, SRH centre effects, doping density and light stimulated generation-recombination processes, (2) surface state effects at the interface where it will be shown that the G-V structure analysis used to obtain surface state densities can be improved by removing from the conductance that portion due to the semiconductor space charge response, (3) impurity band response and bulk freeze-out effects which are observed in the low temperature, high dopant concentration situations. Note that both C-V and G-V curves will be presented in each analysis.

2. The MIS A.C. Problem Under the Thermal Equilibrium Condition

The equilibrium condition basically assumes that the population densities of the various charge bands have their thermal equilibrium values. Generally speaking this is the case for the MIS structure with an oxide thick enough to prevent sizable d.c. currents. Under this condition the small signal transport equations and the analog electrical model can be simply derived. Under the condition of no regeneration-recombination, conservation of charge gives

$$\frac{d\ \delta\rho_p}{dt} + \nabla\cdot j_p = 0; \quad \frac{d\ \delta\rho_n}{dt} + \nabla\cdot j_n = 0; \quad \delta\rho_t = \delta\rho_p + \delta\rho_n \tag{20}$$

where $\delta\rho_p$, $\delta\rho_n$ and $\delta\rho_t$ are the change (from thermal equilibrium) in hole, electron and total charge densities at position x, and

j_n and j_p are the electron and hole band a.c. conduction currents.

Poisson's equation for the a.c. charge density becomes

$$\nabla^2 v_k\ (x,t) = -\ \delta\rho_t(x,t)/\epsilon_S \tag{21}$$

where v_k is the a.c. potential.

The total a.c. current, j_t, is spatially constant, consisting of conduction plus displacement currents.

$$j_t = j_n + j_p - \epsilon_s\ \nabla\dot{v}_k \tag{22}$$

where $\frac{d}{dt}$ is denoted by a dot above the quantity.

To derive the transmission line model, which is presented in fig. 7(a), requires $\delta\rho_n$ and $\delta\rho_p$ to be expanded in terms of a.c. quasi Fermi-level potentials $v_n\ (x,t)$ and $v_p\ (x,t)$ and the definition of a.c. current densities $j_n(x,t)$ and $j_p(x,t)$ in terms of mobility and electric field. Utilizing the small signal assumption, $\delta\rho_n$ and $\delta\rho_p$ are expanded to first order in $(v_n - v_k)$ and $(v_p - v_k)$ to yield:

$$\begin{aligned} \frac{d\ \delta\rho_p}{dt} &= -\frac{\partial P}{\partial V}\ (\dot{v}_p - \dot{v}_k) = C_p(x)\ (\dot{v}_p - \dot{v}_k) \\ \frac{d\ \delta\rho_p}{dt} &= -\frac{\partial N}{\partial V}\ (\dot{v}_n - \dot{v}_k) = C_n(x)\ (\dot{v}_n - \dot{v}_k) \end{aligned} \tag{23}$$

$$\begin{aligned} j_n &= -e\mu_n N \nabla v_n = -\frac{e\mu_n N}{\delta x}\ (v_n(x+\delta x) - v_n(x)) \\ j_p &= -e\mu_p P \nabla v_p = -\frac{e\mu_p P}{\delta x}\ (v_p(x+\delta x) - v_p(x)) \end{aligned} \tag{24}$$

Figure 7 A.C. Transmission Line Model of the MIS Device (See Appendix 2 for parameter values).

(a) Semiconductor model, no SRH centres and no surface states. P_j and N_j label nodes on the hole and electron band conduction paths with a.c. voltages v_{P_j} and v_{N_j}. K_j labels nodes on the displacement current path with a.c. voltage v_{K_j}. (Nodes K_j are at a d.c. voltage, V_{K_j}, given by the electrostatic potential while the d.c. voltages of P_j and N_j differ from V_{K_j} by the d.c. quasi Fermi level shifts.)

(b) Inclusion of non-interacting SRH centres. One node R_i is added for each centre in each section of the model of (a).

(c) Inclusion of non-interacting surface states. One node, S_i is added at the interface for each surface state band.

(d) The non equilibrium modifications to (a) and (b).

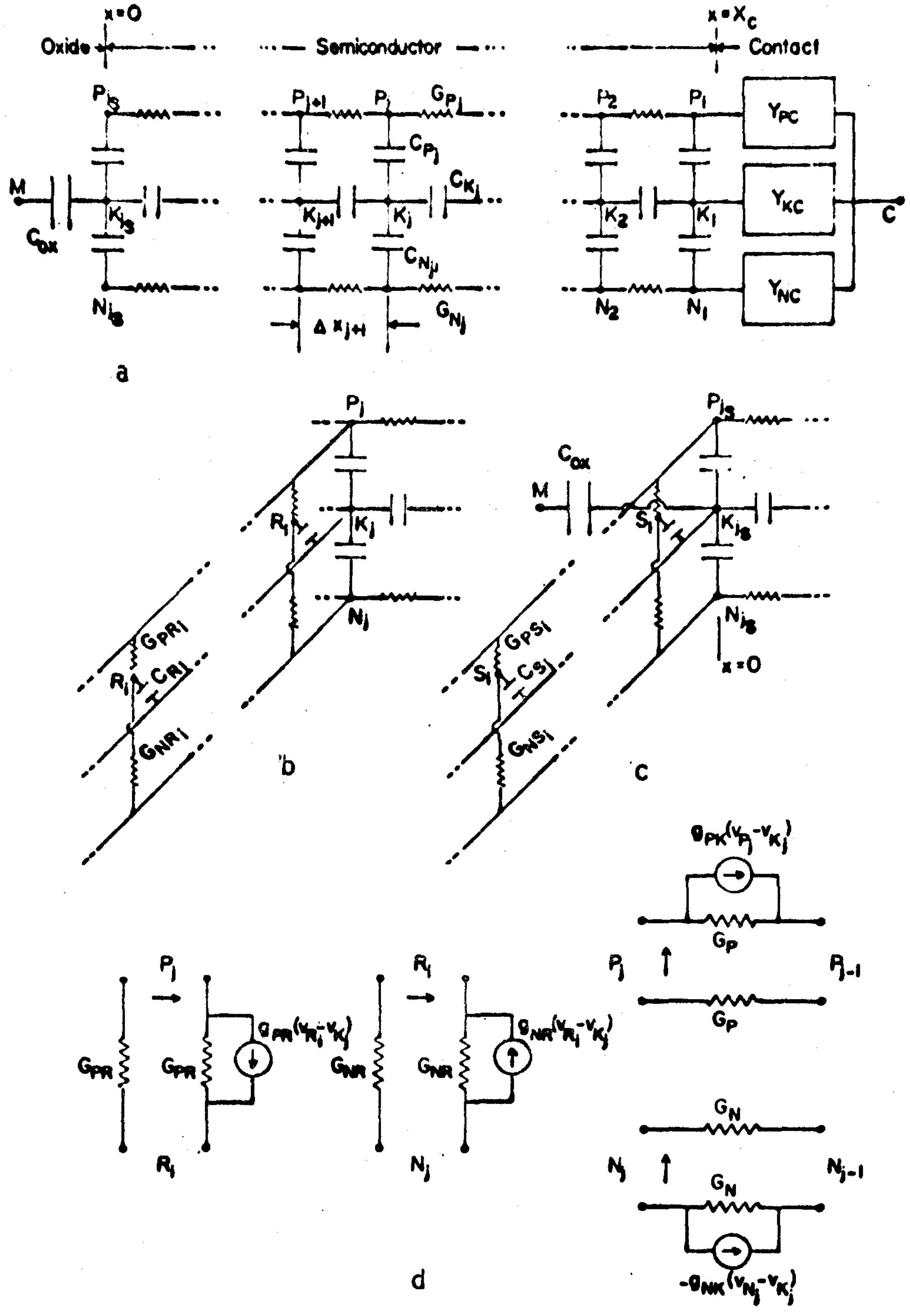
x=0
Oxide
Semiconductor
x=X_c
Contact
P_is
P_j+1
P_j
G_Pj
P_2
P_1
Y_PC
C_Pj
M
K_is
K_j+1
K_j
C_Kj
K_2
K_1
Y_KC
C
C_ox
C_Nj
N_is
N_2
N_1
Y_NC
Δx_j+1
G_Nj
a
P_j
R_i
K_j
N_j
G_PRi
R_i
C_Ri
G_NRi
b
P_is
C_ox
M
S_i
K_is
N_is
x=0
G_PSi
S_i
C_Si
G_NSi
c
g_PK(v_Pj-v_Kj)
G_P
P_j
P_j-1
G_P
P_j
R_i
G_PR
G_PR
g_PR(v_Ri-v_Kj)
G_NR
G_NR
g_NR(v_Ri-v_Kj)
R_i
N_j
G_N
N_j
N_j-1
G_N
-g_NK(v_Nj-v_Kj)
d

Figure 7

where N and P are the electron and hole densities and $V(x)$ is the d.c. electrostatic potential at x. Note that the statistics of the system enter implicitly in the quantities, N, P, $\partial P/\partial V$ and $\partial N/\partial V$.

The a.c. model given in fig. 7(a) and the admittance parameters defined for it in Appendix 2 are derived by inspection from equations (22) to (24). Consider the j^{th} slice in fig. 7(a). It is easily seen that a.c. conduction currents j_n and j_p flow in elements G_{P_j} and G_{N_j} under field gradients ∇v_P and ∇v_n, with the displacement current, $\epsilon_s \nabla \dot{v}_k$, flowing through capacitor C_K. Thus equation (22) is satisfied. $\delta\rho_p$ is stored on capacitor C_{P_j} and $\delta\rho_n$ on C_{N_j} with $\delta\rho_t$, therefore, stored on capacitor C_{K_j}. Since $\delta\rho_t(x)$ is stored on C_K, the a.c. voltage, v_k, must satisfy equation (21) provided C_K is correctly defined.

To include recombination centres in each slice one node must be added for each impurity as shown in fig. 7(b). At the interface, surface state levels* are added as shown in fig. 7(c). The corresponding admittance parameters$^{(32)}$, tabulated in Appendix 2, have been generalized to accept Fermi statistics or any other statistics. A further generalization has been to include the mobility as a function of dopant density and electric field, $\underline{E}$. These dependences$^{(27)}$ are defined by equations (A1) and (A2) in Appendix 1 which gives the semiconductor parameters used in the actual calculations.

---

*The computer program presently allows up to 120 surface state levels.

The method for solving a.c. voltages $v_n(x,t)$, $v_p(x,t)$ and $v_k(x,t)$ lies in writing down the admittance matrix for the transmission line and solving for the determinant and cofactors required to give the necessary impedance matrix elements of the inverted admittance matrix. Starting with the admittance matrix of the back contact and assuming no band bending at the interface, each slice Δx_j of semiconductor is added in until the length of the transmission line equals that of the semiconductor. Since only three quantities are required to specify the complete complex admittance, only three cofactors and the determinant of the $[N(3 + \text{number of trap bands}) + Nss]^{th}$ order square matrix need be calculated (N is the number of sections in the semiconductor transmission line and N_{ss} the number of surface state levels). This is done by a series of recursion relationships which first add the next bare slice, then include the SRH centres (or any other charge transfer mechanisms that one desires to consider) and finally, at the surface, add in the surface state nodes.

For the case of a uniform semiconductor it is a simple matter to recalculate the admittance at a new interface voltage. All that is required is the addition of another section (or sections, depending on the required accuracy) for the additional space charge region and the deletion of an equal distance from the bulk portion of the transmission line. This simplification under the condition of uniform impurity concentration (in the space charge region) enables a saving in overall computing time of a factor of between

50 and 100. In view of this, the examples in the following sections are all uniformly doped. For band bending >.01 eV, an additional 50% reduction in computer time can be achieved without loss of accuracy for cases in which the bulk region is about 10 times thicker than the space charge region by not deleting the bulk slice. Hence, curves presented in this paper use a semiconductor wafer thickness of .01 mm.

All results presented in the following sections utilize a d.c. solution accurate to 1/2%. The slice widths, Δx, in the a.c. model have been chosen to guarantee that the C and G values will not differ by more than 1/2% from the values which would be obtained using an infinite number of slices. At radian frequency $\omega = 0$, the a.c. solution fails completely as the admittance matrix becomes indeterminant. For the sake of completeness however, the exact C-V curves can be calculated from equations (10), (11) and (12) in Chapter II and, for a perfect insulator, the a.c. conductance G goes to zero.

3. Light Stimulation as a Non-Equilibrium Problem

Such external stimuli as carrier injection or hole-electron pair creation by light aided generation result in the introduction of current sources in equations (20), (21) and (22). Hence the a.c. model in fig. 7(a) is no longer valid but requires the addition of several active elements, namely current sources, as indicated in fig. 7(d). The admittance matrix is slightly more complicated but the analysis and the recursion relationships remain valid, and, from the point of view of the a.c. solution, there is no problem once the d.c. solution, which is required to give explicit values to the a.c. parameters, has been solved.

The difficulty here lies in solving the d.c. problem which, instead of simply being described by Poisson's equation, now requires the d.c. transport equations and the complete set of interdependent rate equations(32,33) of all the charge bands. For the thick insulator case, the problem is greatly simplified by the absence of large d.c. currents.

To solve the d.c. problem, a d.c. quasi Fermi level shift is calculated in the bulk and assumed to be spatially constant in the space charge region. This approximation is discussed by R. F. Pierret and C. T. Sah(24) in their theoretical treatment of the problem. In this thesis, instead of requiring the introduction of parameters to fit experiment, the non equilibrium transmission line given in fig. 7 can still be rigorously solved. This arises from the fact that the light stimulated bulk pair production rate is related to the bulk quasi Fermi level using equation (A3) in Appendix 2 and inserting a quasi Fermi level into ρ_c or ρ_v as shown below.

$$N = \frac{\rho_c}{-e} = \int_{CB} g_c(E) f_c(E-\phi_N) dE$$

and (25)

$$P = \frac{\rho_v}{e} = \int_{VB} g_v(E) f_v(E+\phi_p) dE$$

where ϕ_N and ϕ_P are the d.c. quasi Fermi level shifts of the electron and hole bands respectively and N and P, the electron and hole carrier densities.

In terms of the model of fig. 7(d), and having assumed a ϕ_N or ϕ_P, the pair recombination rate, R_L, can be calculated by equation (A3) in Appendix 2. Note that this value, R_L, appears in the transconductance, g, of the various active elements in fig. 7(d).

Having calculated R_L, the d.c. solution can be solved to give explicit values to the a.c. admittances and the a.c. model then solved in the usual way. The results, for different values of light stimulated bulk-pair production rates, will be given in section 4d along with the related value of d.c. quasi Fermi level shift. Note that, unlike the other curves given in this chapter, these results cannot be called exact analytical solutions. However, the failure is not in the a.c. solution but in the approximation required in the d.c. solution.

4. MIS Minority Carrier Response

Applying an a.c. voltage to an MIS device results in charge redistribution in the semiconductor through displacement current and conduction currents. For biases in the accumulation range, the dominant charge transfer mechanism is the majority carrier conduction current.

When biased in inversion, however, the charge redistribution is more complex. Fig. 8 illustrates the charge transfer mechanism

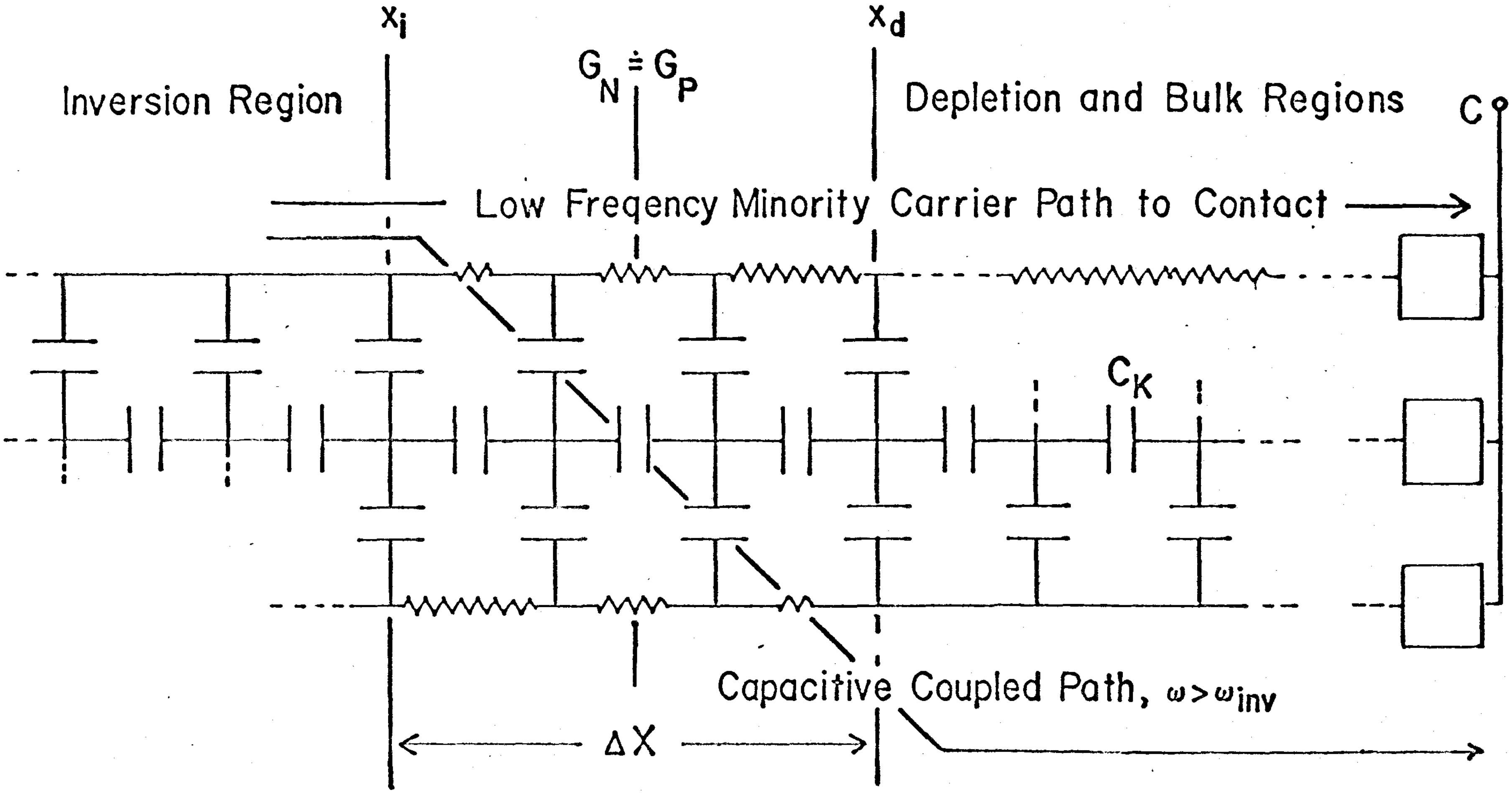

Figure 8 Inversion Bias, Low and High Frequency Current Paths from Interface to Contact.

going from predominantly minority carrier conduction current in the inversion layer to a largely majority carrier conduction current in the bulk. With no space charge generation-recombination, the coupling between the two currents is purely capacitive and occurs primarily in a region of width ΔX_c (see fig. 8 where both carrier densities are roughly the same. Since the total a.c. current is spatially constant, the displacement current is largest when the total conduction current is smallest. This occurs in regions of band bending where the Fermi level is near midgap i.e., in the region ΔX_c. Note that at very low frequencies the bulk and depletion region conductance cannot be considered an open circuit since they may be large with respect to the capacitive admittance in ΔX_c. At these frequencies inversion layer minority carrier flow will be direct from the contact to the interface with a smaller fraction capacitively coupled in ΔX_c. Increasing the frequency increases the fraction of current flowing to the interface through the capacitive coupling region until, finally, it carries virtually all the interface current.

For all regions of d.c. bias the a.c. current in a perfect insulator is totally a displacement current. Because individual current components are continuous, the semiconductor current right at the interface must be a displacement current. This displacement current becomes conduction current through mobile charge coupling capacitance (as shown in fig. 7(a) as C_P and C_N). When the interface is biased in accumulation or inversion, this coupling takes place over a semiconductor region of a few Å width. When biased in depletion, this coupling of the interface displacement current to the band conduction currents is much weaker and takes place over a relatively longer distance.

In examining the C-V and G-V curves presented in this chapter, it will often be possible to explain voltage and frequency dependent features in terms of the model in fig. 8 or in terms of the displacement-conduction current coupling at the interface.

(a) The Effect of Doping Density (No Surface States, No SRH Centers)

Figure 9 gives C-V and G-V curves for an ideal MIS device in which there are no surface states and no SRH centers. The C-V curves show all the usual features: the depletion well and the fall off of the inversion response to the depletion approximation as the frequency is raised. The minority carrier cutoff frequency, as expected, reflects the high bulk and depletion layer minority carrier resistivity. The higher the doping density, the higher the bulk minority carrier band resistivity and the lower the frequency at which direct minority carrier current flowing from the interface to the contact switches to the capacitively coupled path shown in fig. 8.

In addition to the usual C-V features, fig. 9(c) shows an unusual example of majority carrier response cutoff. At very high frequencies, the accumulation capacitance begins to fall, reflecting the change of bulk current flow from majority carrier conduction current to displacement current through capacitive elements, C_K

Figure 9 Ideal MIS C-V and G-V Curves as a Function of Impurity Dopant Density, No Surface States or SRH Traps. (All curves are at T = 300°K for oxide thickness of 1000 Å. ω is the radian frequency. See Appendix 1 for other semiconductor data. 'G' is in units of mho m^2.)

(a) C-V, moderately doped p-type Si(10^{15}/cc).

(b) C-V "degenerately" doped p-type Si(10^{19}/cc).

(c,d) C-V and G-V "intrinsically" doped p-type Si(10^{11}/cc).

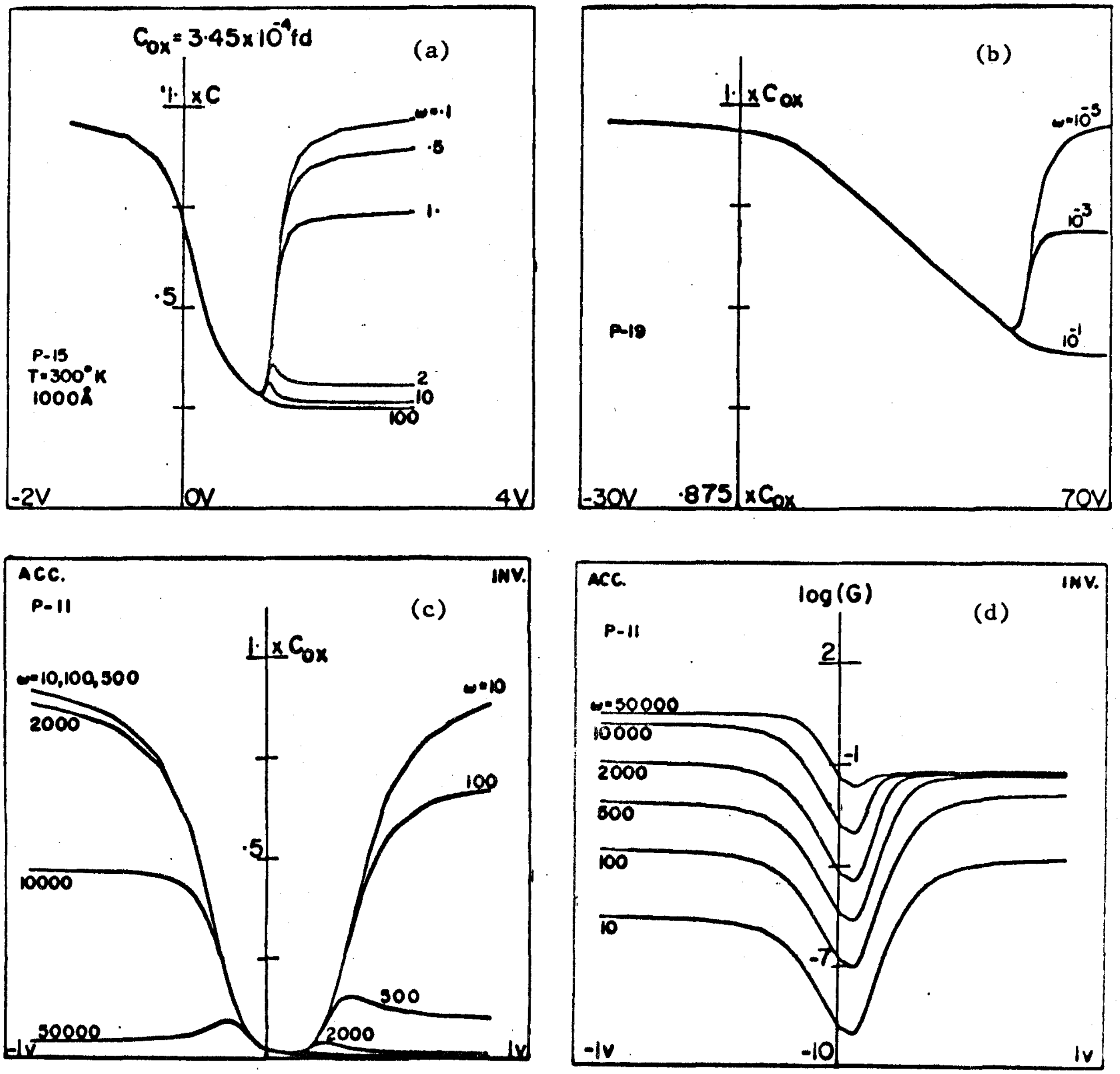
$C_{ox} = 3.45 \times 10^{-4}$ fd
(a)
·1· x C
ω=·1
·5
1·
·5
P-15
T=300° K
1000Å
2
10
100
-2V
0V
4V
(b)
1· x C_{ox}
ω=10^{-5}
10^{-3}
P-19
10^{-1}
-30V
·875
x C_{ox}
70V
ACC.
INV.
P-11
(c)
1· x C_{ox}
ω=10,100,500
2000
ω=10
100
·5
10000
500
50000
2000
-1V
1V
ACC.
log(G)
INV.
P-11
(d)
2
ω=50000
10000
-1
2000
500
100
10
-7
-1V
-10
1V

Figure 9

(see fig. 8). To observe this type of response in the usual MIS frequency range (below 1 mHz) requires a virtually pure semiconductor. With typical commercially obtainable "intrinsic" samples the majority carrier cutoff frequency would probably be in the microwave region. At such frequencies this would require the complex frequency dependent dielectric constant $\epsilon_S(\omega)$ to be used in the transmission line model. In addition, virtually perfect ohmic contacts would be required so as not to cause all the a.c. conductance loss to occur in the contact.

The G-V response for the "intrinsic" material of fig. 9(c) is illustrated in fig. 9(d). Both an accumulation and an inversion conductance saturation (in voltage) can be seen. These will be denoted by $G^V_{acc}(\omega)$ and $G^V_{inv}(\omega)$ where the superscript V denotes a voltage saturation and ω is the radian frequency. Both saturations occur because biasing the interface further into accumulation or inversion requires the addition of a relatively lossless section of transmission line corresponding to the additional space charge region.

In addition to the voltage conductance saturation, there is a frequency saturation on both the inversion and accumulation sides. With an increase in radian frequency, ω, there is an increase in the capacitive admittance (reactance) of both the oxide and of all the capacitive elements of the transmission line. Therefore the relative proportion of displacement current to conduction current increases. This leads to a frequency saturation of $G^V_{inv}(\omega)$ and

$G^V_{acc}(\omega)$ at conductance saturation values G^ω_{inv} and G^ω_{acc} respectively. In fig. 9(d) G^ω_{inv} is clearly present while the $G^V_{acc}(\omega)$ are just starting to approach G^ω_{acc}.

Plots of $G^V_{inv}(\omega)/\omega$ and $G^V_{acc}(\omega)/\omega$ against ω must show maxima. These occur at frequencies corresponding to the minority carrier cutoff frequency, ω_{inv}, and the majority carrier cutoff frequency, ω_{acc}. The G/ω values listed in Table 2 are taken from fig. 9(d) and indicate, for this doping density, an ω_{inv} of about 500 and an ω_{acc} of about 10^4. For normal experimental doping densities, ω_{acc} will generally be in the microwave region where other effects may have to be taken into account. Note that ω_{inv}, as defined here, can be used as the demarcation between the low frequency and high frequency ranges. It can also be used to good effect in selecting parameters for the simpler models(4). Note also that ω_{inv}, while reflected in the C-V inversion region response, cannot be defined so precisely from the C-V curves. For example: from fig. 9(a) $.1 < \omega_{inv} < 100$, from fig. 9(b) $10^{-5} < \omega_{inv} < 10^{-1}$ and from fig. 7(c) $10 < \omega_{inv} < 2000$.

(b) The Effect of Temperature

The effect of increasing temperature on the C-V response is primarily an increase in minority carrier density in the bulk region, raising the cutoff frequency, ω_{inv}, of the low frequency range. Fig. 10 shows C-V curves at four temperatures for a fixed frequency. Clearly at T = 325°K, $\omega = 2$ lies well inside the low frequency range while at T = 290°K, it lies definitely outside.

TABLE 2

Accumulation and Inversion Values of $G(\omega)/\omega$

(For the G-V Curves of Figure 9(d)

ω	10	100	500	2000	10000	50000
G^V_{acc}/ω	-	-	1.3×10^{-5}	5.5×10^{-5}	1.5×10^{-4}	6.0×10^{-5}
G^V_{inv}/ω	1.5×10^{-5}	1.3×10^{-4}	1.0×10^{-3}	2.9×10^{-4}	6.2×10^{-5}	1.3×10^{-5}

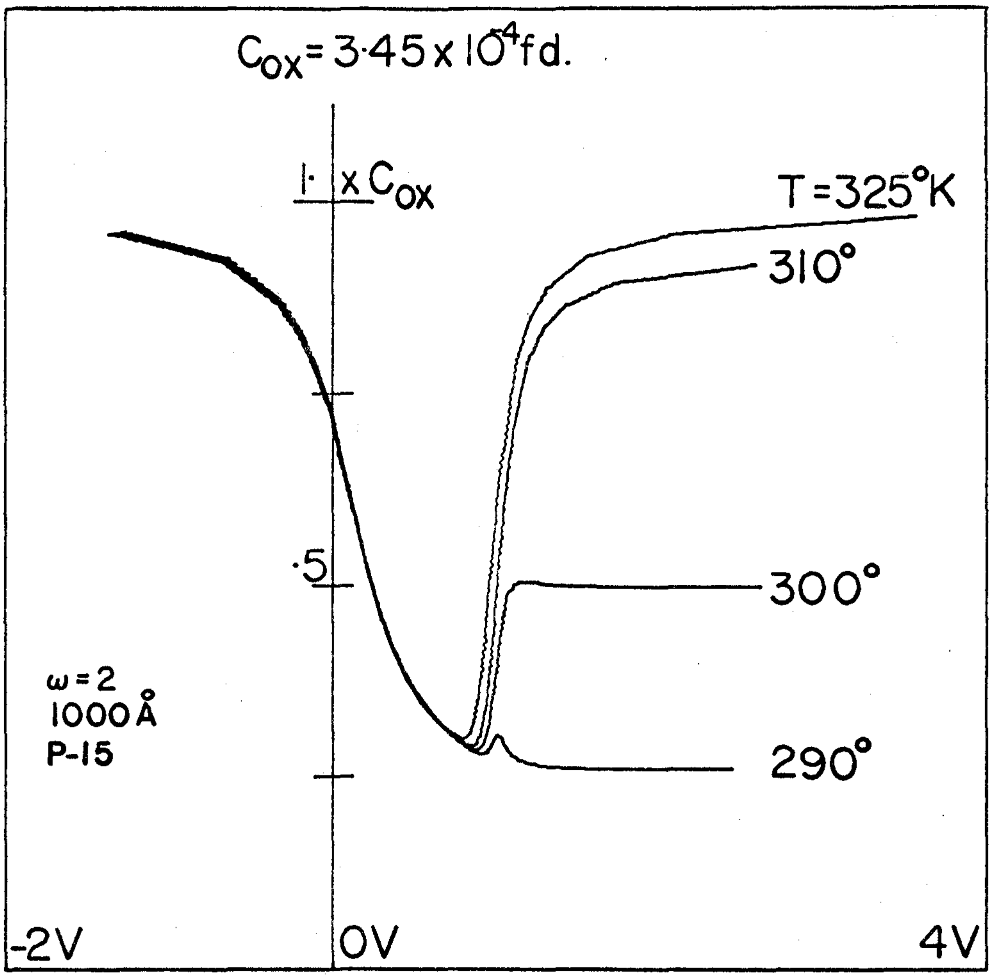

Figure 10 Fixed Frequency MIS C-V Curves as a Function of Temperature, No Surface States or SRH Traps. (Doping density is p-type,10^{15}/cc. See Appendix 1d for other semiconductor data.)

The G-V response with changed temperature is more complicated and depends on the frequency. The nature of this dependence will be discussed in a later section of this chapter.

(c) Effect of SRH Centers

The effect of SRH traps on the C-V and G-V curves lies chiefly in their modification of the coupling region, ΔX_c, shown in fig. 8. The coupling is now a combination of resistive elements and capacitive elements* whose overall effects are quite complex. This is shown in fig. 7(b) through the addition of elements G_{PR}, G_{NR} and C_R which provide a direct majority-minority coupling current.

From the C-V curves shown in fig. 11, it can be seen that the SRH center provides, as one expects, more minority carrier response and hence an increase in the response cutoff frequency, ω_{inv}. The inversion capacitance response is correspondingly higher.

The G-V response also reflects the higher value of ω_{inv}. G^{ω}_{inv} is higher for example, at $\omega = 100$ in fig. 11(f), G^{V}_{inv} increases with trap density. However, for frequencies below ω_{inv}, as for example at $\omega = 1$, in fig. 11(b), G^{V}_{inv} decreases with trap density. This seeming contradiction arises from the fact that, at low frequencies, losses are in the depletion and bulk minority conductance elements $G_{N(or\ P)}$ of fig. 7(a). With high SRH density these elements are bypassed and the result is an increased current flowing conductively through the less lossy coupling region, ΔX_c.

---

*Element values are defined in Appendix 2.

Figure 11 MIS C-V and G-V Curves as a Function of SRH Trap Density at $\omega=1$, 5 and 100, No Surface States. (All curves are for p-type, 10^{15}/cc semiconductor with an oxide thickness of 1000 Å and temperature of 300°K. Other pertinent data is given in Appendix 1c. G is in units of mho m^2.)

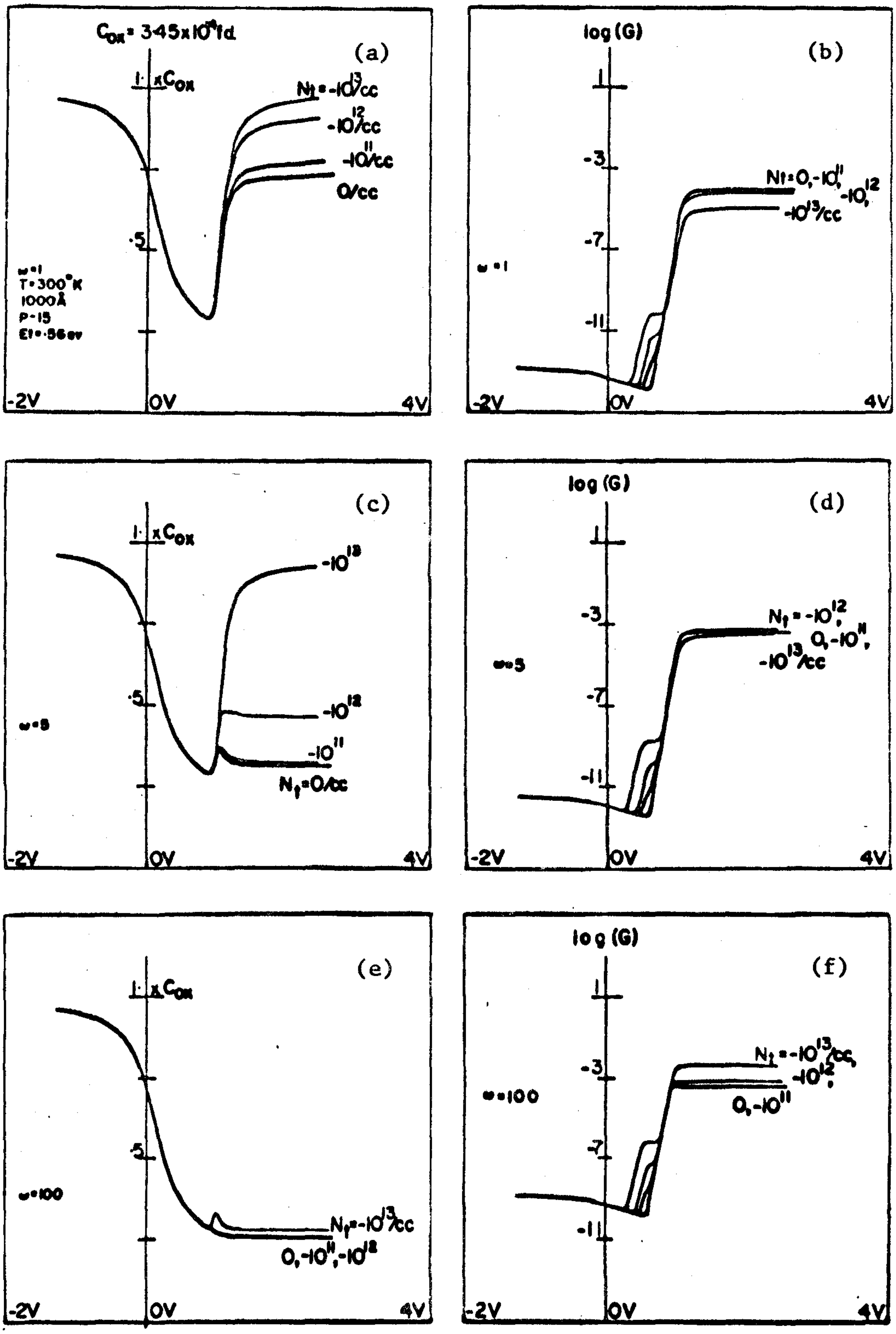
$C_{ox} = 3.45\times10^{-8}$ fd
(a)
1· $\times C_{ox}$
·5
$N_t = -10^{13}$/cc
-10^{12}/cc
-10^{11}/cc
0/cc
ω=1
T=300°K
1000Å
P-15
Et=·56ev
-2V
0V
4V
log (G)
(b)
1
-3
-7
-11
N_t=0, -10^{11}, -10^{12}
-10^{13}/cc
ω=1
-2V
0V
4V
(c)
1· $\times C_{ox}$
·5
-10^{13}
-10^{12}
-10^{11}
N_t=0/cc
ω=5
-2V
0V
4V
log (G)
(d)
1
-3
-7
-11
$N_t = -10^{12}$,
0, -10^{11},
-10^{13}/cc
ω=5
-2V
0V
4V
(e)
1· $\times C_{ox}$
·5
$N_t = -10^{13}$/cc
0, -10^{11}, -10^{12}
ω=100
-2V
0V
4V
log (G)
(f)
1
-3
-7
-11
$N_t = -10^{13}$/cc,
-10^{12},
0, -10^{11}
ω=100
-2V
0V
4V

Figure 11

In accumulation and in the flatband condition, the SRH centre has no measurable effect on response. As the interface is biased into depletion and farther into moderate inversion, the coupling region ΔX_c described in fig. 8 forms. The SRH centres, being near midgap, begin to take effect at roughly the same bias resulting in the G-V bumps seen at about .4 volts in figs. 11(b, d and f).

The bumps in the C-V curve, however, are not due to SRH centre response but are present in most of the MIS C-V curves. They simply reflect the majority carrier response in the inversion layer. No bump is seen at very low frequencies because the majority carrier response in the inversion layer is masked by the much larger minority carrier response. No bump is seen at very high frequencies because of the decrease in the size of both the majority carrier and the minority carrier conduction current relative to the displacement current. With higher SRH densities (greater than about 10% of the doping impurity density), there will generally be a capacitance bump associated with the SRH centre charge storage. In fig. 11 the SRH density is < 1% of the dopant impurity density. Hence the C-V peaks that one might expect at .4 volts are too small to be seen.

(d) Effect of Light

As has already been noted in section 4 of this chapter, the a.c. model requires the inclusion of several active elements which attempt to return the system towards its thermal equilibrium value. The major effect of the light induced pair production process is to increase both the hole and electron densities throughout the semiconductor. This is treated in the d.c. solution by a d.c. quasi Fermi level shift (here ϕ_N) for the minority carrier band(24).

The C-V curves of fig. 11 reflect this in two ways. First, there is an improved inversion layer response resulting in a much higher value of ω_{inv}. Second, the depletion well is narrowed and its minimum is raised, much as if one were treating an equilibrium system with a smaller (by ϕ_N) bandgap.

The G-V behavior with increased illumination is much like that shown in fig. 11 for increased SRH centre density. Instead of being plotted, the voltage saturation levels, $G_{inv}(\omega)$, are given in Table 3. As with the SRH centre density, $G^V_{inv}(\omega)$ increased with ϕ_N for $\omega > \omega_{inv}$ and decreased with ϕ_N for $\omega < \omega_{inv}$. Again this results from the modification of the coupling region ΔX_c. At low frequencies the increased coupling allows a greater portion of the current to flow through the less lossy majority carrier current path. At high frequencies the increased coupling that results in a higher ω_{inv} also leads to $G^V_{inv}(\omega)$ saturating (in frequency) at a higher value of G^{ω}_{inv}.

5. Effect of Surface States on the MIS Admittance

(a) Surface State G-V and C-V Effects

Figures 14 and 15 contain C-V and G-V curves for

Figure 12 MIS C-V Curves for Different Amounts of D.C. Quasi Fermi Level Shift, ϕ_N. (All curves are for p-type 10^{15}/cc semiconductor at T = 300°K and an oxide thickness of 1000 Å. There were no surface states. Conversion from ϕ_N to the radiation induced bulk pair production rate, R_L, is given in Table 3. Other semiconductor data is given in Appendix 1.)

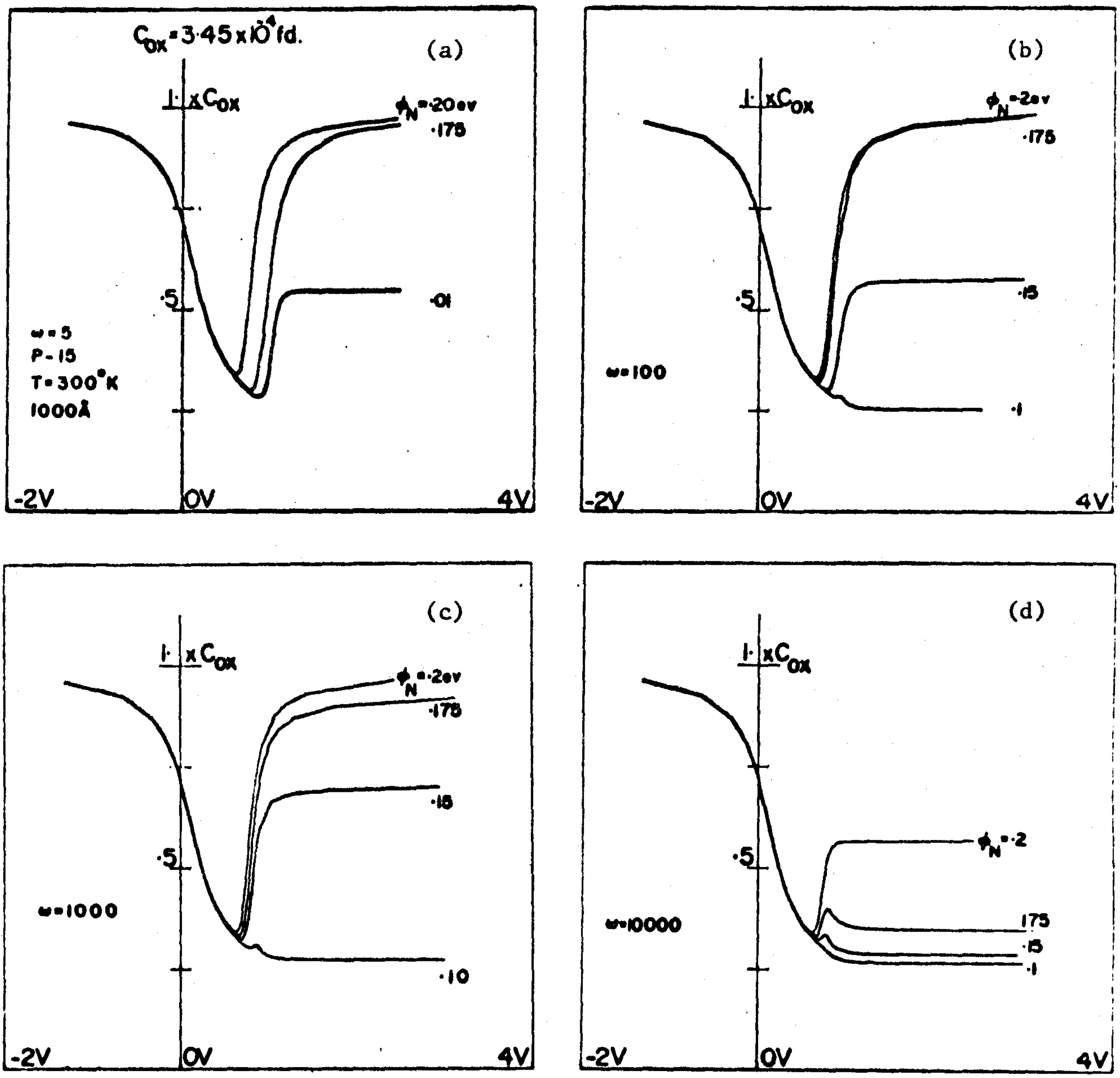
$C_{OX}=3.45\times10^{-4}$ fd.
(a)
1· xC_{OX}
ϕ_N=.20ev
.175
.01
.5
ω=5
P-15
T=300°K
1000Å
-2V
0V
4V
(b)
1· xC_{OX}
ϕ_N=.2ev
.175
.15
.1
.5
ω=100
-2V
0V
4V
(c)
1· xC_{OX}
ϕ_N=.2ev
.175
.15
.10
.5
ω=1000
-2V
0V
4V
(d)
1· xC_{OX}
ϕ_N=.2
175
.15
.1
.5
ω=10000
-2V
0V
4V

Figure 12

Table 3

G Saturation Values at Different ϕ_N (see Figure 12)

d.c. quasi Fermi level Shift, ϕ_N (in eV)	Equivalent bulk pair production rate, R_L, (no./sec/m^3)	rad. freq. ω	$\log_{10}(G_{acc})$	$\log_{10}(G_{inv})$
			(G in (mho m^2))	
.01	3.16 10^{16}	5	-11.96	-3.90
		100	-10.66	-4.93
.1	1.01 10^{20}	5	-11.96	-4.84
		100	-10.66	-3.90
		1000	- 9.66	-4.66
		10000	- 8.66	-5.66
.15	4.92 10^{21}	5	-11.96	-5.99
		100	-10.66	-4.69
		1000	- 9.66	-3.91
		10000	- 8.66	-4.53
.175	3.40 10^{22}	5	-11.96	-6.41
		100	-10.66	-5.11
		1000	- 9.66	-4.15
		10000	- 8.66	-4.15
.2	2.35 10^{23}	5	-11.96	-6.83
		100	-10.66	-5.52
		1000	- 9.66	-4.53
		10000	- 8.66	-3.92

surface state distributions "1" and "2" given in fig. 13. The distributions consist of truncated Gaussian peaks near each band edge on top of a constant distribution across the gap. For programming purposes each distribution is represented by 120 levels equally spaced in energy.

Figs. 14(a) and (c) and figs. 15(a) and (c) are the C-V and G-V curves which result when the surface state a.c. response is arbitrarily suppressed. While such curves cannot be experimentally observed, they are valuable in separating the d.c. effects of surface states from the a.c. effects. This is accomplished by setting the conductances G_{PS} and G_{NS} to zero in the equivalent circuit shown in fig. 7(c). Thus these curves reflect only the d.c. effects of the distribution, namely a widening of the depletion characteristics in both the C-V and G-V curves. The filling of surface states requires a larger increase in device voltage for the same change in semiconductor band bending. Hence the depletion well for the MIS diode with the larger midgap surface state distribution (figs. 14(a) and (b))has been broadened much more than that of the MIS diode with the smaller midgap distribution (figs. 15(a) and (b)).

The C-V and G-V curves for normal a.c. surface state response are shown in figs. 14(b), 14(d), 15(b) and 15(d). As for the case of the SRH centre discussed earlier, each surface state level is physically characterized by electron and hole emission and capture cross sections. The values used for these are given along with the other semiconductor data in Appendix 1.

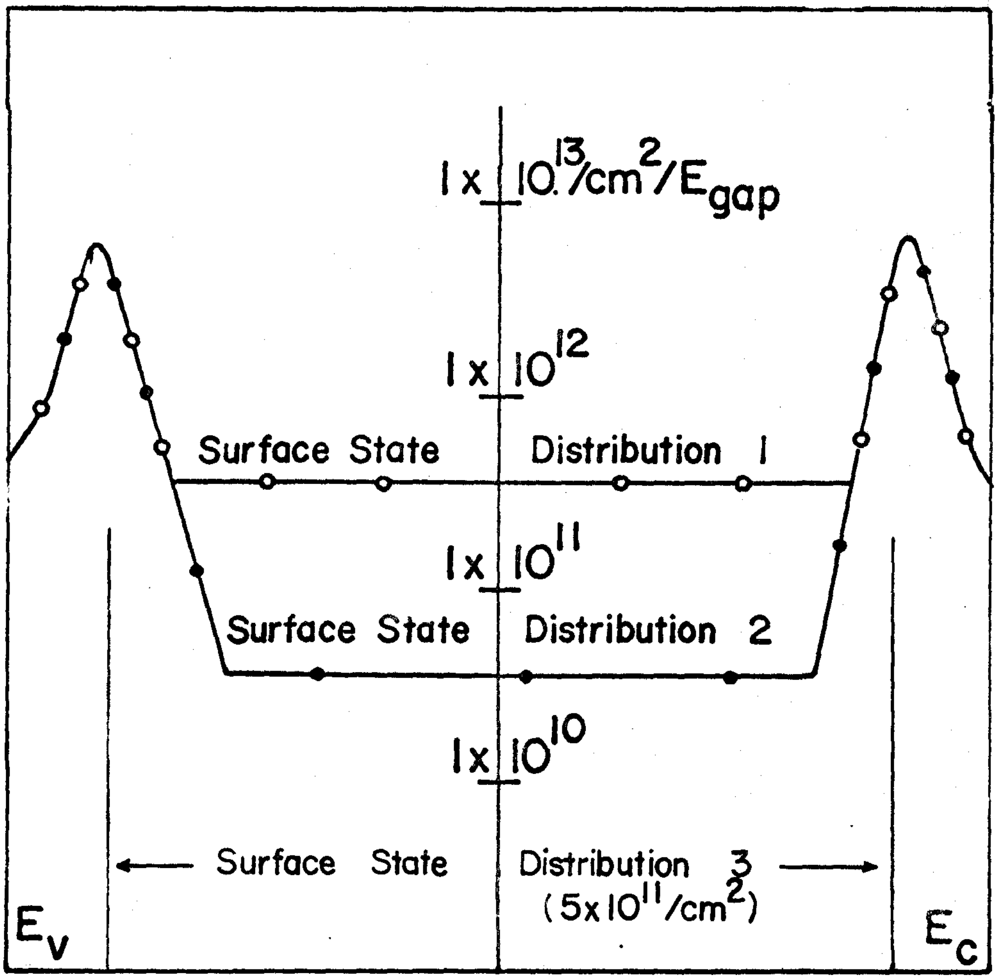

Figure 13 Surface State Distributions Used in Generating Some of the C-V and G-V Curves of Chapters III and IV. (The distributions consist of truncated Gaussian peaks near each band-edge on top of a constant level across the gap. E_v=valence band edge. E_c=conduction band edge. E_{gap} is given in Appendix 1 in eV. Distribution '3' consists of a monoenergetic density of $5x10^{11}$ positive or neutral states .93 eV from the valence band and $5x10^{11}$ negative or neutral states .93 eV from the conduction band.)

Figure 14 C-V and G-V Curves for an MIS Diode with Surface States, No SRH Traps. (All curves are for p-type 10^{15}/cc semiconductor at T = 300°K with an oxide thickness of 1000 Å. The surface state distribution is given in fig. 13 as surface state distribution 1. G is in units of mho m^2.)

(a,b) C-V and G-V d.c. effects of surface states with their a.c. response suppressed. (Elements G_{PS} and G_{NS} of the a.c. model in fig. 7c are arbitrarily set to zero.)

(c,d) C-V and G-V curves with normal a.c. response. (G_{PS} and G_{NS} are given values as defined in Appendix 2. Other pertinent semiconductor data is given in Appendix 1b).

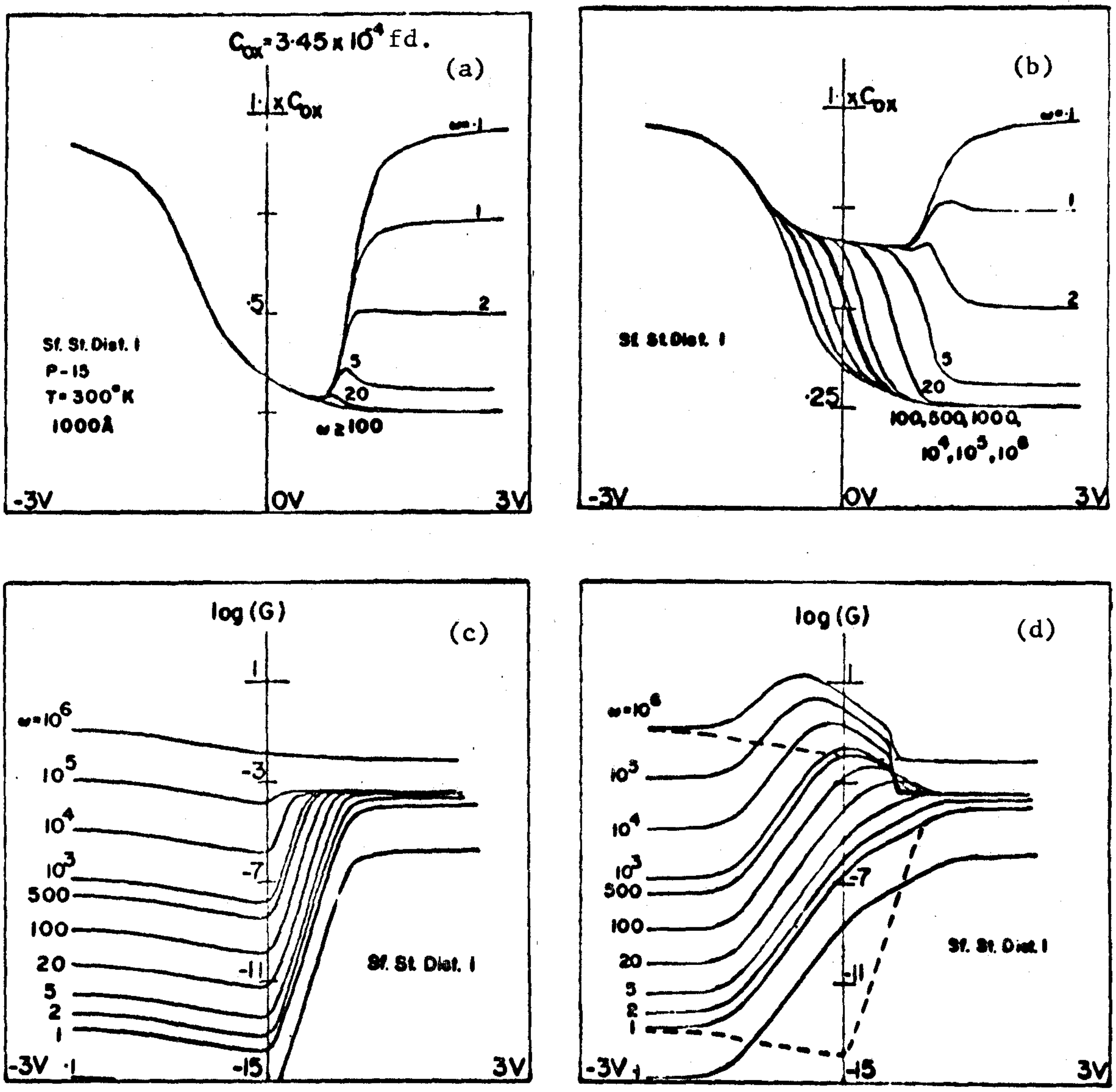
C_{ox} = 3·45 x 10^{-4} fd.
(a)
1· x C_{ox}
ω=·1
1
2
5
20
ω ≥ 100
·5
Sf. St. Dist. 1
P-15
T = 300°K
1000Å
-3V
0V
3V
(b)
1· x C_{ox}
ω=·1
1
2
5
20
·25
100, 500, 1000, 10^4, 10^5, 10^6
Sf. St. Dist. 1
-3V
0V
3V
(c)
log (G)
ω=10^6
10^5
10^4
10^3
500
100
20
5
2
1
-3
-7
-11
-15
Sf. St. Dist. 1
-3V
3V
(d)
log (G)
ω=10^6
10^5
10^4
10^3
500
100
20
5
2
1
-7
-11
-15
Sf. St. Dist. 1
-3V
3V

Figure 14

Figure 15 C-V and G-V Curves for an MIS Diode with Surface States. (All curves are for p-type 10^{15}/cc semiconductor at T = 300°K with an oxide thickness of 1000 Å. The surface state distribution is given in Fig. 13 as surface state distribution 2. G is in units of mho m^2.)

(a,b) C-V and G-V d.c. effects of surface states with their response suppressed. (Elements G_{PS} and G_{NS} of the a.c. model in Fig. 7(c) are arbitrarily set to zero.)

(c,d) C-V and G-V curves with normal a.c. response. G_{PS} and G_{NS} are given values as defined in Appendix 2. Other pertinent semiconductor data is given in Appendix 1b.

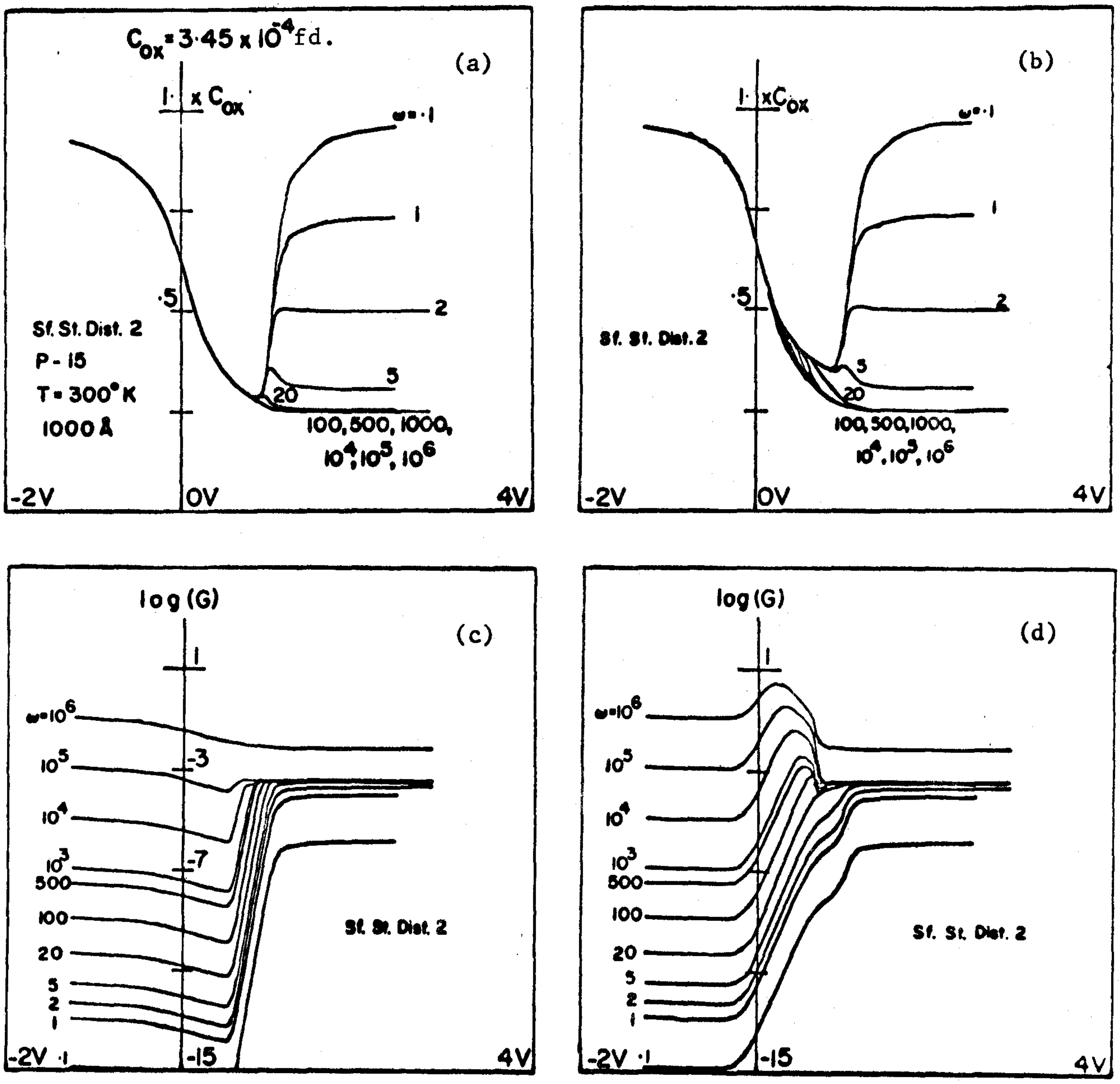
$C_{ox} = 3.45 \times 10^{-4}$ fd.
(a)
1· x C_{ox}
ω=·1
1
2
5
20
·5
100, 500, 1000,
10^4, 10^5, 10^6
Sf. St. Dist. 2
P - 15
T = 300°K
1000 Å
-2V
0V
4V
(b)
1· xC_{ox}
ω=·1
1
2
5
20
·5
100, 500, 1000,
10^4, 10^5, 10^6
Sf. St. Dist. 2
-2V
0V
4V
(c)
log (G)
1
ω=10^6
10^5
-3
10^4
-7
10^3
500
100
20
5
2
1
Sf. St. Dist. 2
-2V ·1
-15
4V
(d)
log (G)
1
ω=10^6
10^5
10^4
10^3
500
100
20
5
2
1
Sf. St. Dist. 2
-2V ·1
-15
4V

Figure 15

The effect of a particular surface state level depends chiefly on four things. First, the difference in energy of the surface state level and the Fermi level regulates the size of the surface state capacitance C_{S_i} for that level. Since C_{S_i} is proportional to the derivative of the surface state level Fermi function, levels S_i which are far (in energy) from the Fermi level have negligibly small capacitances. Thus it immediately follows that a.c. surface state current, i_S, can only flow from surface state levels relatively close to the Fermi level. Second, surface state energy with respect to the band edges controls the size of the conductances, G_{PS_i} and G_{NS_i}. G_{PS_i} is approximately proportional to $\exp(-(E_{S_i}-E_V)/kT)$ and G_{NS_i} is approximately proportional to $\exp(-(E_C-E_{S_i})/kT)$. Hence, except when limited by semiconductor minority carrier response, most of the a.c. current from the i^{th} level will flow into the closest (in energy) band. Third, the value of the radian frequency, ω, is required to establish the relative value of the capacitive admittance, ωC_{S_i}, to the conductive admittances, G_{PS_i} and G_{NS_i}. This, along with the size of the current from the i^{th} level, determines the contribution of the i^{th} level to both the capacitance and conductance of the device. Fourth, the semiconductor itself plays a role through the a.c. response of the electron and hole bands at the interface. The most important illustration of this effect can be seen in the sharp drop in conductance at about .7 volts in figs. 14(d) and 15(d). This marks the bias at which the interface is becoming inverted. The minority carrier band portion of the surface state current is now controlled by the semiconductor minority carrier response. Hence, except at frequencies below ω_{inv}, the observed surface state effects are primarily through that portion of the surface state current i_S, which flows into the majority carrier band.

The C-V curves of fig. 15(b) show what one would expect from large surface state densities(28) while the C-V curves of fig. 15(b) are more representative of the densities obtainable with present day surface preparation techniques. Both figures show the gradual cutoff in response of surface state levels farthest from the majority carrier band with increasing frequency. At $\omega = .1$ rad/sec, all of the states are responding while at $\omega = 10^6$, only states very near the majority band edge are responding.

The G-V curves of figs. 14(d) and 15(d) are more complex. First, surface state response increases with frequency due to increased capacitive admittances, ωC_{S_i}. Second, at any given frequency the surface state contribution to the device conductance goes through a maximum at a diode voltage designated as V_{peak}. At V_{peak}, the bands are bent so that the time constants of surface state levels near the Fermi level are approximately equal to $1/\omega$. This implies that the bands are bent to give, for surface state levels at the Fermi level, a capacitive admittance $\omega C_S = G'_{PS} + G'_{NS}$. The primed quantities G'_{PS} and G'_{NS} serve to emphasize the modification of surface state time constant, τ_S, by the semiconductor. For example, in N-type semiconductor, $G'_{NS} = G_{NS}$, while, for $\omega > \omega_{inv}$, lack of semiconductor minority carrier response causes G'_{PS} to approach zero. Third, the peak shifts toward accumulation voltages as the frequency increases, bending the majority band at the interface closer to the Fermi level. Therefore the surface state levels near the Fermi level at this new value of interface band bending are also closer to the majority carrier band. Hence they have a correspondingly larger value of $G_{NS(or\ PS)}$ and a correspondingly smaller time constant, τ_S. The amount of the shift in V_{peak} can be approximately inferred from the change in interface band bending required to give $\omega\tau_S = 1$.

In the G-V curves of fig. 14(d) the "background" conductances at two frequencies have been reproduced (from fig. 14(c)) as the dashed lines. This helps to illustrate more clearly the a.c. conductance contribution of surface states. Similar capacitance "background" can be removed from the C-V curves of figs. 14(b) and 15(b) using figs. 14(a) and 15(a) respectively.

(b) The Effect of Temperature

The behavior of the C-V curves with temperature shown in fig. 16 is similar to the ideal, surface state free cases previously described in Section 5b of this chapter and shown in fig. 10. Minority carrier response increases with increasing temperature giving a higher value of ω_{inv}. In addition, increasing the temperature leads to increased capacitive response

Figure 16 Effect of Temperature on the MIS C-V and G-V Response, No SRH Traps. (Surface state distribution 2 is plotted in Fig. 13. The semiconductor is p-type 10^{15}/cc. T = 300°K and oxide thickness is 1000 Å. Other semiconductor data is given in Appendix 1d. G is in units of mho m^2.)

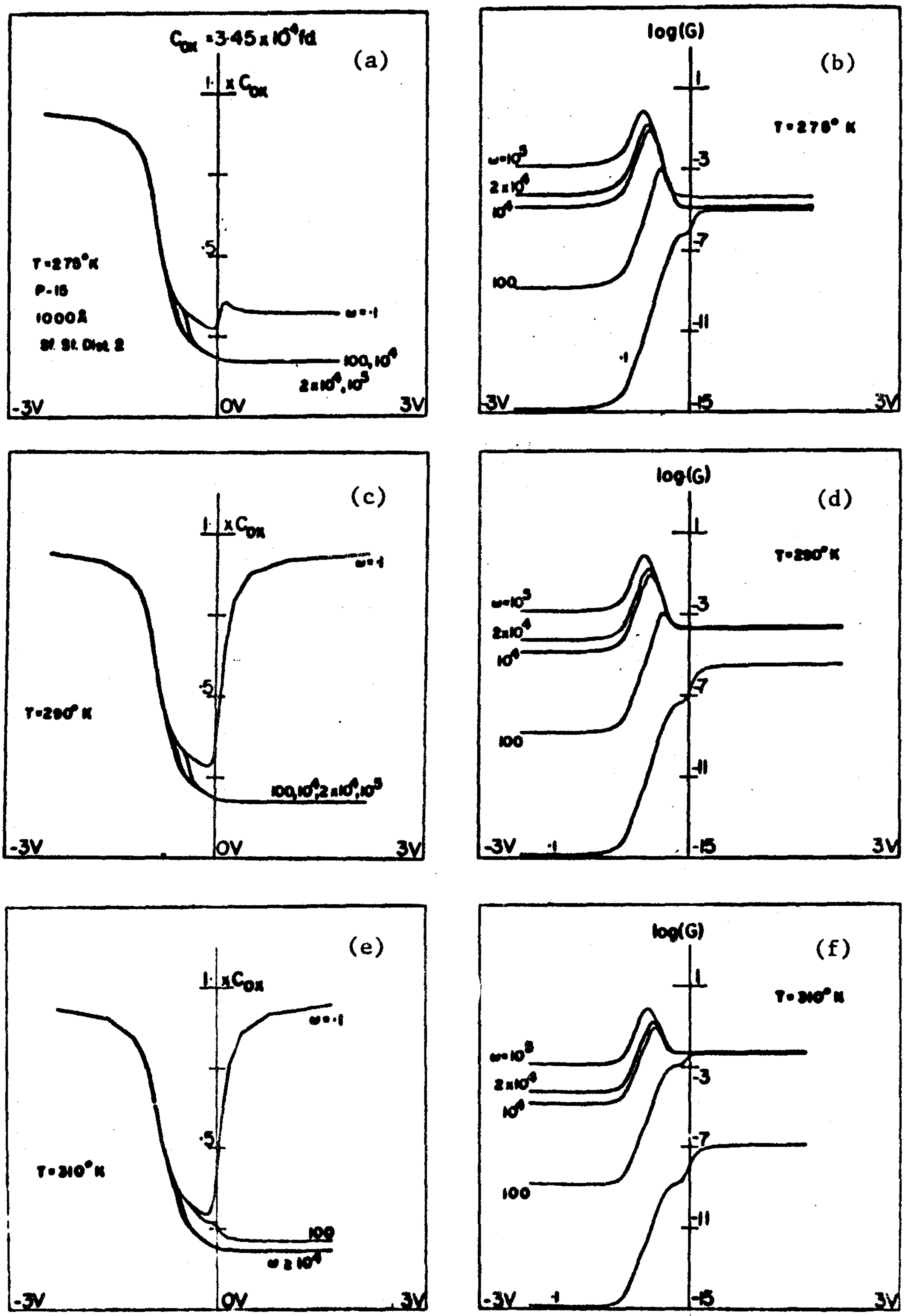
(a)
C_OX = 3.45 x 10^-4 fd
1. x C_OX
.5
T = 278° K
P-15
1000Å
St. St. Dist. 2
ω = 1
100, 10^4
2x10^4, 10^5
-3V
0V
3V
(b)
log(G)
T = 278° K
ω = 10^5
2x10^4
10^4
100
1
1
-3
-7
-11
-15
-3V
3V
(c)
1. x C_OX
.5
T = 290° K
ω = 1
100, 10^4, 2x10^4, 10^5
-3V
0V
3V
(d)
log(G)
T = 290° K
ω = 10^5
2x10^4
10^4
100
1
1
-3
-7
-11
-15
-3V
3V
(e)
1. x C_OX
.5
T = 310° K
ω = 1
100
ω ≥ 10^4
-3V
0V
3V
(f)
log(G)
T = 310° K
ω = 10^5
2x10^4
10^4
100
1
1
-3
-7
-11
-15
-3V
3V

Figure 16

(at the bottom of the C-V depletion well) by allowing states which are further away from the majority carrier band to respond.

The G-V inversion saturation values, $G^V_{inv}(\omega)$, reflect the increase in ω_{inv} with temperature. For frequencies below ω_{inv}, G^V_{inv} decreases with increasing temperature. This is due to smaller bulk and depletion layer minority carrier resistivities and correspondingly smaller losses along the low frequency minority carrier current path shown in fig. 8. At frequencies above ω_{inv}, device conductance increases with temperature reflecting the increased current in the high frequency path of the coupling region, ΔX_c, shown in fig. 8.

Although parameters such as effective mass and mobility vary with temperature, the most important effects result from the change in kT in the Fermi functions. For a fixed surface state density, there is a linear reduction, with decreasing temperature, in the number of surface state levels effectively contributing to the a.c. surface state response. However, the loss components between the two bands and the surface state (G_{NS_i} and G_{PS_i}) shown in fig. 7(c) decrease even faster since they are approximately proportional to $\exp(-|E_{band}-E_{S_i}|/kT)$. The result is a voltage shift of the conductance peak towards accumulation such that the majority carrier band at the IS interface is bent closer to the Fermi level. This is illustrated in fig. 17(b) which shows G-V curves at $\omega = 100$ for four temperatures. Note also that the flatband bias point

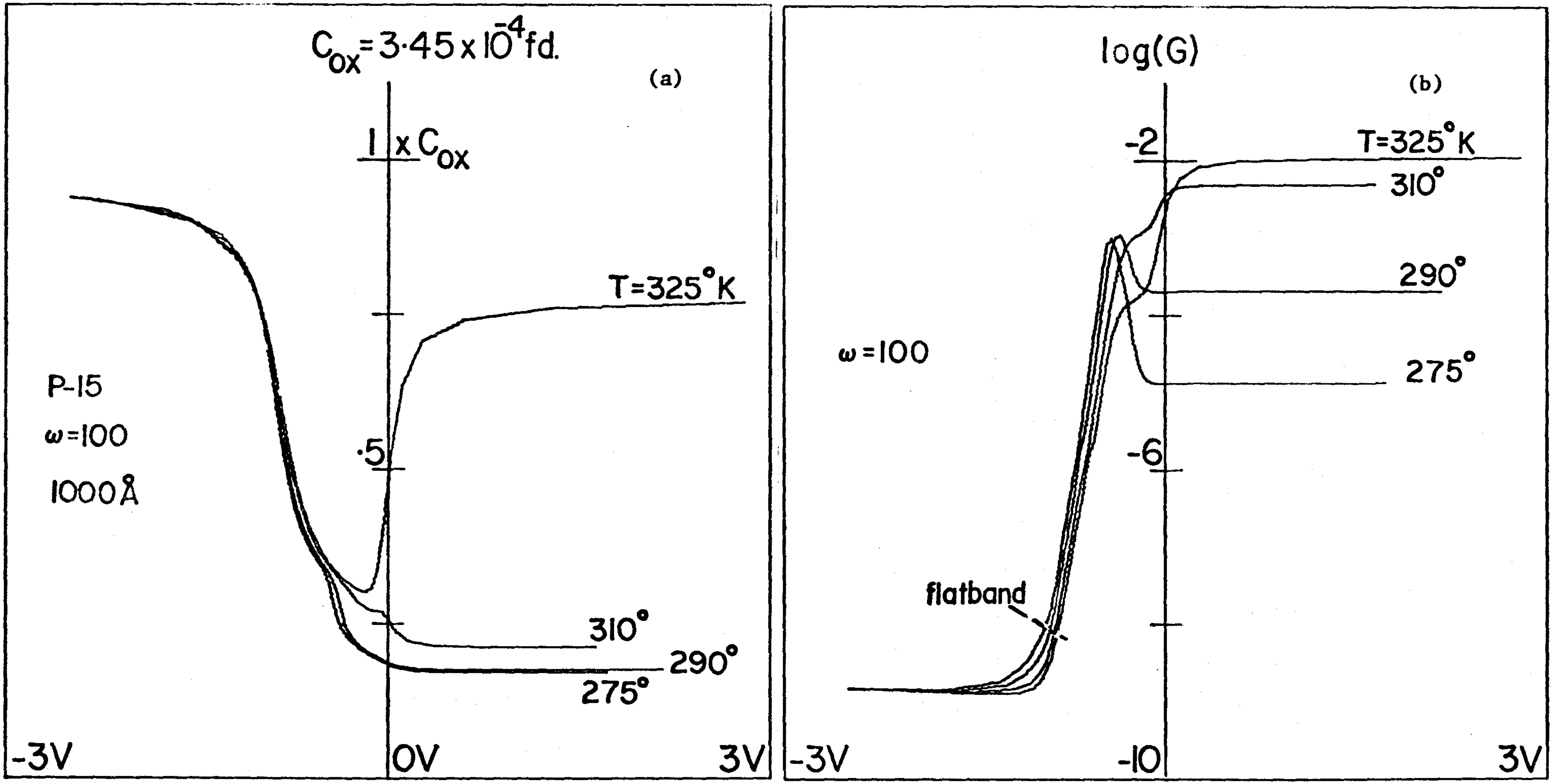

Figure 17 MIS C-V and G-V Curves at a Fixed Frequency, as a Function of Temperature. (The semiconductor data is identical to that given for Fig. 16, ie. Surface State Distribution 2 of Fig. 13. No SRH traps, and semiconductor data as given in Appendix 1d. G is in units of mho m^2).

changes with temperature. This shift is a d.c. effect due to charged surface states and is the basis of the temperature method for determining surface densities(19) near flatband.

(c) Contact Effects

Contact effects have been included in the a.c. model shown in fig. 7(a) by inserting complex admittances Y_{NC}, Y_{PC} and Y_{KC} in the electron, hole, and displacement current paths respectively. For all of the C-V and G-V curves, these have been chosen to simulate an "ideal" contact, ie. Y_{NC} and Y_{PC} almost short circuit [$Y_{NC} = (10^8,0)$ and $Y_{PC} = (10^8,0)$] and Y_{KC} an open circuit. The G-V curves of fig. 18 were generated with the same Y_{PC}, Y_{NC} and Y_{KC} values but with a small series resistance, R, in the external circuit.

In fig. 18(a) the radian frequency, ω, was fixed and R varied. In fig. 18(b), R was fixed and ω varied. G-V effects in both figures can be understood in terms of the resistance, R, in series with a pure capacitor, C. With $1/R >> \omega C$, the conductance of such a circuit behaves as $\omega^2 C^2 R$. This is illustrated in fig. 18(a) for R values greater than 10^{-7} Ω/m^2. The saturation of G for R values $\leq 10^{-7}$ Ω/m^2 indicates the <u>true</u> conductance of the MIS diode. One can also infer that (at $\omega \leq 10^5$ for the MIS diode shown in fig. 18(a)) contacts with $R < 10^{-7}$ can effectively be termed ideal. On the inversion side of fig. 18(b) $1/R >> \omega C$ for all of the frequencies shown. With fixed R, and with C approximately given by the high frequency inversion capacitance the device conductance increases

Figure 18 Effects of a Resistance, R, in Series with an Ideal (Ohmic) Contact on the G-V Inversion and Accumulation Saturation Levels. (The semiconductor is p-type 10^{15}/cc. The temperature is indicated in the figure. G is in units of mho m^2.)

(a) Effect of varying R with frequency fixed.

(b) Effect of varying frequency with R fixed.

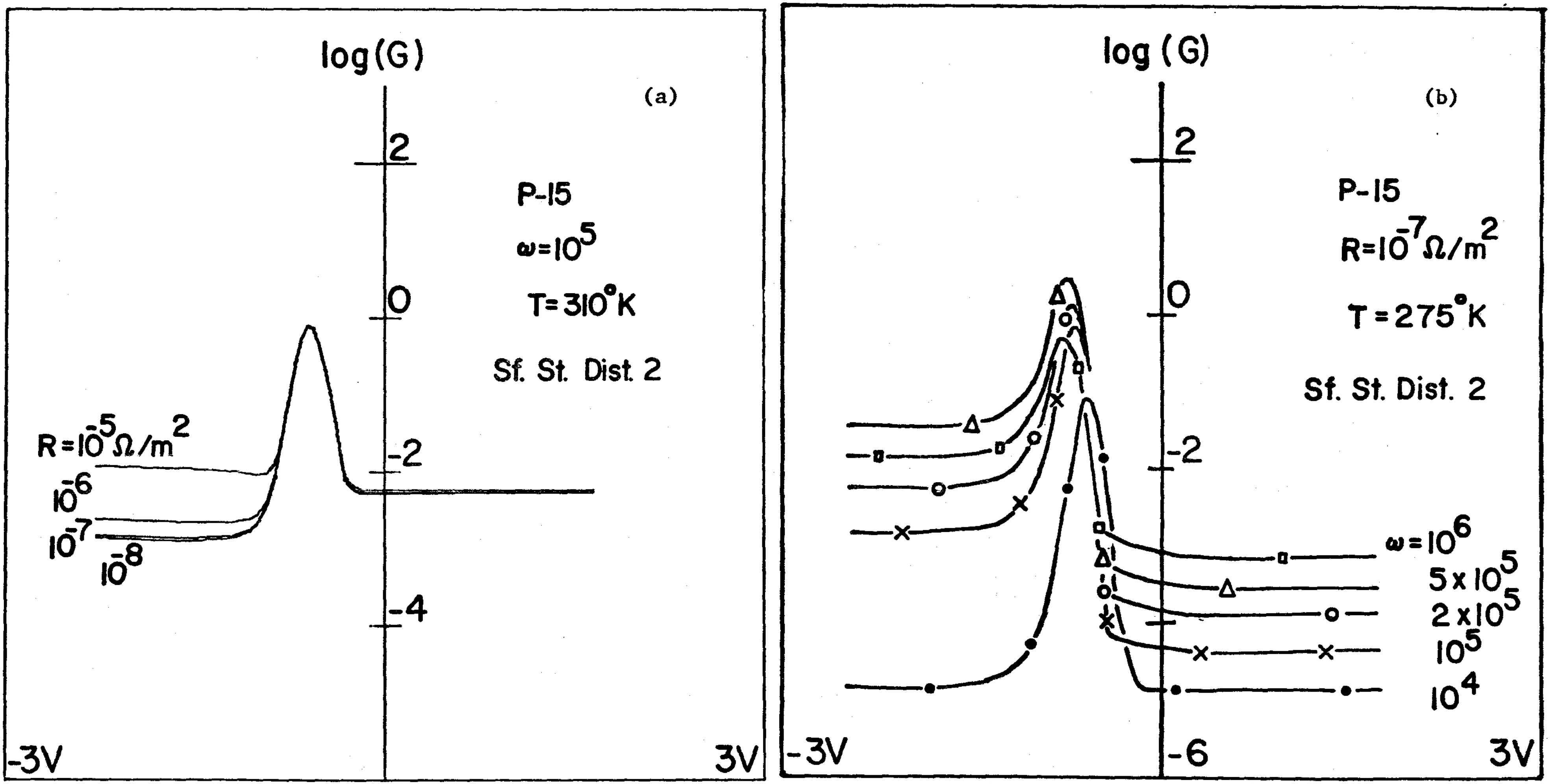
log(G)
(a)
2
0
-2
-4
P-15
ω=10^5
T=310°K
Sf. St. Dist. 2
R=10^-5 Ω/m^2
10^-6
10^-7
10^-8
-3V
3V
log (G)
(b)
2
0
-2
-6
P-15
R=10^-7 Ω/m^2
T=275°K
Sf. St. Dist. 2
ω=10^6
5x10^5
2x10^5
10^5
10^4
-3V
3V

Figure 18

as ω^2. In accumulation, the capacitance is much larger (approximately C_{ox}) and the inequality holds only to an ω of about 5×10^5. At higher frequencies the inequality reverses and the behaviour of the simple series network predicts a response falling with increasing frequency to a value of 1/R. Physically this is indicative of current being limited by R and can be seen in fig. 18(b) in going from $\omega = 5 \times 10^5$ to $\omega = 10^6$ rad/sec.

6. MIS Impurity Band Response at Low Temperature

The effects of impurity band response at low temperatures are illustrated in fig. 19 where C-V curves are plotted as a function of doping density, frequency, and temperature. The impurity profile, g(E), as given in equation (1) is Gaussian(25). Band tailing effects have also been included(25) and the relevant data for the different cases considered in fig. 19 is listed in Table 4. Surface state distribution 2 (see fig. 13) was used in all curves.

An immediate consequence of the small kT value at low temperatures can be seen in the appearance of surface state capacitance bumps in the low frequency C-V curves (denoted by symbol SF in fig 19. These surface state bumps correspond to the surface state density peaks in the distribution. At low temperature these peaks are far enough from the band edges (in kT) to be observed. At $\omega = 10^6$ the surface states are unable to response and the capacitance bumps disappear.

Figure 19 MIS Dopant Band and Surface State Effects at Low Temperatures (See Appendix 1 for semiconductor parameters at 50°K, 63°K, 88°K and 112°K. SF and IMP denote surface state and impurity band peaks respectively).

(a,b) Response as a function of frequency. (p-type 10^{18}/cc semiconductor with 1000 Å oxide).

(c,d) Response as a function of temperature. (p-type 10^{18}/cc semiconductor with 1000 Å oxide).

(e,f) Response as a function of doping density. (Oxide thickness is 1000 Å, the frequency, ω, is 10^6 and the temperature is 50°K. Note that P17, 5P17 and P18 denote p-type 10^{17}/cc, 5 x 10^{17}/cc and 10^{18}/cc semiconductor respectively).

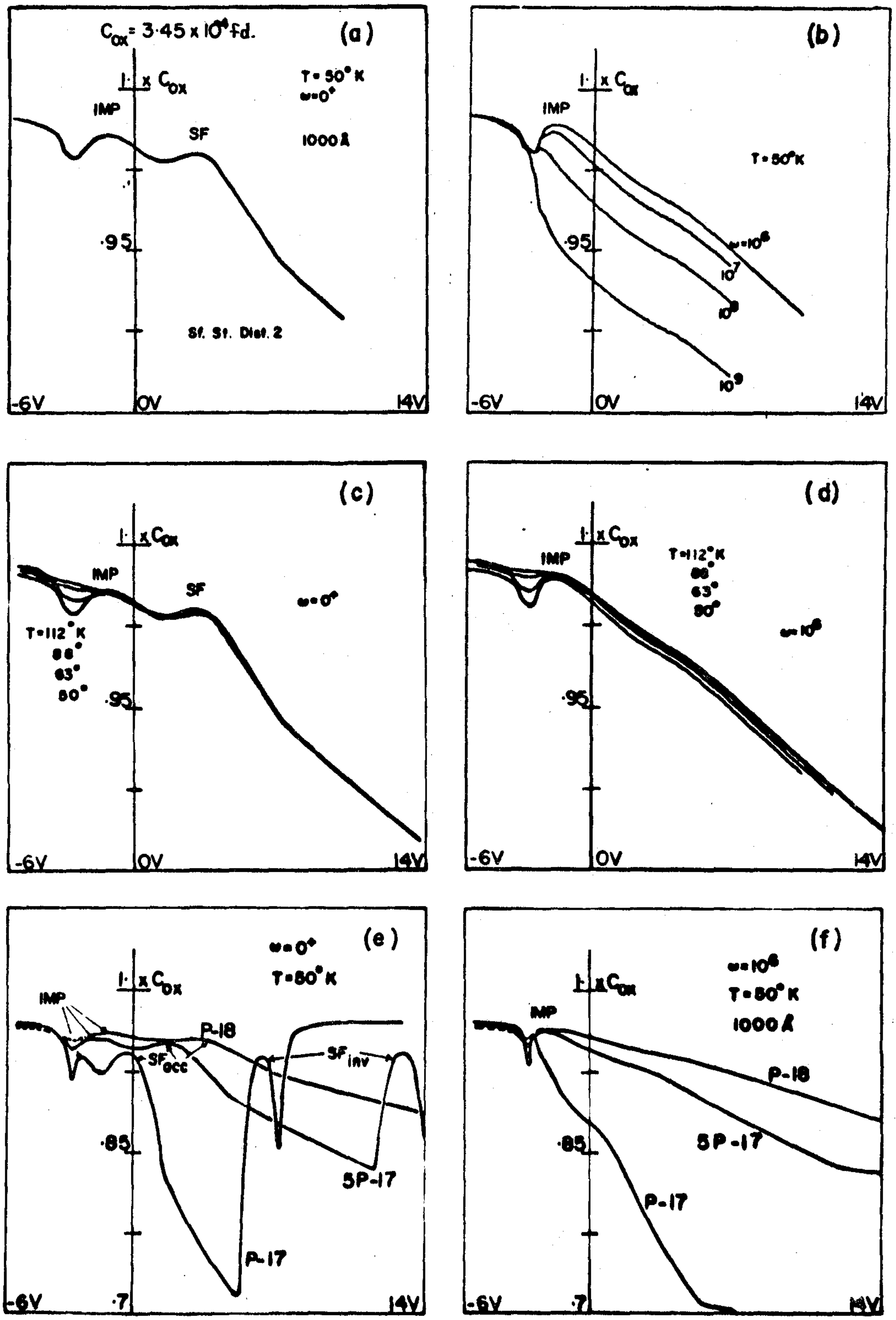
(a)
$C_{ox} = 3.45 \times 10^{-4}$ fd.
1· x C_{ox}
T = 50° K
ω = 0°
1000 Å
IMP
SF
·95
Sf. St. Dist. 2
-6V
0V
14V
(b)
1· x C_{ox}
IMP
T = 50° K
ω = 10^6
10^7
10^8
10^9
·95
-6V
0V
14V
(c)
1· x C_{ox}
IMP
SF
ω = 0°
T = 112° K
88°
63°
50°
·95
-6V
0V
14V
(d)
1· x C_{ox}
IMP
T = 112° K
88°
63°
50°
ω = 10^6
·95
-6V
0V
14V
(e)
ω = 0°
T = 80° K
1· x C_{ox}
IMP
P-18
SF_{occ}
SF_{inv}
·85
5P-17
P-17
-6V
·7
14V
(f)
1· x C_{ox}
ω = 10^6
T = 80° K
1000 Å
IMP
P-18
5P-17
P-17
·85
-6V
·7
14V

Figure 19

Table 4

Band Tailing and Dopant Impurity Line Broadening for a Gaussian Distribution With Variance σ (see Figure 19)

Doping Density (per cm^3)	Band Tailing	Temperature (°K)	$2\sigma^2$
10^{18} p-type	2.713 kT	50°	15.97 $(kT)^2$
	.0117 eV		$2.94\text{x}10^{-4}$ $(eV)^2$
10^{18} p-type	2.145 kT	63°	9.90 $(kT)^2$
	.0117 eV		$2.95\text{x}10^{-4}$ $(eV)^2$
10^{18} p-type	1.529 kT	88°	5.02 $(kT)^2$
	.0117 eV		$2.94\text{x}10^{-4}$ $(eV)^2$
10^{18} p-type	1.198 kT	112°	3.08 $(kT)^2$
	.0117 eV		$2.95\text{x}10^{-4}$ $(eV)^2$
5 x 10^{17} p-type	2.032 kT	50°	8.88 $(kT)^2$
	.00875 eV		$1.64\text{x}10^{-4}$ $(eV)^2$
10^{17} p-type	1.039 kT	50°	2.32 $(kT)^2$
	.00448 eV		$4.28\text{x}10^{-5}$ $(eV)^2$

Though normally masked by the majority band, at low temperatures it becomes possible to observe the capacitance response of the dopant band. The result is a capacitance peak occurring at that value of interface bending for which the impurity dopant band is bent through the Fermi level. (These are denoted in fig. 19 by the symbol IMP.) Figs. 19(c) and (d) illustrate this concept. As the temperature is raised the dopant capacitance bump disappears into the increased majority band background response.

If band tailing and dopant line broadening are small enough to leave a distinct gap between the majority carrier band and the dopant band, it will be possible, as shown in fig. 19(b), to see the disappearance of the dopant C-V bump with increased frequency. This occurs as the majority carrier communication with the impurity band begins to lag behind the a.c. signal.

Figures 19(e) and (f) show the effect of doping density. The higher the doping density, the more band broadening and the larger and broader the peak which must be superimposed on the accumulation wall of the depletion characteristic. As a result, the lower doping density C-V curve exhibits a smaller but more distinct peak.

A number of problems have been skirted here by keeping the doping density low enough to ensure distinct impurity and majority carrier bands. The higher doping situations must be treated with more care and some progress has been made in this direction(25,26,30,60,62).

7. Summary of the MIS Diode A.C. Admittance Behaviour

The transmission line model of the semiconductor(2,3) has been solved with the aid of a computer*. SRH impurity effects and surface states have been included at the IS interface. Used in conjunction with an accurate d.c. analysis(1), C-V and G-V curves can be calculated at any frequency. Various features of the d.c. solution also allow analysis of low temperature effects such as dopant impurity response. The areas investigated in this part of the thesis have been those in which the simpler parametric models of previous investigators were most prone to error.

First, minority carrier response was studied as a function of doping density, temperature, SRH centre density and light induced pair production. In terms of C-V and G-V curves, typical minority carrier response is observed with the system biased in inversion. Voltage saturation is also seen in both C and G. Both the C_{inv} and G_{inv} frequency dependences are best understood in terms of a low frequency (LF) path (as opposed to a high frequency (HF) path) for a.c. minority carrier current from the inversion layer (through the depletion and bulk regions) to the contact (see fig. 8). At low frequencies the a.c. current is limited by the low ωC reactance values and hence increases with

---

*The program is written in Fortran IV and on a CDC 6400 computer and generates the d.c. solution in 30 seconds. The surface state free a.c. solution takes 30 seconds longer. For 120 surface state levels and 10 SRH levels, the a.c. solution requires 100 seconds.

frequency. Thus device conductance in this frequency range, due to dissipation by depletion and bulk minority carrier resistivity, increases with frequency. However, as the frequency is increased past ω_{inv}, the predominant interface current follows the HF path through ΔX_c, where the resistivities are much smaller and the contribution to device conductance also very small. Thus $G^V_{inv}(\omega)$ appears to saturate as a function of frequency at G^ω_{inv}.

Inserting SRH centres modifies the admittance in the coupling region, ΔX_c. At low frequencies the additional LF minority carrier path connecting the bands (through G_{PR} and G_{NR} of fig. 7(d) yields a lower net device conductance by lowering the depletion and bulk minority carrier conduction current. At high frequencies the increased coupling in ΔX_c, allows a larger current. Hence the high frequency device conductance saturation level, G^ω_{inv} increases.

Since minority carrier response is increased with SRH density, the cut off frequency for minority carrier response, ω_{inv}, also increases as shown by the C-V curves and the G-V curves. Both raising the temperature and illuminating with light increase minority carrier response and the same sort of C-V and G-V effects are seen. That is, for $\omega > \omega_{inv}$, G^V_{inv} increased with T (fig. 16) and with ϕ_N (Table 3). For $\omega < \omega_{inv}$, G^V_{inv} decreased.

The second area of investigation involved the effect of surface states. Two different distributions were investigated as a function of frequency and temperature. C-V and G-V curves are given for two cases: (1) suppressed a.c. surface state response,

(2) normal surface state response through G_{SP} and G_{SN} (see fig. 7(c).

Third, the investigation of dopant impurity C-V response, given in fig. 19, shows an impurity capacitance bump which separates from the accumulation wall of the depletion well as the temperature decreases. This response is frequency dependent, being cut off at high frequencies when the majority carriers cannot communicate fast enough with the impurity band.

These three applications demonstrate the usefulness of an accurate a.c. solution (derived from first principles) in predicting semiconductor behaviour with respect to virtually any space charge, bulk, or contact effect. Even the difficult non equilibrium case, a.c. problem is soluble if the d.c. solution is available. Thus there exists the possibility of C and G fits to experimental data to determine such constants as hole and electron capture cross sections of SRH centres, doping impurity bands and surface states. An improved semiconductor analysis also allows better calculation of surface state densities.

The theoretical problems which remain are related to the d.c. solution - whether the system is in thermal equilibrium, and if it is not, whether there exists some simple relationship to the equilibrium solution (such as the d.c. quasi Fermi level shift in section 7d). The practical problems in fitting experimental data lie in the failure of the real device to be planar, for example, and the demonstrated fact that for a given device voltage there may be a considerable variation in IS interface band bending over the cross sectional area. This evidently "softens" all experimental C-V and G-V curve features and the best theoretical approach, without going to a three dimension solution, is to consider the average properties of an ensemble of MIS devices with a Gaussian distribution of either interface band bending or oxide voltage at a fixed device voltage. Naturally the effect of lateral response will be only approximately accounted for in the Gaussian half width of the distribution*.

A second experimental problem, somewhat related to the one above, is the question of a.c. signal amplitude. It is required to be infinitesimal by theory but is necessarily finite for experiment. In the low frequency range this particular problem can be resolved to some extent by taking an ensemble average over devices which have a d.c. voltage distribution reflecting the time distribution of the a.c. sine wave voltage**.

---

* Figure 20 shows the effect of such an averaging on one of the C-V curves of Figure 16(a) for four values of variance, $\sigma_{1/2}$.

**See fig. 21 for an example of the amplitude averaging technique at four different a.c. signal amplitudes.

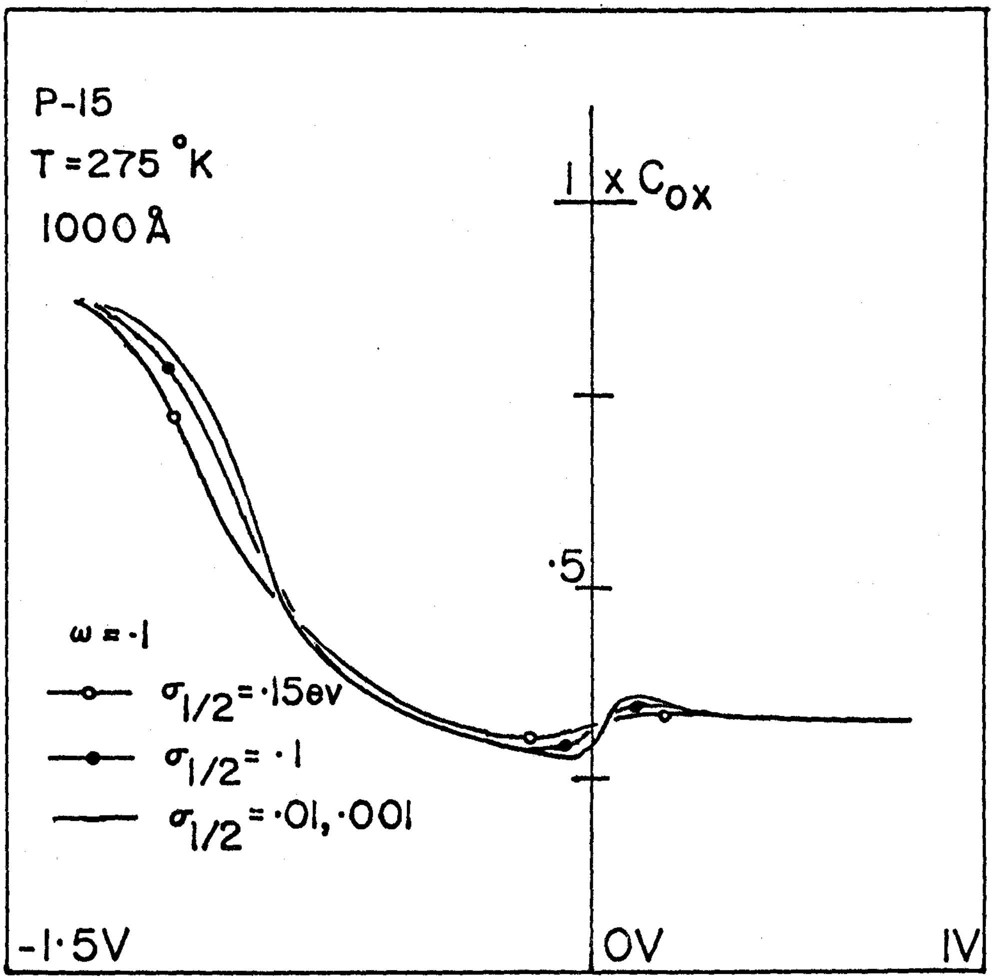

Figure 20 The Effect of a Gaussian Weighted Average Over Oxide Voltage. ($\sigma_{1/2}$ is the Gaussian variance. See Fig. 16(a) for original unaveraged curve).

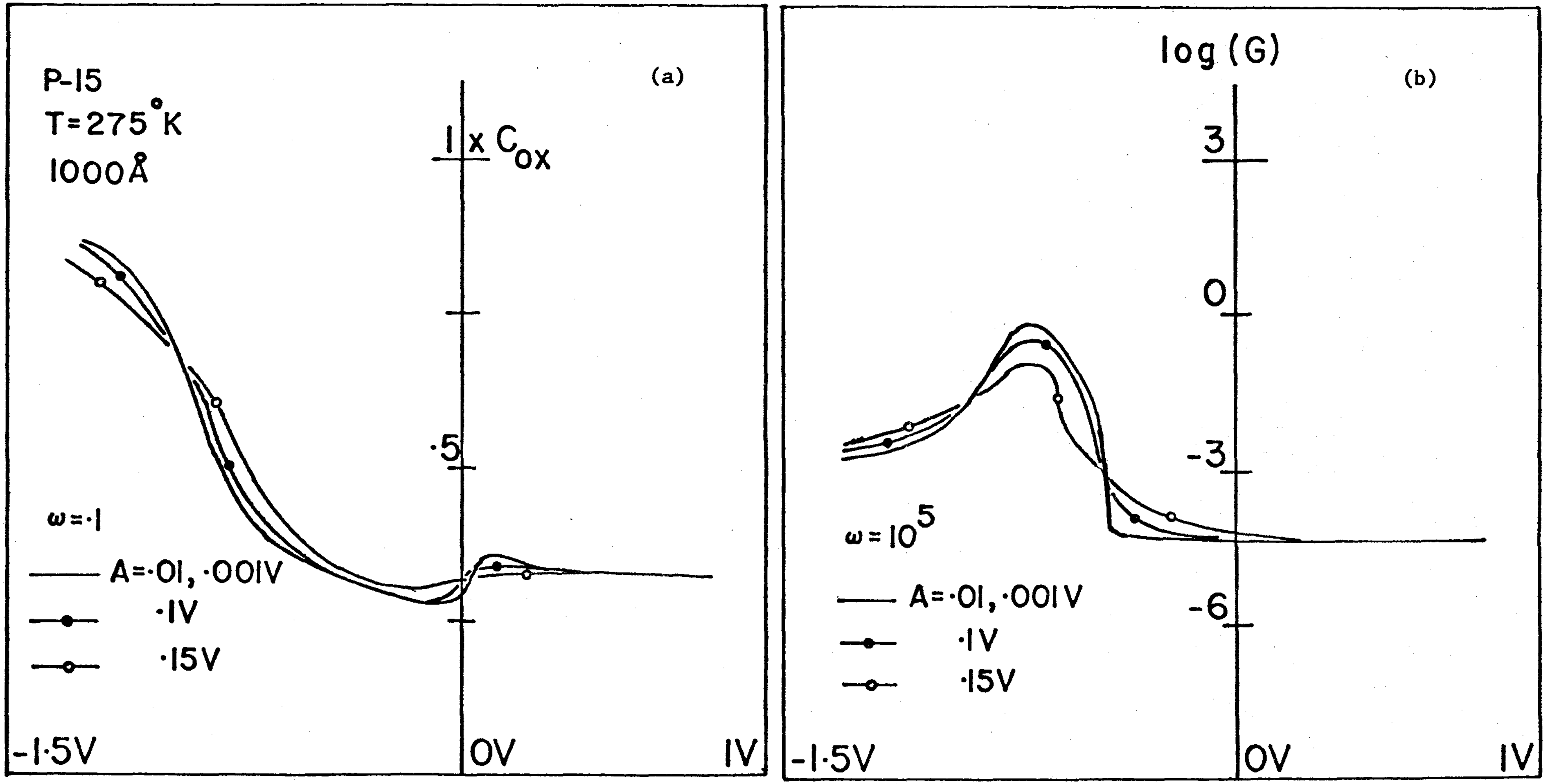

Figure 21 The Effect of a Weighted A.C. Signal Amplitude Averaging (A is the a.c. signal amplitude. See Figures 16(a) and (b) for the original unaveraged curves.)

CHAPTER IV

EXACT A.C. ADMITTANCE OF THE SIS DIODE

1. Introduction to the SIS A.C. Solution

Although a great deal of work has been done on the MIS (Metal-Insulator-Semiconductor) device, much less interest has been shown in other semiconductor-insulator sandwiches. In particular, the SIS (Semiconductor-Insulator-Semiconductor) structure has received little attention despite the fact that it has a number of interesting features which might be utilized in building new types of varactor diodes(1,3,34). In active device applications, for example, one might utilize the fact that there are two semiconductor-insulator interfaces jointly controlled by a single bias voltage.

The SIS device study given in this chapter is a natural application of the exact solution of the d.c. bias (electrostatic potential) problem given in Chapter II and the exact solution of semiconductor transmission line model given in Chapter III. Although the SIS device was treated breifly in Chapter II, only the low frequency limit SIS capacitance-voltage characteric could be obtained. The purpose of this chapter is to apply the a.c. solution method described previously for the MIS device$^{(3)}$ to obtain the exact complex admittance as a function of frequency for the SIS diode.

In the following sections the features of the d.c. and the a.c. solutions will be described briefly along with SIS admittance characteristics as a function of surface state density, Shockley-Reed-Hall (SRH) impurity density, temperature, doping density and fixed oxide-charge effects. In addition, one example is given of a non-equilibrium condition caused by light generated hole-electron pairs.

Some of the features, particularly the unusual C-V response, have been observed experimentally and can be found in an experimental paper on the SIS device behaviour$^{(59)}$.

2. The D.C. Problem

When a d.c. bias is applied across an SIS diode, a portion of the voltage appears across the insulator and the remainder across the semiconductors. For the device in thermal equilibrium, the voltage variation and corresponding semiconductor band bending are related to the charge density through Poisson's equation (see fig. 22 for a simple band bending diagram).

Since the d.c. solution used in this chapter has been derived and discussed in detail in Chapter II, only a brief enumeration of some of its features will be listed. These include: 1. prespecified accuracy, 2. Fermi statistics and integration over the density of states for conduction, valence and impurity band contributions to the charge density, 3. applicability at any temperature provided correct energy band parameters are available, 4. inclusion of SRH (Shockley-Read-Hall) recombination centers, 5. inclusion of any surface state distribution at the insulator-semiconductor interfaces, and 6. inclusion of any amount of fixed or static oxide-charge at arbitrary distances into the oxide or insulator. The curves generated here use the semiconductor data, nominally silicon, given in Appendix 1.

3. The A.C. Problem

The most useful electrical experimental measurements made on the SIS device are of the complex small signal admittance as a function of d.c. applied bias and frequency. The theoretical problem involves the dynamics of the charge redistribution and requires the solution of the small signal transport equations in a non-uniform electric field. The exact electrical analog of the a.c. transport equations is a transmission line and the resultant equivalent circuit model, under equilibrium condition, has been derived in Chapter III and is shown in fig. 7.

The basic idea behind the a.c. small signal model lies in the linearization of the transport equations when expanded about the d.c. equilibrium solution at any point, x, in the semiconductor. Hence the parameters of the a.c. model are completely determined by the d.c. solution and are time independent. The addition of recombination centers and surface states into the model are shown in figs. 7(b) and (c). In Chapter III, an exact solution of this model was utilized in deriving admittance solutions for the MIS device. This solution will be applied here in obtaining the SIS G-V (conductance-voltage) and C-V (capacitance-voltage) response for a number of SIS devices.

After obtaining the d.c. solution at a particular applied bias, the a.c. solution for each semiconductor is calculated and the device admittance can be expressed as:

$$Y_{dev} = \frac{Y_{S1}Y_{ox}Y_{S2}}{Y_{S1}Y_{S2} + Y_{S1}Y_{ox} + Y_{ox}Y_{S2}} \tag{26}$$

where $Y_{S1} = (G_{S1}, \omega C_{S1})$ is the admittance of semiconductor 1

$Y_{S2} = (G_{S2}, \omega C_{S2})$ is the admittance of semiconductor 2

$Y_{ox} = (0, \omega C_{ox})$ is the admittance of the oxide

and $Y_{dev} = (G_{dev}, \omega C_{dev})$ is the admittance of the device.

Note that the convention for labeling semiconductors 1 and 2 is defined in fig. 22. A feature of the a.c. solution is its ability to permit the surface states to either respond normally or be arbitrarily suppressed. A comparison of these two cases is useful in determining the true contribution of surface states to both the C and G curves.

4. General SIS C-V Features

Temple and Shewchun$^{(1,3)}$ have pointed out that the

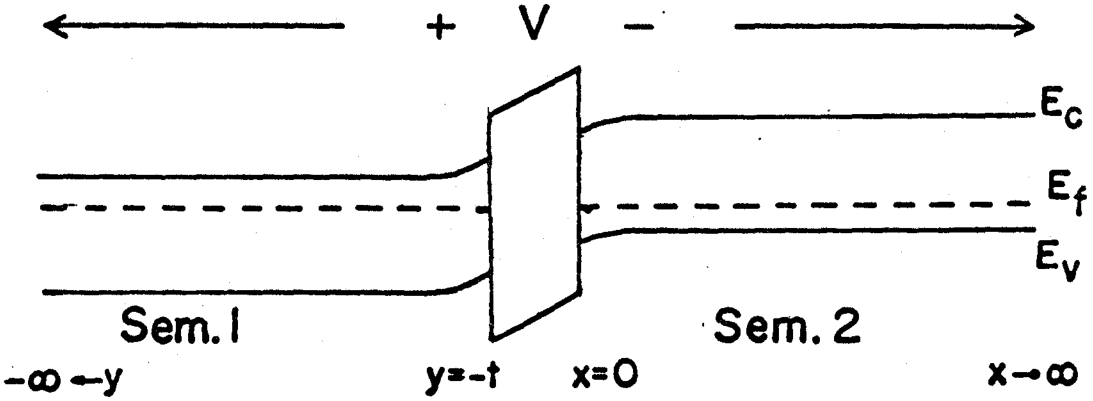

Figure 22 Simple Band Bending Model of SIS System.

complexity of the SIS electrical characteristics which makes it attractive for application, also makes analysis more complicated. There are two semiconductors whose interfaces may be biased in accumulation, depletion or inversion. Each C-V curve contains two depletion minima which, in general, occur over different ranges of applied bias and can, therefore, be separately identified*. Oxide and surface state charges shift the relative positions of the depletion wells so that a number of combinations exist. These combinations are given schematically in fig. 23 which is referred to frequently in the following sections of this paper. Note that the "depletion wells" of fig. 23 are shown as triangular with the expected high frequency response given by the dashed curves. The high frequency response in regions of single inversion falls to a level determined by the minority carrier response of the 'inverted' semiconductor,while response in regions of double inversion falls to a level determined by the minority carrier response of both semiconductors.

5. General SIS G-V Features

The G-V curves given in this paper have been obtained by plotting the real part of the device admittance, G_{dev}, against device voltage. Expanding equation 26 in terms of the real and

---

*Only in the case of equal doping density and the correct combination of surface and oxide charge will the depletion bias ranges coincide with only one deep, broad well.

Figure 23 Schematic Showing Possible Types of Low and High Frequency SIS C-V Responses. The schematic assumes equal dopant densities on both sides. ACC, INV, and DEP refer to accumulation, inversion and depletion respectively. "1" and "2" identify the semiconductor. Semiconductor "1" is the fixed reference. The solid lines represent the low frequency response and the dashed lines represent high frequency response.

SCHEMATIC LF AND HF C-V RESPONSE

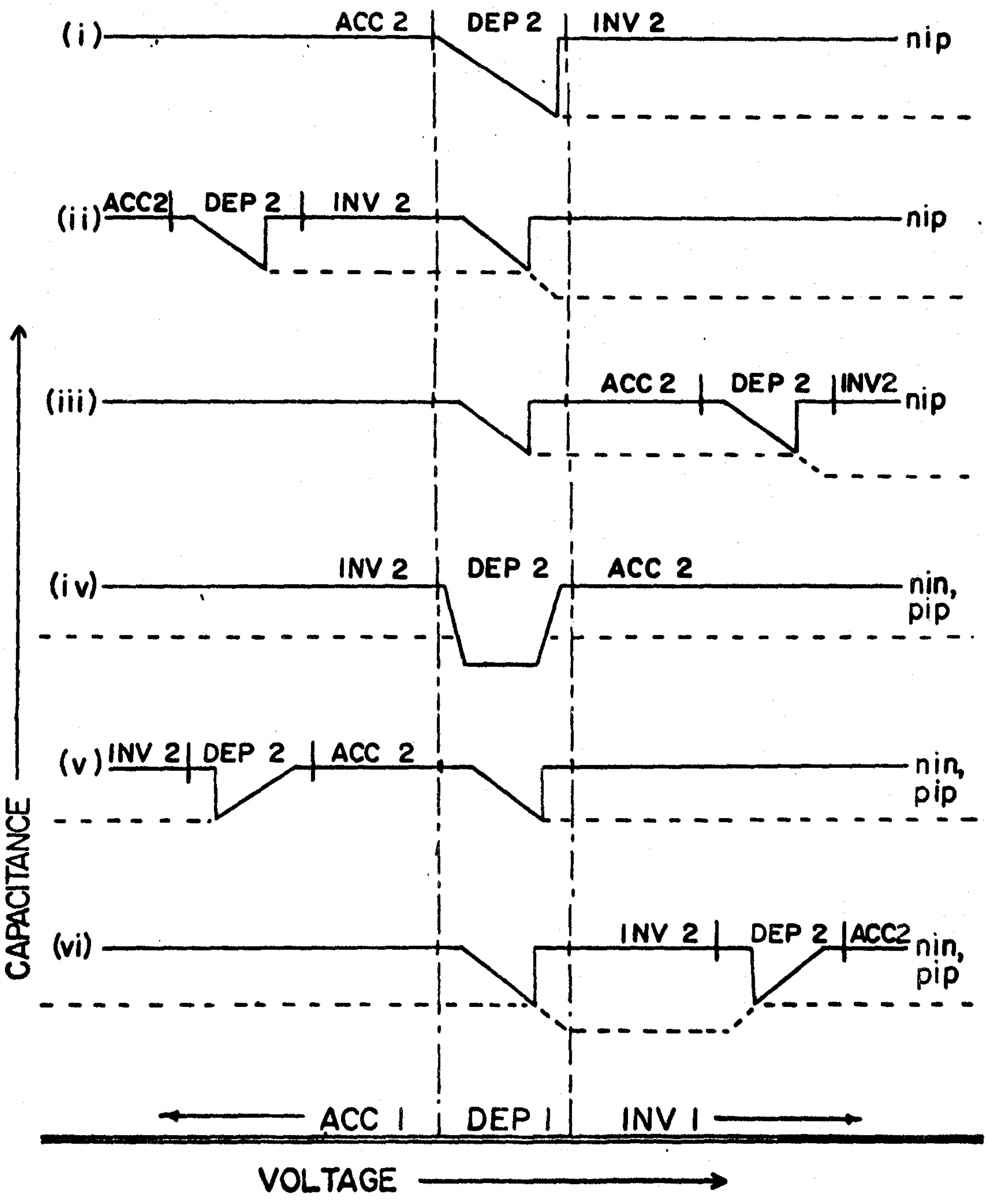

Figure 23

imaginary parts of the semiconductor admittances, Y_1 and Y_2, gives

$$G_{dev} = \frac{\omega^4(C_{ox}^2 G_{S2} C_{S1}^2 + C_{ox}^2 G_{S1} C_{S2}^2) + \omega^2(C_{ox}^2 G_{S1}^2 G_{S2} + C_{ox}^2 G_{S2}^2 G_{S1})}{\omega^2(C_{ox}^2 G_{S1}^2 + C_{ox}^2 G_{S2}^2 + C_{S2}^2 G_{S1}^2 + C_{S1}^2 G_{S2}^2 + 2C_{ox}^2 G_{S1} G_{S2} + 2C_{ox} C_{S1} G_{S2}^2 + 2C_{ox} C_{S2} G_{S1}^2) + G_{S1}^2 G_{S2}^2 + \omega^4(C_{S1}C_{S2} + C_{S1}C_{ox} + C_{S2}C_{ox})^2} \qquad (27)$$

A general analysis of equation 27 is virtually impossible and will not be attempted. However, in most cases, one or more simplifying assumptions can be made to reduce it. Before deriving these expressions, it is useful to discuss the behaviour of the semiconductor admittance (Y_{S1} or Y_{S2}) alone. For this reason figs. 24 and 25 are included to show the individual semiconductor admittances together with the resultant device admittance. In fig. 24 semiconductor 1 is n-type (doped at 10^{15}/cc) while semiconductor 2 is p-type (also doped at 10^{15}/cc). In fig. 25 both semiconductors are p-type (doped at 10^{15}/cc).

The C-V and G-V curves of figs. 24(a) and (b) depict a typical semiconductor admittance*. These curves possess most of the MIS response characteristics(3) with one or two notable exceptions. These are: 1. In the semiconductor C-V curves, the accumulation capacitance and the low frequency inversion capacitance no longer assymptotically approach C_{ox} but increase rapidly, reflecting the

---

*Note that this is the admittance between interface node, 'K_{i_s}', and contace node, 'C' of fig. 7(a).

Figure 24 Ideal, Individual Semiconductor C-V and G-V Response with the Resultant SIS Device C-V and G-V Response (n-i-p case). ω = radian frequency. ∘ represents the flat band condition. G is in units of mho m^2.

(a,b) The C-V and G-V response of semiconductor "1", (n-type, 10^{15}/cc).

(c,d) The C-V and G-V response of semiconductor "2", (p-type, 10^{15}/cc).

(e,f) The device C-V and G-V response obtained by the series admittance of semiconductor "1", the oxide, and semiconductor "2".

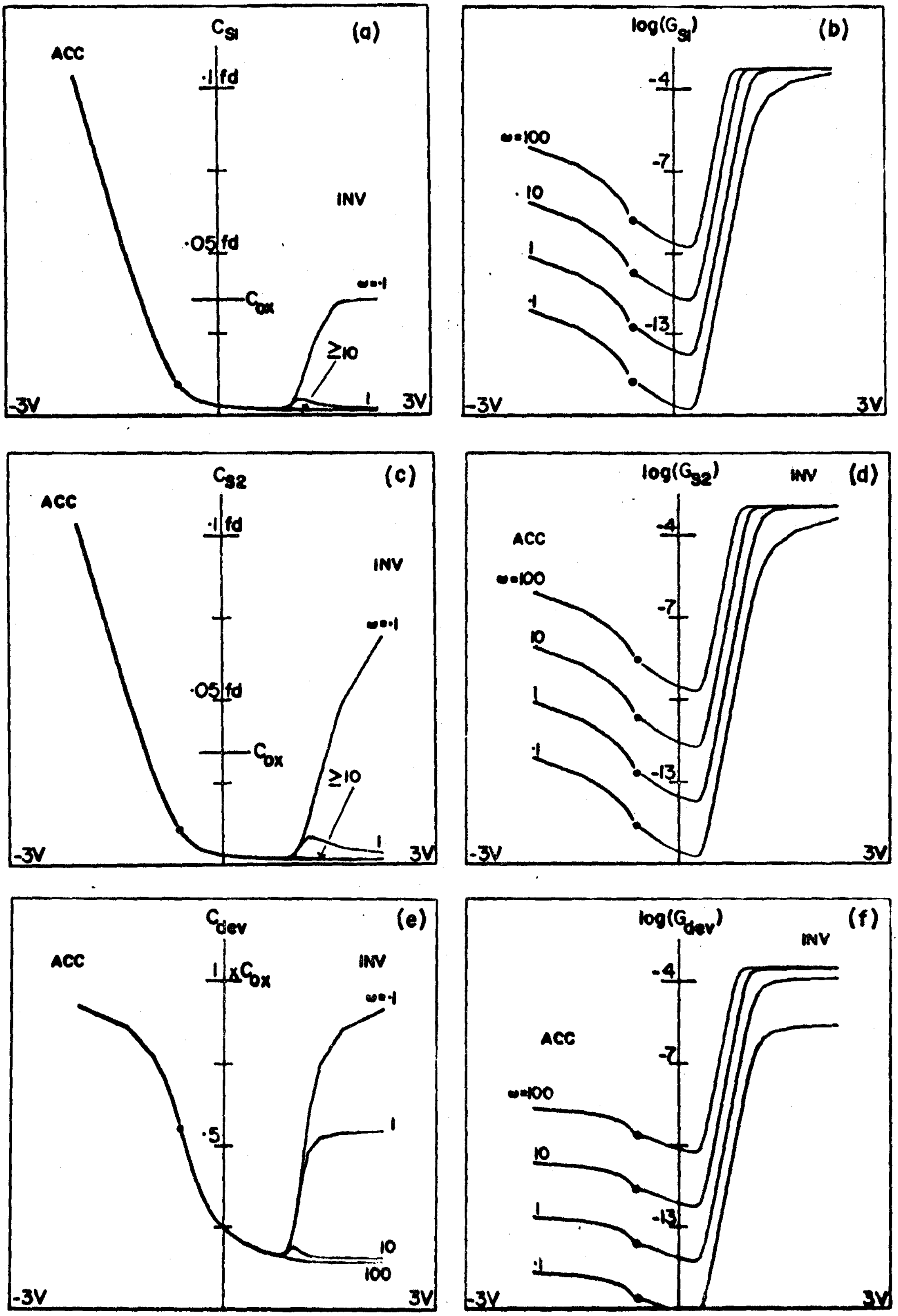
(a)
C_{S1}
ACC
·1 fd
INV
·05 fd
C_{ox}
ω=·1
≥10
1
-3V
3V
(b)
$\log(G_{S1})$
-4
ω=100
-7
10
1
-13
·1
-3V
3V
(c)
C_{S2}
ACC
·1 fd
INV
ω=·1
·05 fd
C_{ox}
≥10
1
-3V
3V
(d)
$\log(G_{S2})$
INV
-4
ACC
ω=100
-7
10
1
-13
·1
-3V
3V
(e)
C_{dev}
ACC
1 x C_{ox}
INV
ω=·1
·5
1
10
100
-3V
3V
(f)
$\log(G_{dev})$
INV
-4
ACC
-7
ω=100
10
1
-13
·1
-3V
3V

Figure 24

Figure 25 Ideal, Individual Semiconductor C-V and G-V Response with the Resultant SIS Device C-V and G-V Response (p-i-p case). ω = radian frequency. ∘ represents flat band condition. G is in units of mho m^2.

(a,b) The C-V and G-V response of semiconductor "1", (p-type, 10^{15}/cc).

(c,d) The C-V and G-V response of semiconductor "2", (p-type, 10^{15}/cc).

(e,f) The device C-V and G-V response obtained by the series admittance of semiconductor "1", the oxide, and semiconductor "2".

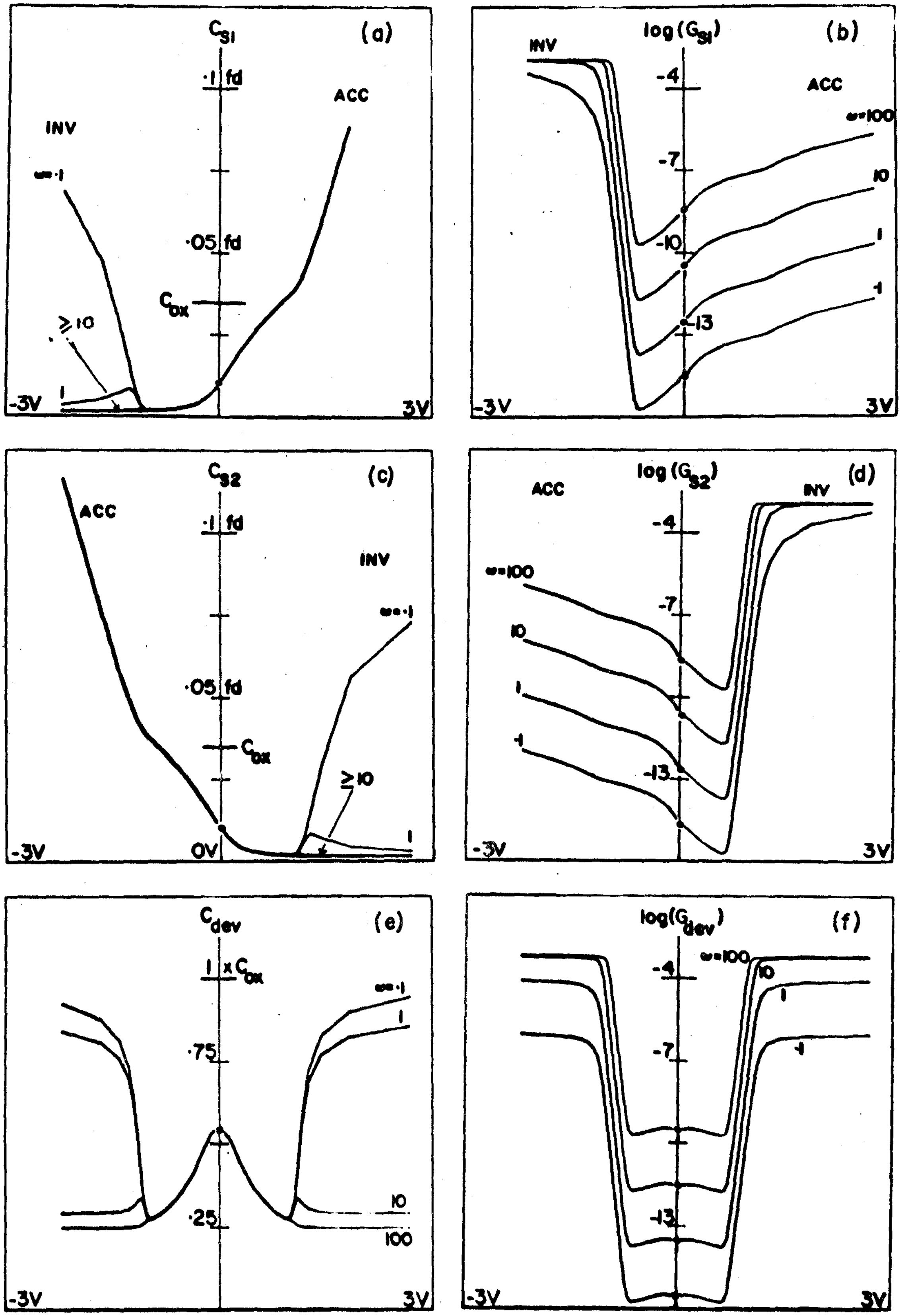
C_{S1}
(a)
·1 fd
ACC
INV
ω=·1
·05 fd
C_{ox}
≥10
1
-3V
3V
log(G_{S1})
(b)
INV
-4
ACC
ω=100
-7
10
-10
1
-13
·1
-3V
3V
C_{S2}
(c)
·1 fd
ACC
INV
ω=·1
·05 fd
C_{ox}
≥10
1
-3V
0V
log(G_{S2})
(d)
ACC
INV
-4
ω=100
-7
10
1
·1
-13
-3V
3V
C_{dev}
(e)
1 x C_{ox}
ω=·1
1
·75
10
·25
100
-3V
3V
log(G_{dev})
(f)
ω=100
-4
10
1
-7
·1
-13
-3V
3V

Figure 25

growing ratio of interface charge density to interface electric field. 2. In the semiconductor G-V curves, there is no saturation in voltage of the accumulation-side conductance*, G_S^{acc}. By making the interface more accumulated, better coupling occurs between the interface displacement current and the semiconductor band currents with a corresponding increase in semiconductor conductance.

MIS C-V features such as the depletion well and the minority carrier response cutoff in inversion can still be seen. Similarly, MIS G-V features such as the inversion conductance saturation at $G_{inv}^V(\omega)$ (where superscript V denotes a saturation in voltage) and the saturation in frequency of $G_{inv}^V(\omega)$ at a level given by G_{inv}^ω (where superscript ω denotes a saturation in frequency) are still evident(3).

The net device conductances of figs. 24(f) and 25(f) can be obtained at any voltage by using semiconductor capacitances, C_{S1} and C_{S2}, and semiconductor conductances, G_{S1} and G_{S2}, (from figs. 24(a - d) and figs. 25 (a - d). With these quantities, and knowing C_{ox}, equation (27) can be evaluated. Because this equation is so unwieldy, several simpler expressions will be derived under various conditions. These various approximations, which are indicated below, have only been derived for the purpose of discussion.

---

*'inv', 'acc', and 'dep' denote inversion, accumulation and depletion. Subscript 'S' denotes semiconductor and 'ox', the oxide.

The C-V and G-V curves presented in this work have been calculated with the exact expression (ie. equation (26) or (27)) using a computer.

The most important simplification is that which can be made for frequencies and bias regions when the semiconductor capacitive admittances (reactances), ωC_{S1} and ωC_{S2}, are much larger than their respective conductances, G_{S1} and G_{S2}. Device conductance, G_{dev}, is then given approximately by

$$G_{dev} \doteq \frac{C_{ox}(G_{S1}C_{S2} + G_{S2}C_{S1})}{C_{ox}C_{S1} + C_{ox}C_{S2} + C_{S1}C_{S2}} \tag{28}$$

Table 5 lists $G_{S1}/\omega C_{S1}$ and $G_{S2}/\omega C_{S2}$ for two voltages and the frequencies in figs. 24 and 25. From this table it can be seen that equation (28) is valid over the entire voltage range at each of the frequencies used. Further approximations can be made at high and low frequencies* for various voltage ranges. These are listed as follows:

---

*Chapter III defines an operational method for dividing the high and low frequency ranges as that frequency 'ω_{inv}' for which $G_{inv}^{V}(\omega)/\omega$ is maximized(3). (Physically, this corresponds closely to the cutoff frequency for interface minority carrier response). In this thesis ω_1^{inv} and ω_2^{inv} will be defined more precisely as that frequency at which the phase angle between the a.c. voltage at the interface and the a.c. minority band current at the interface is 45°. Subscripts 1 and 2 refer to interface 1 and 2. (This is in fact the 'exact' cutoff frequency of the interface minority carrier response).

Table 5

Ratio of Conductance to Reactance (G/ωC) for Semiconductor Admittances YS1 and YS2 and for Device Admittance Y_{dev} (Values are taken from Figure 25 at ± 2 Volts)

Radian Frequency ω	$G_{S1}/\omega C_{S1}$ (S1 is n-type, 10^{15}/cc) + 2 Volts (inversion)	$G_{S1}/\omega C_{S1}$ (S1 is n-type, 10^{15}/cc) - 2 Volts (accumulation)	$G_{S2}/\omega C_{S2}$ (S2 is p-type, 10^{15}/cc) + 2 Volts (inversion)	$G_{S2}/\omega C_{S2}$ (S2 is p-type, 10^{15}/cc) - 2 Volts (accumulation)	$G_{dev}/\omega C_{dev}$ + 2 Volts (double inversion)	$G_{dev}/\omega C_{dev}$ - 2 Volts (double accumulation)
.1	7.25×10^{-3}	5.68×10^{-12}	3.98×10^{-3}	7.11×10^{-12}	7.36×10^{-2}	6.31×10^{-11}
1.0	2.51×10^{-2}	5.68×10^{-11}	2.51×10^{-2}	7.11×10^{-11}	6.03×10^{-1}	6.31×10^{-10}
10.0	3.31×10^{-3}	5.68×10^{-10}	6.61×10^{-3}	7.11×10^{-10}	4.88×10^{-1}	6.31×10^{-9}
100.0	3.31×10^{-4}	5.68×10^{-9}	6.61×10^{-4}	7.11×10^{-9}	5.26×10^{-2}	6.31×10^{-8}

(i) double inversion at high frequencies where $C_S^{inv} << C_{ox}$

$$G_{dev} \simeq (G_{S1}^{inv}C_{S2}^{inv} + G_{S2}^{inv}C_{S1}^{inv})/(C_{S1}^{inv} + C_{S2}^{inv}) \tag{29a}$$

and at low frequencies where $C_S^{inv} >> C_{ox}$

$$G_{dev} \simeq C_{ox}(G_{S1}^{inv}/C_{S1}^{inv} + G_{S2}^{inv}/C_{S2}^{inv}) \tag{29b}$$

(ii) double accumulation where $C_S^{acc} >> C_{ox}$

$$G_{dev} \simeq C_{ox}(G_{S1}^{acc}/C_{S1}^{acc} + G_{S2}^{acc}/C_{S2}^{acc}) \tag{30}$$

(iii) Semiconductor 1 in accumulation; Semiconductor 2 in inversion; at high frequencies where $C_{S2}^{inv} << C_{ox}$

$$G_{dev} \simeq G_{S2}^{inv} \tag{31a}$$

and at low frequencies where $G_{S1}^{acc} << G_{S2}^{inv}$, with $C_{S1}^{acc} >> C_{ox}$ and $C_{S2}^{inv} >> C_{ox}$

$$G_{dev} \simeq C_{ox}\, G_{S2}^{inv}/C_{S2}^{inv} \tag{31b}$$

The second most important simplification in analyzing the SIS conductance is that which can be made when only one of the semiconductor conductances is negligible. For example, with $G_{S1} << \omega C_{S1}$ but with G_{S2} not negligible with respect to ωC_{S2}, the SIS structure can be analyzed (at least in terms of conductance-voltage behaviour) as an MIS structure with the oxide capacitance C_{ox} replaced by the voltage and frequency dependent series combination of C_{S1} and C_{ox}. Defining C'_{ox} as below

$$C'_{ox} = C_{ox}C_{S1}/(C_{S1} + C_{ox}) \tag{32}$$

equation (27) reduces to

$$G_{dev} \simeq \omega^2 \, C'^2_{ox} \, G_{S2}/(G^2_{S2} + \omega^2(C'_{ox} + C_{S2})^2) \tag{33}$$

6. Ideal SIS Response as a Function of Dopant Impurity Concentration

(a) n-i-p Structure

Figure 26 shows C-V and G-V curves for 3 n-i-p diodes. In each diode the p-type semiconductor doping was fixed at 10^{15}/cc while the n-type dopant density was varied (10^{11}/cc, 10^{13}/cc, and 10^{15}/cc). The C-V curves of fig. 26(a) show a response similar to case (i) in fig. 23. Note that with different dopant densities two depletion wells can be seen as in both figs. 26(c) and (e).

The G-V curves in figs. 26(b), (d) and (f) go from double

Figure 26 The Effect of Doping Density on the Ideal SIS Admittance (n-i-p case) ω is radian frequency. ∘ denotes the flat band condition. G is in units of mho m^2.

(a,b) Semiconductor "1" n-type, 10^{15}/cc; Semiconductor "2" p-type, 10^{15}/cc.

(c,d) Semiconductor "1" n-type, 10^{13}/cc; Semiconductor "2" p-type, 10^{15}/cc.

(e,f) Semiconductor "1" n-type, 10^{11}/cc; Semiconductor "2" p-type, 10^{15}/cc.

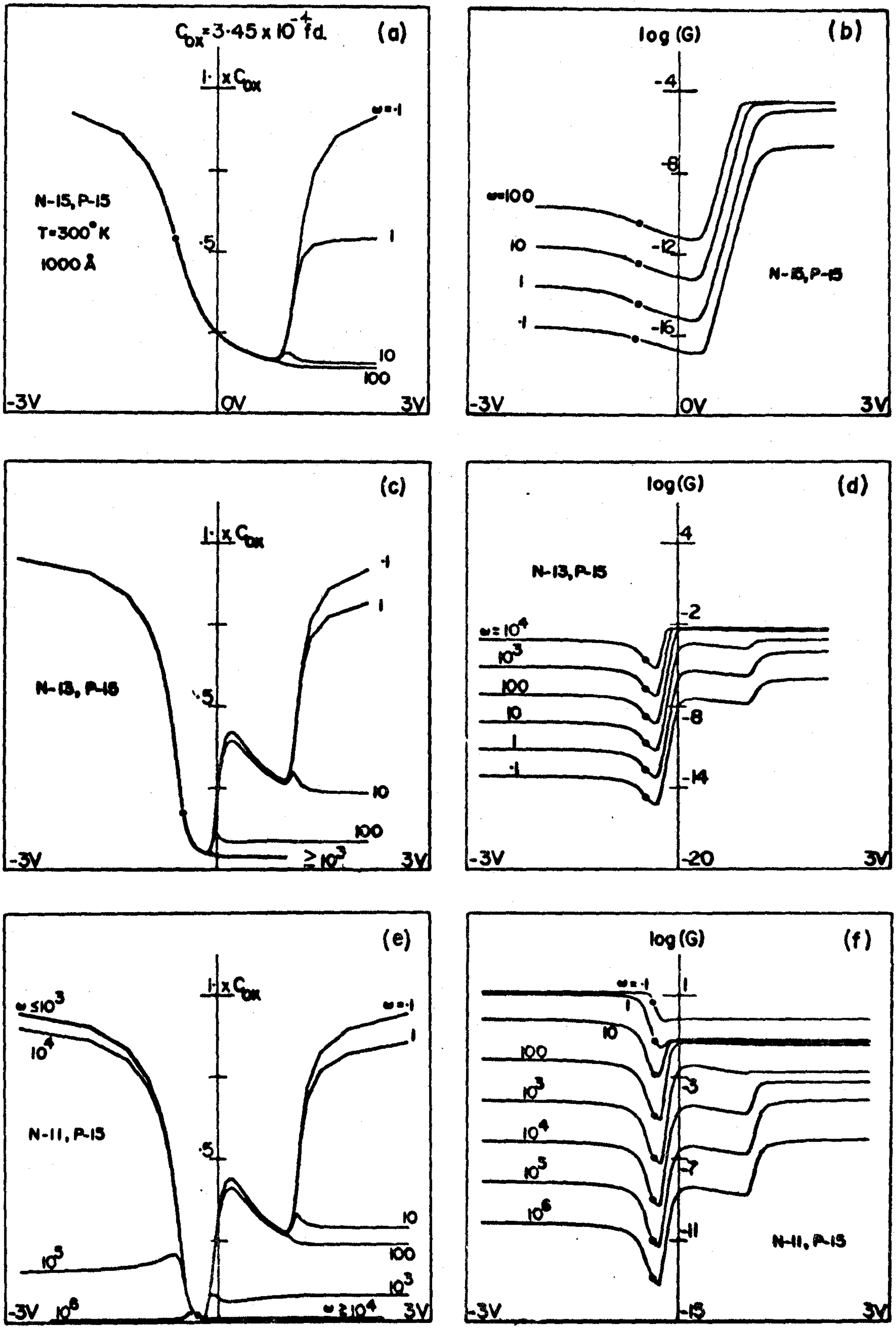
(a)
C_OX=3·45 x 10^-4 fd.
1·x C_OX
ω=·1
1
10
100
·5
N-15, P-15
T=300°K
1000 Å
-3V
0V
3V
(b)
log (G)
-4
-8
-12
-16
ω=100
10
1
·1
N-15, P-15
-3V
0V
3V
(c)
1·x C_OX
·1
1
·5
10
100
≥10^3
N-13, P-15
-3V
3V
(d)
log(G)
4
-2
-8
-14
-20
N-13, P-15
ω=10^4
10^3
100
10
1
·1
-3V
3V
(e)
1·x C_OX
ω≤10^3
10^4
ω=·1
1
·5
N-11, P-15
10
100
10^5
10^3
-3V
10^6
ω≥10^4
3V
(f)
log (G)
ω=·1
1
10
100
10^3
10^4
10^5
10^6
1
-3
-7
-11
-15
N-11, P-15
-3V
3V

Figure 26

accumulation for negative biases to double inversion for positive biases. At all frequencies the combined response can be analyzed under the approximation discussed in Section 5, where the semiconductor conductances are negligible with respect to the semiconductor reactances, ie., $G_{S1} << \omega C_{S1}$ and $G_{S2} << \omega C_{S2}$.

In regions of double accumulation the device conductance is, therefore, given approximately by equation (30). The semiconductor capacitances, C_{S1} and C_{S2}, at large band bending reflect the total charge densities at the respective interfaces and as such are relatively independent of the doping density. The semiconductor conductances, G_{S1} and G_{S2}, reflect bulk ohmic losses resulting from finite majority carrier resistivity and hence decrease with increased doping density. From equation (30) the net device conductance, G_{dev}, is proportional to $(G_{S1}^{acc}/C_{S1}^{acc} + G_{S2}^{acc}/C_{S2}^{acc})$ and, therefore, must also decrease with increased doping density.

In regions of double inversion and for frequencies greater than the minority carrier cutoff frequencies, ω_1^{inv} and ω_2^{inv}, equation 29a can be applied. Above ω^{inv}, G_{S1}^{inv} increases with decreasing doping density(3) while C_{S1}^{inv} decreases (G_{S2}^{inv} and G_{S2}^{inv} remain unchanged because the 'S2' doping density is constant). Hence the numerator of equation (29a) behaves like $G_{S1}^{inv}\ C_{S2}^{inv}$. The slight conductance drop between zero and one volt in figs. 26(d) and (f) results from the fall of C_{S2} as semiconductor 2 goes through depletion (see figs. 26(c) and (e)).

The sharp rise in the low frequency conductance at about one volt marks the point at which semiconductor 2 reaches inversion. At low frequencies, C_{S2} does not saturate but increases rapidly. Furthermore, for low frequencies, G_{S1}^{inv} increases with decreased doping density$^{(2)}$ so that this voltage also marks the point at which $G_{S2}^{inv}C_{S1}^{inv}$ (negligible at high frequency) begins to contribute to the device conductance.

(b) p-i-p Structure

Figure 27 shows C-V and G-V curves for 3 p-i-p diodes. In each case the dopant density of "semiconductor 2" was fixed at 10^{15}/cc while that of "semiconductor 1" was varied (10^{11}/cc, 10^{13}/cc and 10^{15}/cc). The C-V curves of figs. 27(a) and (c) show a response similar to that of case (iv) in fig. 23. Note the capacitance maximum (between the depletion minima) where both semiconductors are partially accumulated. As predicted$^{(1)}$, the center maximum remains at high frequency, resulting in an unusual bell shaped response.

As with fig. 26, the G-V curves can be analyzed under the approximation that $G_{S1} << \omega C_{S1}$ and $G_{S2} << \omega C_{S2}$. At low frequencies the device conductance for large positive or negative bias is given by equation 32(b). Thus the device conductance, G_{dev}, reflects the low frequency variation with doping densities of G_S^{inv}/C_S^{inv} (decreasing with decreased doping density). At high

Figure 27 The Effect of Doping Density on the Ideal SIS Admittance (p-i-p case). ω is radian frequency. ∘ denotes the flat band condition. G is in units of mho m^2.

(a,b) Semiconductor "1" p-type, 10^{15}/cc; Semiconductor "2" p-type, 10^{15}/cc.

(c,d) Semiconductor "1" p-type, 10^{13}/cc; Semiconductor "2" p-type, 10^{15}/cc.

(e,f) Semiconductor "1" p-type, 10^{11}/cc; Semiconductor "2" p-type, 10^{15}/cc.

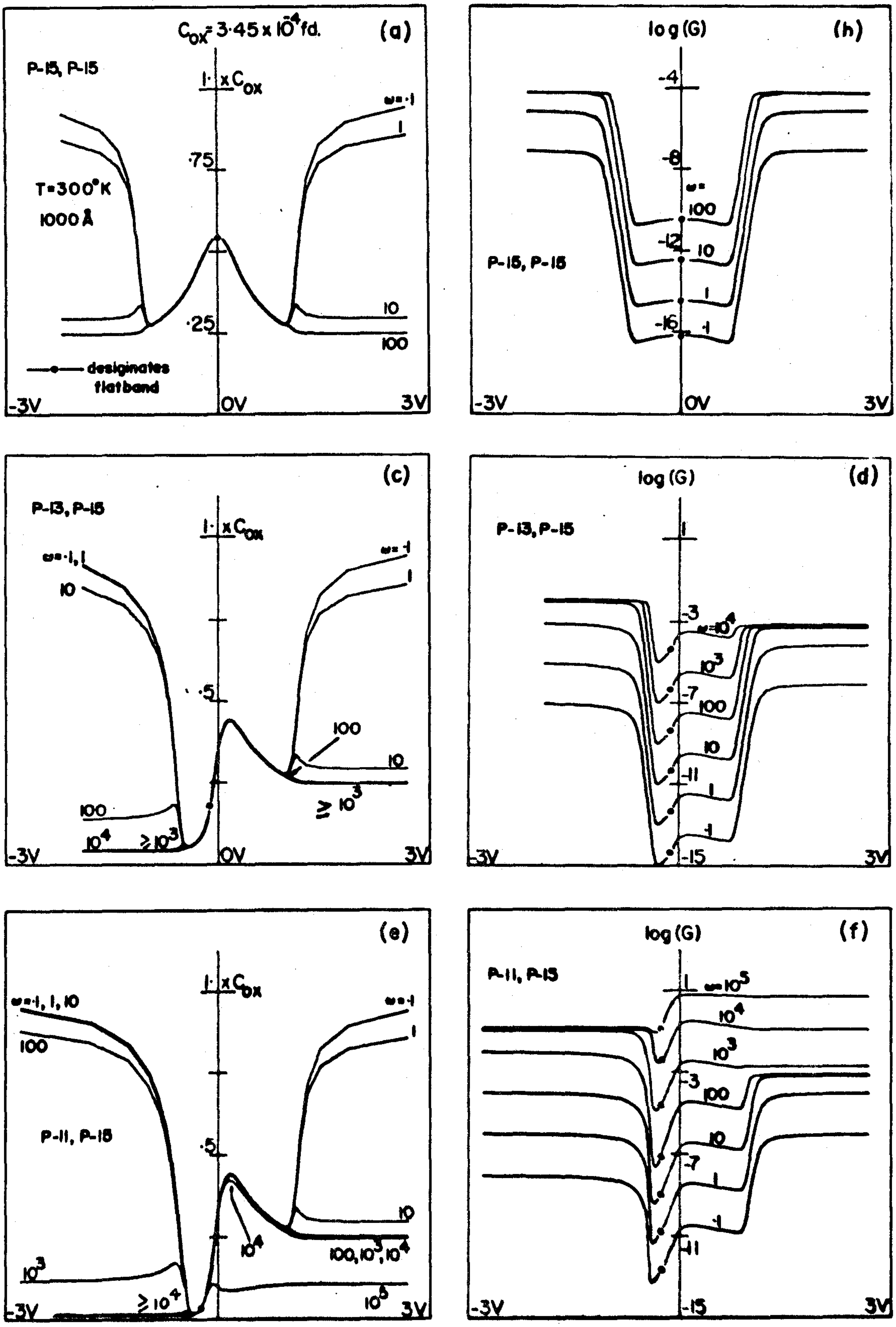
(a)
C_{OX} = 3·45 x 10^{-4} fd.
P-15, P-15
1· x C_{OX}
ω=·1
1
·75
T=300°K
1000Å
10
·25
100
designates flatband
-3V
0V
3V
(h)
log (G)
-4
-8
ω=
100
-12
10
P-15, P-15
1
-16
·1
-3V
0V
3V
(c)
P-13, P-15
1· x C_{OX}
ω=·1, 1
10
ω=·1
1
·5
100
10
100
≥ 10^3
10^4
≥ 10^3
-3V
0V
3V
(d)
log (G)
P-13, P-15
1
-3
ω=10^4
10^3
-7
100
10
-11
1
·1
-3V
-15
3V
(e)
P-11, P-15
1· x C_{OX}
ω=·1, 1, 10
100
ω=·1
1
·5
10
10^4
100, 10^3, 10^4
10^3
≥ 10^4
10^5
-3V
3V
(f)
log (G)
P-11, P-15
1
ω=10^5
10^4
10^3
-3
100
10
-7
1
·1
-11
-3V
-15
3V

Figure 27

frequency and large negative or positive bias, G_{dev} is given simply by the conductance G_S^{inv} of the inverted semiconductor. Thus, at high frequency, G_{dev} increases with decreasing doping density. In the central region of the G-V curves of figs. 33(d) and (f), the conductance is dominated by the term in $G_{S1}^{acc}C_{S2}^{dep}$ since the accumulation conductance of the more lightly doped semiconductor (semiconductor 1) is much greater than that of the more heavily doped semiconductor (semiconductor 2). The slight fall in G_{dev} between zero and one volts is due to the fall in C_{S2}^{dep}. The sharp rise at about one volt marks the point at which semiconductor 2 is becoming inverted. At this point, the conductance quickly becomes that given by equation (31a) at high frequencies or by equation (31b) at low frequencies.

7. Effect of Fixed Charge and Surface States

(a) p-i-p Structure

Figures 28 and 29 show the effects of fixed charge and surface states at each of the oxide-semiconductor interfaces. Figs. 28(a) and (b) give C-V and G-V curves for suppressed* a.c. surface state response in a p-i-p structure where both semiconductors are doped at 10^{15}/cc and have a fixed interface charge of -3.2×10^{-8} coulombs/cm^2 at each interface. Figs. 28(c) and (d) give the corresponding curves for normal surface state response. Figs. 28(e)

---

*Suppressed surface state response is obtained by setting the "surface-state level to band" conductances (G_{PS_i} and G_{NS_i}) shown in fig. 7(c) to zero.

Figure 28 Effect of Surface States and Fixed Interface Charge (p-i-p case, both semiconductors are p-type doped at 10^{15}/cc with Surface State Distribution 1 at each interface. G is in units of mho m^2).

(a,b) C-V and G-V curves with a.c. surface state response suppressed. There is a fixed charge at each interface of -3.2×10^{-8} coulombs/cm^2.

(c,d) C-V and G-V curves with normal surface state response. Fixed charges are identical to those in (a,b).

(e,f) C-V and G-V curves with normal surface state response. There is a fixed charge density at each interface of $+3.2 \times 10^{-8}$ coulombs/cm^2.

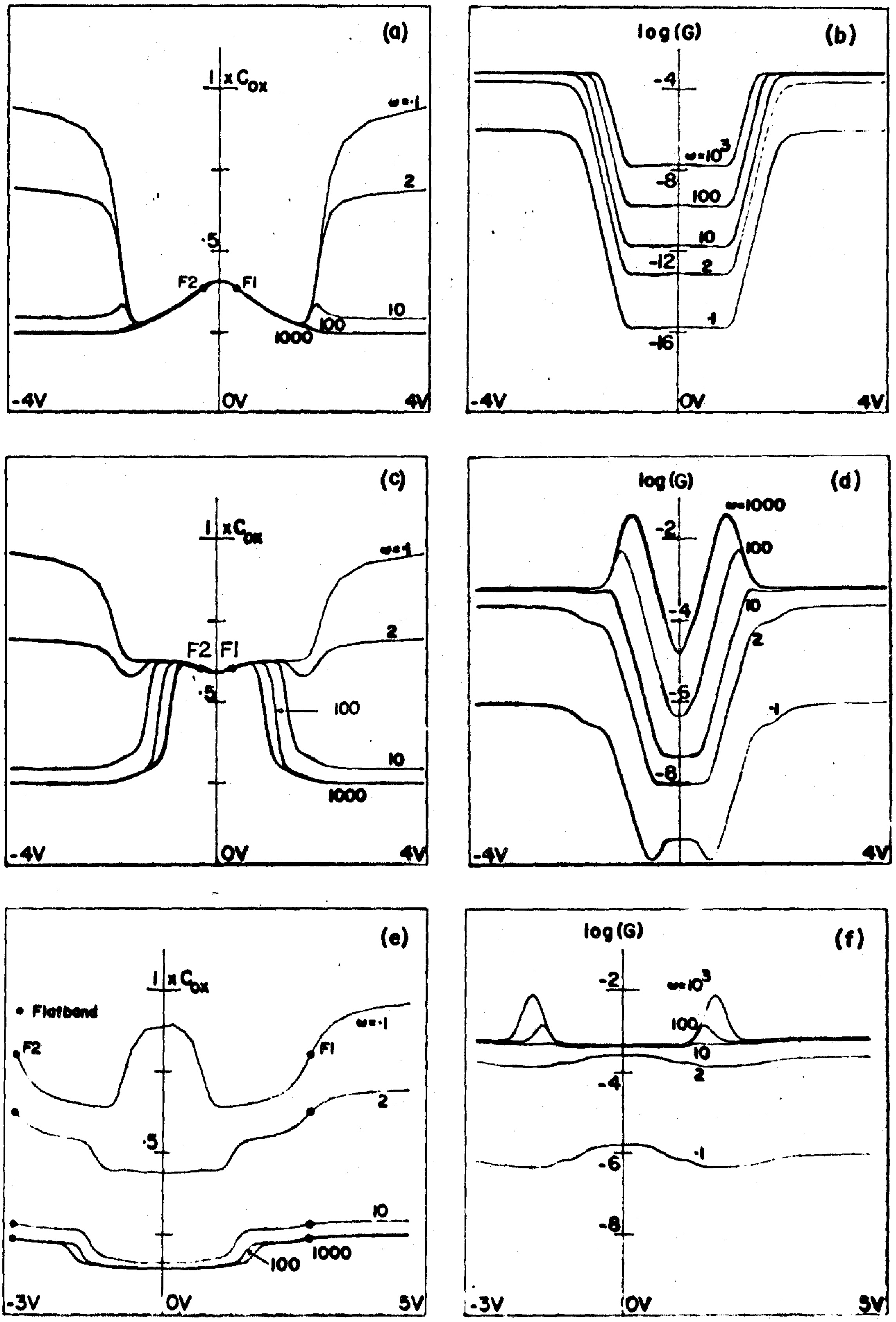
(a)
1 x C_ox
ω=.1
2
.5
F2
F1
10
100
1000
-4V
0V
4V
log (G)
(b)
-4
ω=10^3
-8
100
10
-12
2
.1
-16
-4V
0V
4V
(c)
1 x C_ox
ω=.1
2
F2 F1
.5
100
10
1000
-4V
0V
4V
log (G)
(d)
ω=1000
-2
100
-4
10
2
-6
.1
-8
-4V
0V
4V
(e)
1 x C_ox
• Flatband
F2
F1
ω=.1
2
.5
10
100
1000
-3V
0V
5V
log (G)
(f)
-2
ω=10^3
100
10
2
-4
.1
-6
-8
-3V
0V
5V

Figure 28

and (f) give normal C-V and G-V response for the same p-i-p device as in figs.28(a-d) except that the fixed interface charge densities are now $+3.2 \times 10^{-8}$ coulombs/cm^2. Both interfaces for the SIS device of figs.28(a) to (d) and both interfaces for that of figs. 28(e) and (f) have a surface state profile denotes as "Surface State Distribution 1". This, along with a second surface state distribution, "Surface State Distribution 2", is shown in fig. 13.

Looking at the C-V curves and comparing the behaviour with and without a.c. surface state response (fig. 28(e) versus fig. 28(a)),gives a clear picture of the a.c. effect of surface states. Points on the curves marked F1 and F2 denote the biases at which semiconductor 1 and semiconductor 2 go through the flatband condition. The depletion well on the left is that of semiconductor 1, with the well on the right that of semiconductor 2. The effect of the net interface charge, fixed charge and surface state charge determines the relative positions of the depletion wells (as depicted in case (iv) in fig. 23), with the region between F1 and F2 being slightly accumulated for both semiconductors. The effect of frequency on surface state response can, therefore, be explained in the normal way. Increasing frequency cuts off the response of states furthest from the majority carrier band edge. Response from states near the minority carrier band edge is cut off by the lack of semiconductor minority carrier response.

Fixed interface charge can cause gross changes in C-V response as seen by comparing figs. 28(c) and (e). The depletion well on the left is now that of semiconductor 2 and the region in the center of the curve is a region of double inversion (see case (vi) of fig. 23).

Naturally the G-V curves (figs. 28(d) and (f)) also differ considerably when fixed interface charge is changed. The center dip in fig. 28(d) reflects the lower G_S values associated with accumulation. This feature is missing in fig. 28(f) which has no region of double accumulation. The surface state conductance peaks of both semiconductors are clearly observable in figs. 28(d) and (f). These peaks grow in size and shift in voltage$^{(3)}$ toward the accumulation side of the respective semiconductor with increasing frequency. Hence, in fig. 28(d), the peaks on the left represent a.c. surface state response at the interface of semiconductor 2, while in fig. 28(f) the peaks on the left represent semiconductor 1.

(b) n-i-p Structure

Figure 29 shows the G-V and C-V response for semiconductor 1, n-type (doped at 10^{13}/cc) and semiconductor 2, p-type (doped at 10^{15}/cc). Figs. 29(a) to (d) show both the 'suppressed' and the 'normal' surface state response for the case of a fixed charge of -3.2×10^{-8} coulombs/cm^2 at both insulator-semiconductor interfaces. Figs. 29(e) and (f) show only the normal response but with a fixed charge of $+3.2 \times 10^{-8}$ coulombs/cm^2 at each interface. The surface state distribution for the n-type semiconductor interface

Figure 29 Effect of Surface States and Fixed Interface Charge (n-i-p case. Semiconductor 1 is n-type doped at 10^{13}/cc with Surface State Distribution 1 at its interface, while semiconductor 2 is p-type, doped at 10^{15}/cc with Surface State Distribution 2 at its interface. G is in units of mho m^2).

(a,b) C-V and G-V curves with a.c. surface state response arbitrarily suppressed. There is a fixed charge at both interfaces of -3.2×10^{-8} coulombs/cm^2.

(c,d) C-V and G-V curves with normal surface state response. Fixed charges are identical to those in (a,b).

(e,f) C-V and G-V curves with normal surface state response. There is a fixed charge density at each interface of $+3.2 \times 10^{-8}$ coulombs/cm^2.

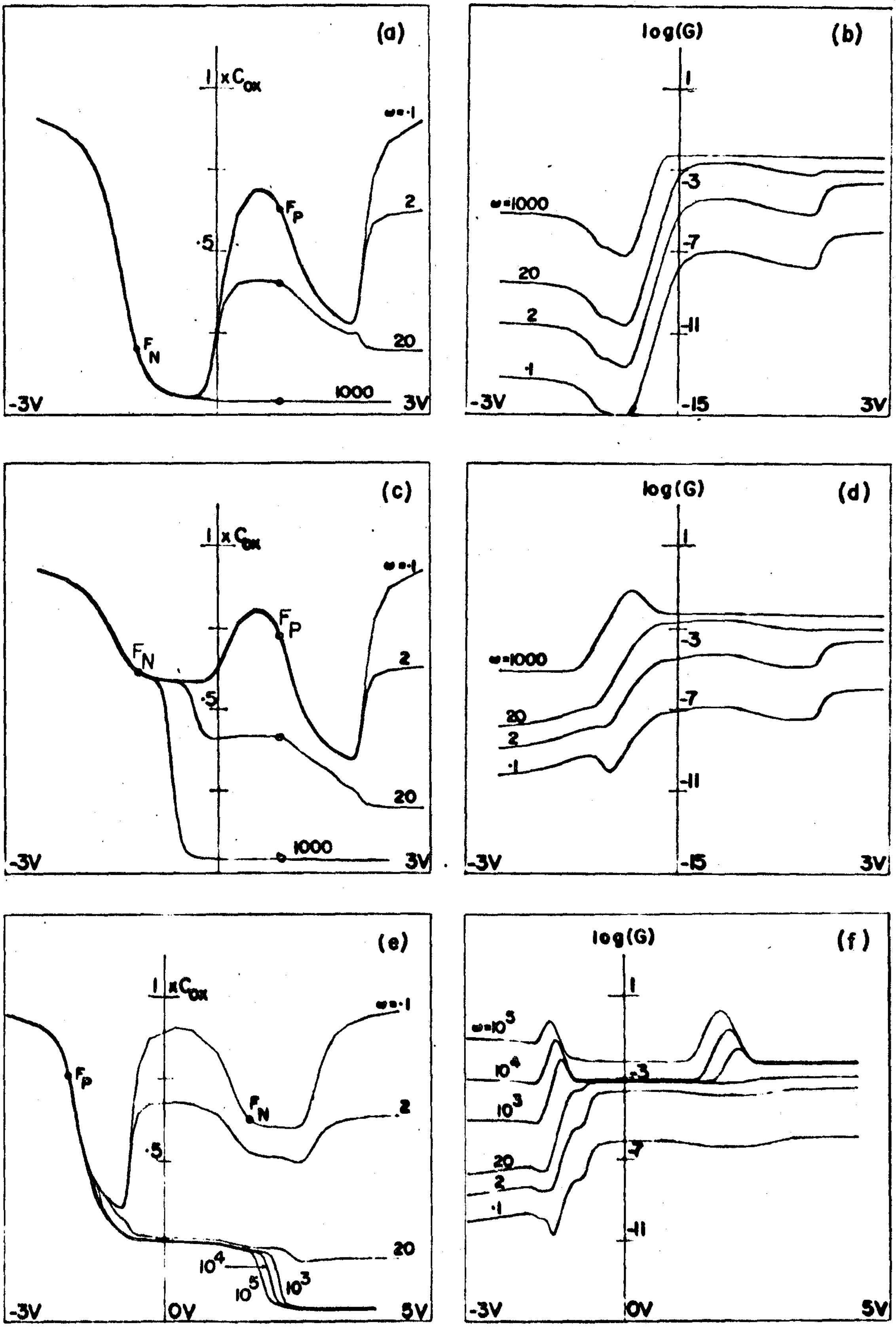
(a)
1 x C_ox
ω=·1
2
20
1000
F_P
F_N
·5
-3V
3V
(b)
log(G)
1
-3
-7
-11
-15
ω=1000
20
2
·1
-3V
3V
(c)
1 x C_ox
ω=·1
2
20
1000
F_P
F_N
·5
-3V
3V
(d)
log(G)
1
-3
-7
-11
-15
ω=1000
20
2
·1
-3V
3V
(e)
1 x C_ox
ω=·1
2
20
F_P
F_N
·5
10^4
10^5
10^3
-3V
0V
5V
(f)
log(G)
1
-3
-7
-11
ω=10^5
10^4
10^3
20
2
·1
-3V
0V
5V

Figure 29

is Surface State Distribution 1 as in fig. 13 and for the p-type semiconductor interface is Surface State Distribution 2. Surface State Distribution 2 differs from Distribution 1 by having a density 10 times greater across the middle of the bandgap.

The low frequency a.c. response of these midgap surface states is evidently enough to fill in the depletion well capacitance of the less doped n-type semiconductor to such an extent that it is shallower than the depletion well of the more heavily doped p-type semiconductor (fig. 29(c)). At high frequencies only states near the respective majority band edges are contributing to the C-V (and G-V) response. Thus the high frequency C-V curve for the case of 'normal' surface state response ($\omega = 1000$, fig. 29(c)) approaches that of the 'suppressed' response ($\omega = 1000$, fig. 29(a)).

Figures 29(c) and (d) can be compared with figs. 29(e) and (f) to illustrate the effect on the C-V and G-V characteristics of changing the sign of the fixed interface charge. In figs. 29(c) and (d) the 'n' depletion well is on the left and corresponds to case (iii) as shown in fig. 23. In figs. 29(e) and (f) the 'n' depletion well is on the right and corresponds to case (ii) as shown in fig. 23.

Perhaps the most striking effect in fig. 29 is not in the change in the C-V response but in the G-V response. In fig. 29(d) there is only one surface state peak, while in fig. 29(f) two surface state peaks can be seen. This can be explained by looking at

G_{dev} as given by equation (28) and noting that the semiconductor conductances are multiplied by the capacitance of the semiconductor on the other side (ie., $G_{S1}C_{S2}$ and $G_{S2}C_{S1}$). Because of the difference in doping density, $G_N^{inv} > G_P^{inv}$ and $C_P^{inv} > C_N^{inv}$ (where subscripts 'N' and 'P' refer to the n-type and p-type semiconductors respectively). Hence in fig. 29(d) the missing surface state conductance peak near F_p (associated with the surface states near the p-type majority carrier band) is explained by noting that $G_P^{acc}C_N^{inv}$ is negligible (at least at the frequencies used) with respect to $G_N^{acc}C_P^{inv}$.

8. SRH Centre Effects

SRH (Shockley-Read-Hall) centers(22,23) affect the semiconductor response through charge storage (capacitive) effects and through alteration of the coupling between majority band and minority band a.c. currents. In the a.c. transmission line model, each SRH trap level(21) requires trap to band conductances G_{RP} and G_{RN} with capacitive coupling C_R between the displacement node, K, and the trap level node, R. Equations for these quantities are given in Appendix 2.

Figure 30 shows typical C-V and G-V curves for a p-i-p structure with Surface State Distribution 1 and a fixed charge density of -3.2×10^{-8} coulombs/cm^2 at each insulator-semiconductor interface. Figs. 30(a) and (b) show C-V and G-V curves for

Figure 30 Effect of SRH Centres and SRH Centre Capture Cross Sections. (Both semiconductors are p-type, doped at 10^{15}/cc. With a mid-gap SRH density of 10^{13}/cc. Both have Surface State Distribution 1 and a fixed charge density of -3.2×10^{-8} coulombs/cm^2 at each insulator-semiconductor interface. G is in units of mho m^2).

(a,b) C-V and G-V curves for supressed a.c. surface state response. The capture cross section times thermal velocity ($\sigma\theta$) parameter is assumed to be 5×10^{-13} m^3/sec for both holes and electrons.

(c,d) C-V and G-V curves for normal a.c. surface state response. SRH centre data is identical to that given for (a,b).

(e) C-V curve for noraml a.c. surface state response. The capture cross section times thermal velocity parameter has been reduced by a factor of 50 to 1×10^{-14} m^3/sec for both holes and electrons.

(f,g) G-V response for suppressed and normal surface state response. SRH centre data is identical to that given for (e).

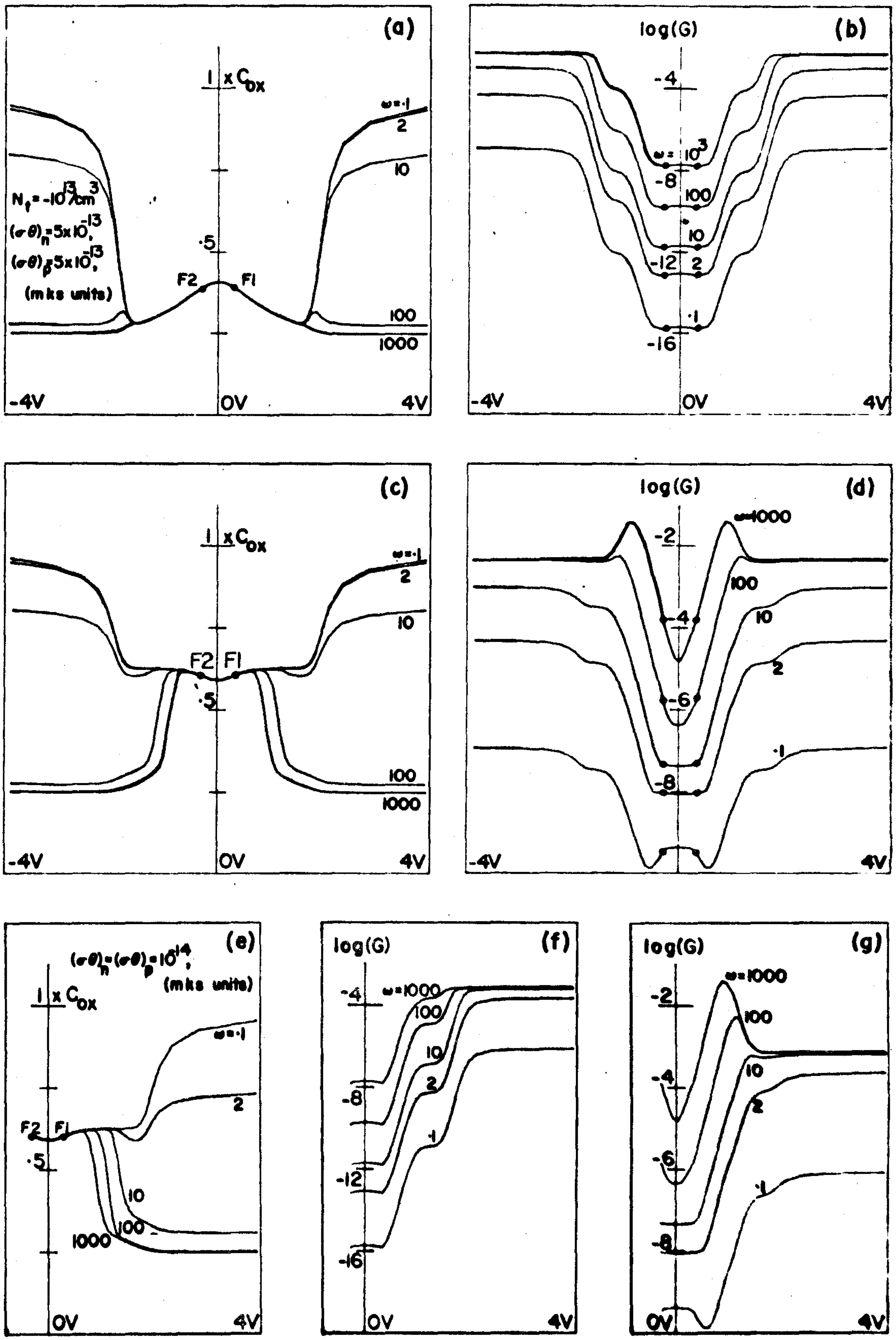
(a)
1 x C_ox
ω=1
2
10
$N_t = -10^{13}/\text{cm}^3$
$(\sigma\theta)_n = 5\times10^{-13}$,
$(\sigma\theta)_p = 5\times10^{-13}$,
(mks units)
·5
F2
F1
100
1000
-4V
0V
4V
(b)
log(G)
-4
ω = 10^3
-8
100
10
-12
2
·1
-16
-4V
0V
4V
(c)
1 x C_ox
ω=1
2
10
F2
F1
·5
100
1000
-4V
0V
4V
(d)
log(G)
ω=1000
-2
100
-4
10
-6
2
·1
-8
-4V
4V
(e)
$(\sigma\theta)_n = (\sigma\theta)_p = 10^{-14}$,
(mks units)
1 x C_ox
ω=1
2
F2
F1
·5
10
100
1000
0V
4V
(f)
log(G)
-4
ω=1000
100
10
2
·1
-8
-12
-16
0V
4V
(g)
log(G)
ω=1000
-2
100
-4
10
2
-6
·1
-8
0V
4V

Figure 30

'suppressed' surface state response while figs. 30(c) and (d) show curves for 'normal' surface state response. The SRH trap density was 10^{13}/cc in both semiconductors and the SRH energy level was exactly at midgap. The SRH center was also characterized in terms of a capture cross section for holes and electrons, σ_{Rn} and σ_{Rp}. These quantities always enter the expressions for the trap to band conductances (G_{PR} and G_{NR} shown in fig. 7(b) and given in Appendix 2) in conjunction with the carrier velocities, θ_p and θ_n. Hence the products $(\sigma\theta)_n$ and $(\sigma\theta)_p$ are given in the figures (ie., in figs. 30(a) to (d) as 5×10^{-13} m^3/sec for both holes and electrons in both semiconductors).

Figures 30(e), (f) and (g) give C-V and G-V curves for the same p-i-p device as in figs. 30(a) to (d) with the exception that the $(\sigma\theta)$ product has been changed to 1×10^{-14} m^3/sec. For $(\sigma\theta)$ products this low, the effect of the SRH centre (10^{13}/cc) on the C-V and G-V response is negligible. This can be seen by comparing the C-V and G-V curves of figs. 30(e) and (g) with the C-V and G-V curves for the SRH free system of figs. 28(c) and (d). With the higher value of $(\sigma\theta)$ (ie., 5×10^{-13} m^3/sec) in figs. 30(a) to (d), the expected(3) effects can be seen. That is, better inversion layer response (resulting in inversion layer capacitance response to higher frequencies), an increase in the 'background' inversion conductance at high frequencies (above ω_{inv}) and a decrease in the background inversion conductance at low frequencies.

9. Effect of Light

It has been shown(3) that the a.c. transmission line model of the semiconductor can be solved exactly even in non-equilibrium situations provided an exact d.c. solution can be obtained. Active elements must be added to the transmission line as shown in fig. 7(d). The case treated here is that of hole-electron pair creation through SRH centers when the semiconductor is illuminated with light. The d.c. solution used assumes that the same quasi Fermi shift appropriate in the bulk semiconductor can be applied throughout the space charge region(24).

Typical C-V and G-V curves for both 'suppressed' and 'normal' surface state response are shown in figs. 31(a) to (d). The p-i-p diode is exactly identical to that of figs. 30(e) to (g). The minority band quasi Fermi level shift of .2 eV provides increased minority carrier response. The double depletion well is narrowed in both the C-V and G-V curves and the surface state conductance bumps almost merge at $\omega = 10^6$ rad/sec in fig. 31(d). The C-V curves show inversion minority carrier response up to more than $\omega = 100$. As in the MIS case(3), background inversion conductance is less at low frequencies (below ω_{inv}) and greater at high frequencies (above ω_{inv}) than the corresponding SIS case with no light illumination.

10. Response as a Function of Temperature

Figure 32 shows C-V curves for normal surface response at

Figure 31 Effect of SRH Centre, Light Stimulated Hole-Electron Pair Creation (Both semiconductors are p-type doped at 10^{15}/cc. Both have a mid-gap SRH centre density of 10^{13}/cc with $(\sigma\theta)_n = (\sigma\theta)_p = 10^{-14}$ m^3/sec. Both semiconductors have a d.c. quasi Fermi level shift of .2 eV which corresponds to a bulk pair production rate of 2.35 x 10^{23} pairs/m^3/sec. Both semiconductors have Surface State Distribution 1 as well as a fixed charge density of -3.2 x 10^{-8} coulombs/cm^2 at their respective interfaces. G is in units of mho m^2).

(a,b) C-V and G-V curves for suppressed a.c. surface state response.

(c,d) C-V and G-V curves for normal surface state response.

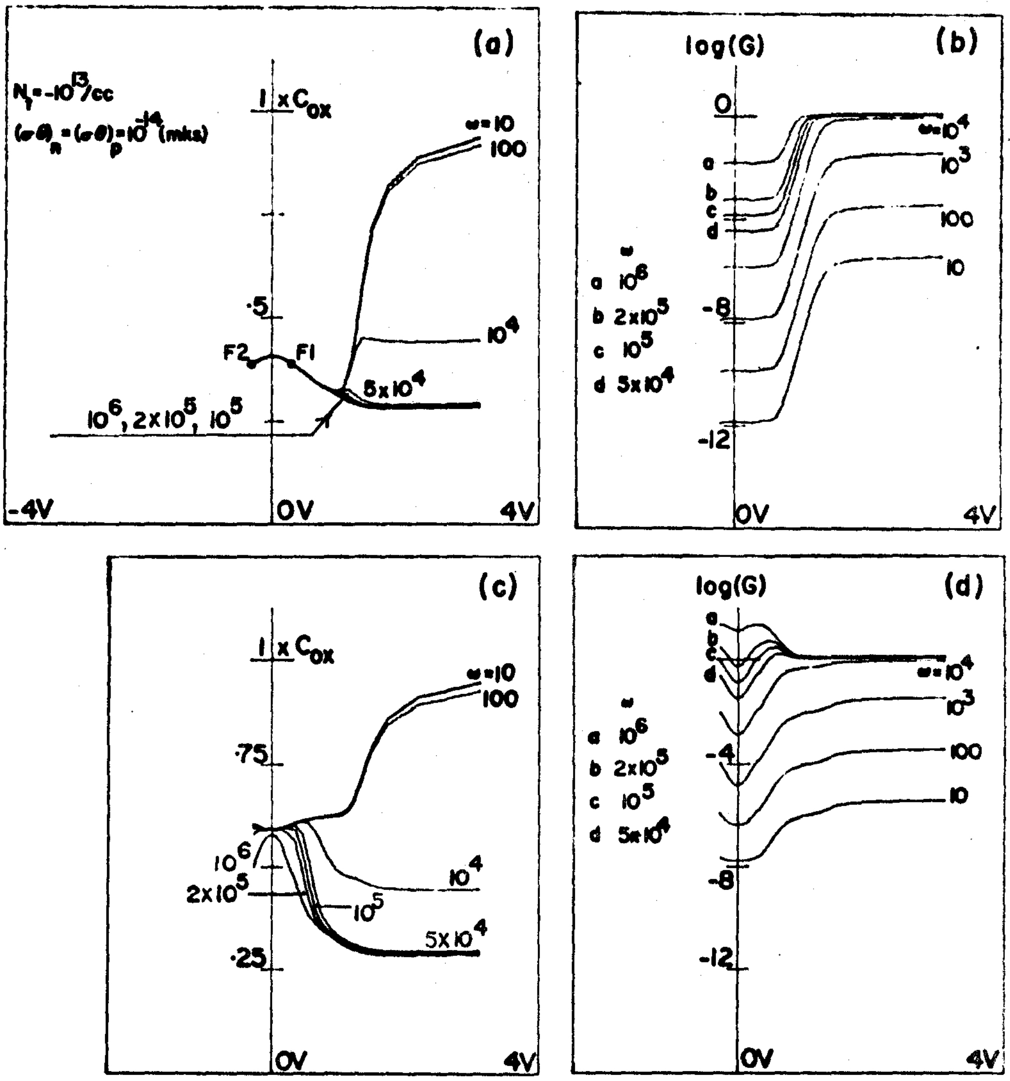
(a)
N_T = -10^13/cc
(σθ)_n = (σθ)_p = 10^-14 (mks)
1 x C_OX
ω=10
100
·5
10^4
F2
F1
5x10^4
10^6, 2x10^5, 10^5
-4V
0V
4V
(b)
log(G)
0
ω=10^4
10^3
100
10
a
b
c
d
-8
-12
ω
a 10^6
b 2x10^5
c 10^5
d 5x10^4
0V
4V
(c)
1 x C_OX
ω=10
100
·75
10^6
2x10^5
10^4
10^5
5x10^4
·25
0V
4V
(d)
log(G)
a
b
c
d
ω=10^4
10^3
-4
100
10
-8
-12
ω
a 10^6
b 2x10^5
c 10^5
d 5x10^4
0V
4V

Figure 31

T = 325°K, T = 300°K and T = 275°K (figs. 32(a), (d), (f)). G-V curves for both "suppressed" and "normal" surface state response are given for corresponding temperatures in figs. 32(b), (c), (e), (f), (h) and (i). Both semiconductors are identical, p-type (doped to 10^{15}/cc) with the same surface state distribution (Surface State Distribution 1) and fixed charge (-3.2×10^{-8} coulombs/cm^2) at each interface. All of the temperature effects which were reported for the MIS case are seen in the p-i-p system of fig. 32. The C-V curves show progressively lower values of ω_{inv} as the temperature is decreased, reflecting poorer coupling between majority and minority band currents. Corresponding to the reduction in ω_{inv} is a reduction in the high frequency (above ω_{inv}) conductance background level and an increase in the low frequency (below ω_{inv}) conductance.

Temperature also affects surface state response by cutting off response from states furthest away from the majority band edge as temperature is lowered. This explains the C-V temperature response and also explains the shift of the surface state conductance peak with temperature (ie., left towards accumulation with decreased temperature in going from fig. 32(c) to 32(f) to 32(i)). The shift in the flat band bias points (denoted by F1 and F2 in fig. 32) is a d.c. surface state charge effect which is also seen in the MIS case$^{(11,19)}$.

Figure 33 shows some unusual low temperature curves. The n-i-n system depicted by the left hand figures, figs. 33(a), (c)

Figure 32 Effect of Temperature on the SIS Admittance (Both semiconductors are p-type doped at 10^{15}/cc. Both have Surface State Distribution 1 as well as a fixed charge density of -3.2×10^{-8} coulombs/cm^2 at their respective interfaces. G is in units of mho m^2).

(a,d,g) C-V curves for normal a.c. surface state response at 325°K, 300°K and 275°K respectively.

(b,c) G-V curves for suppressed and normal surface state response at 325°K.

(e,f) G-V curves for suppressed and normal surface state response at 300°K.

(h,i) G-V curves for suppressed and normal surface state response at 275°K.

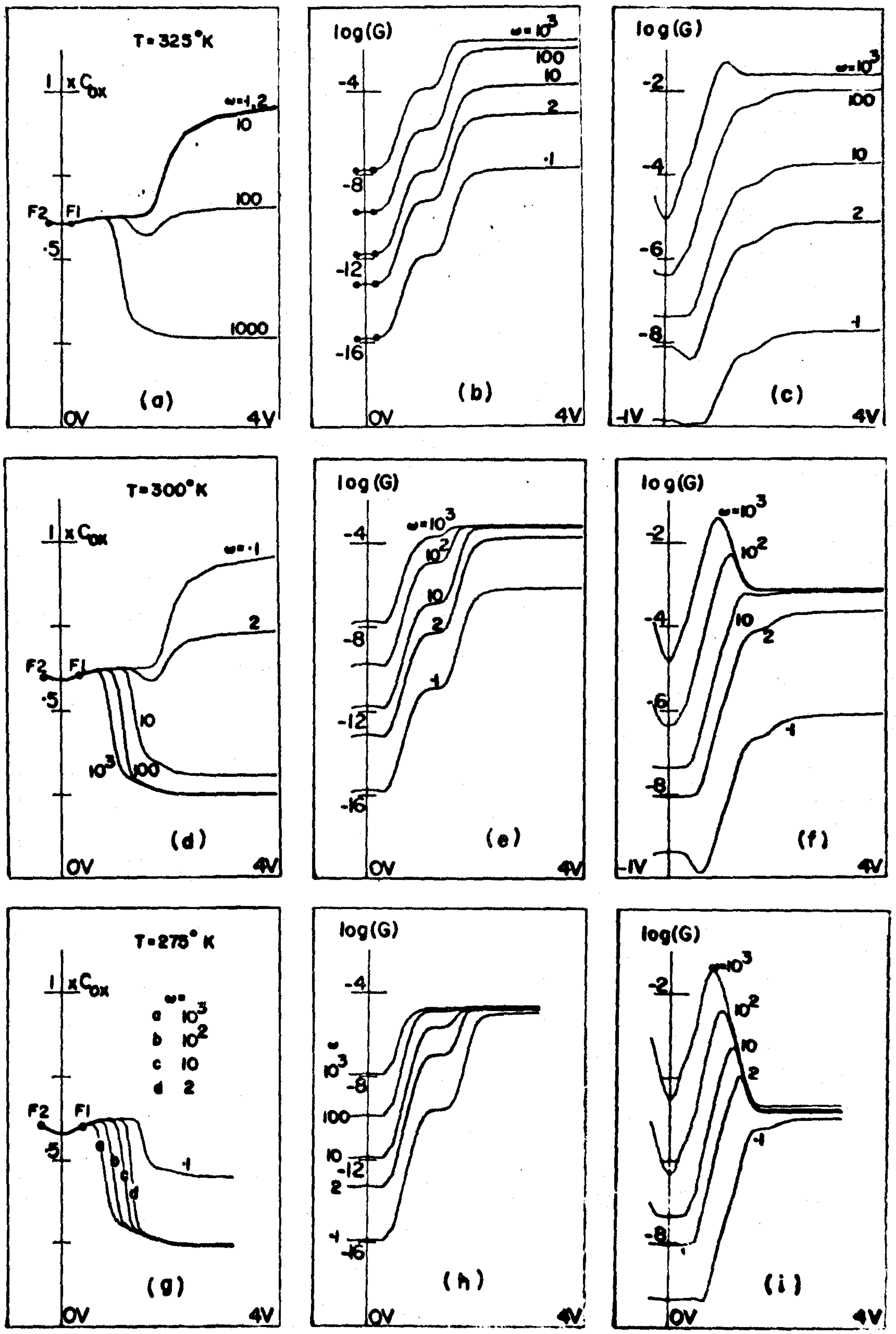
T=325°K
1 x C_OX
ω=1,2
10
100
1000
F2
F1
·5
(a)
OV
4V
log(G)
ω=10^3
100
10
2
·1
-4
-8
-12
-16
(b)
OV
4V
log(G)
ω=10^3
100
10
2
·1
-2
-4
-6
-8
(c)
-1V
4V
T=300°K
1 x C_OX
ω=·1
2
10
10^3
100
F2
F1
·5
(d)
OV
4V
log(G)
ω=10^3
10^2
10
2
·1
-4
-8
-12
-16
(e)
OV
4V
log(G)
ω=10^3
10^2
10
2
·1
-2
-4
-6
-8
(f)
-1V
4V
T=275°K
1 x C_OX
ω=
a 10^3
b 10^2
c 10
d 2
·1
F2
F1
·5
a
b
c
d
(g)
OV
4V
log(G)
ω
10^3
100
10
2
·1
-4
-8
-12
-16
(h)
OV
4V
log(G)
ω=10^3
10^2
10
2
·1
-2
-8
(i)
OV
4V

Figure 32

and (e), differs from the n-i-n system depicted by the right hand figures, figs. 33(b), (d) and (f), only in the fixed interface charge density (4.8 x 10^{-8} coulombs/cm^2 instead of 3.2 x 10^{-8} coulombs/cm^2). With this difference in fixed charge density, figs. 33(a), (c) and (e) correspond to case (iv) in figs 23 while figs. 33(b), (d) and (f) correspond to case (v). The difference in relative position of the depletion wells is the sole cause of the great difference in the observed effects.

The curves marked 'A' in figs. 33(a) and (b) show the $\omega = 0^+$ (ie., the low frequency limit) C-V response with normal surface state response. The curves marked 'B' illustrate suppressed surface state response which can be compared to the normal surface state response shown in figs. 33(c) and (d). The capacitance peaks that are seen in figs. 33(c) and (d) are unusual in the sense that they cannot be observed at higher temperatures (higher than 100°K, for example) since they would be masked by the coincident (and much larger) majority band charging.

The G-V curves are unusual in one or two respects. The very small band bending change at interface 1 as a result of the filling of the surface state distribution peak near the minority band edge causes the background conductance shelves observed in fig. 33(f) (at $\omega < .1$ and between 4 and 6 volts). The surface state conductance peaks are shifted with frequency in the normal way (towards accumulation) but are much more irregularly shaped and seem to disappear at high frequencies into the background conductance.

Figure 33 Low Temperature SIS Admittance (50°K) (Both semiconductors are n-type doped at 10^{15}/cc. Both have Surface State Distribution 1. The curves on the left side (a,c,e) have a fixed charge density at both interfaces of +3.2 x 10^{-8} coulombs/cm^2. The curves on the right side (b,d,f) have a fixed charge density at both interfaces of +4.8 x 10^{-8} coulombs/cm^2. G is in units of mho m^2).

(a,b) C-V curves marked 'B' show suppressed surface state response. Curves marked 'A' denote the $\omega = 0+$ low frequency limit with normal surface state response.

(c,d) C-V curves with normal surface state response.

(e,f) G-V curves with normal surface state response.

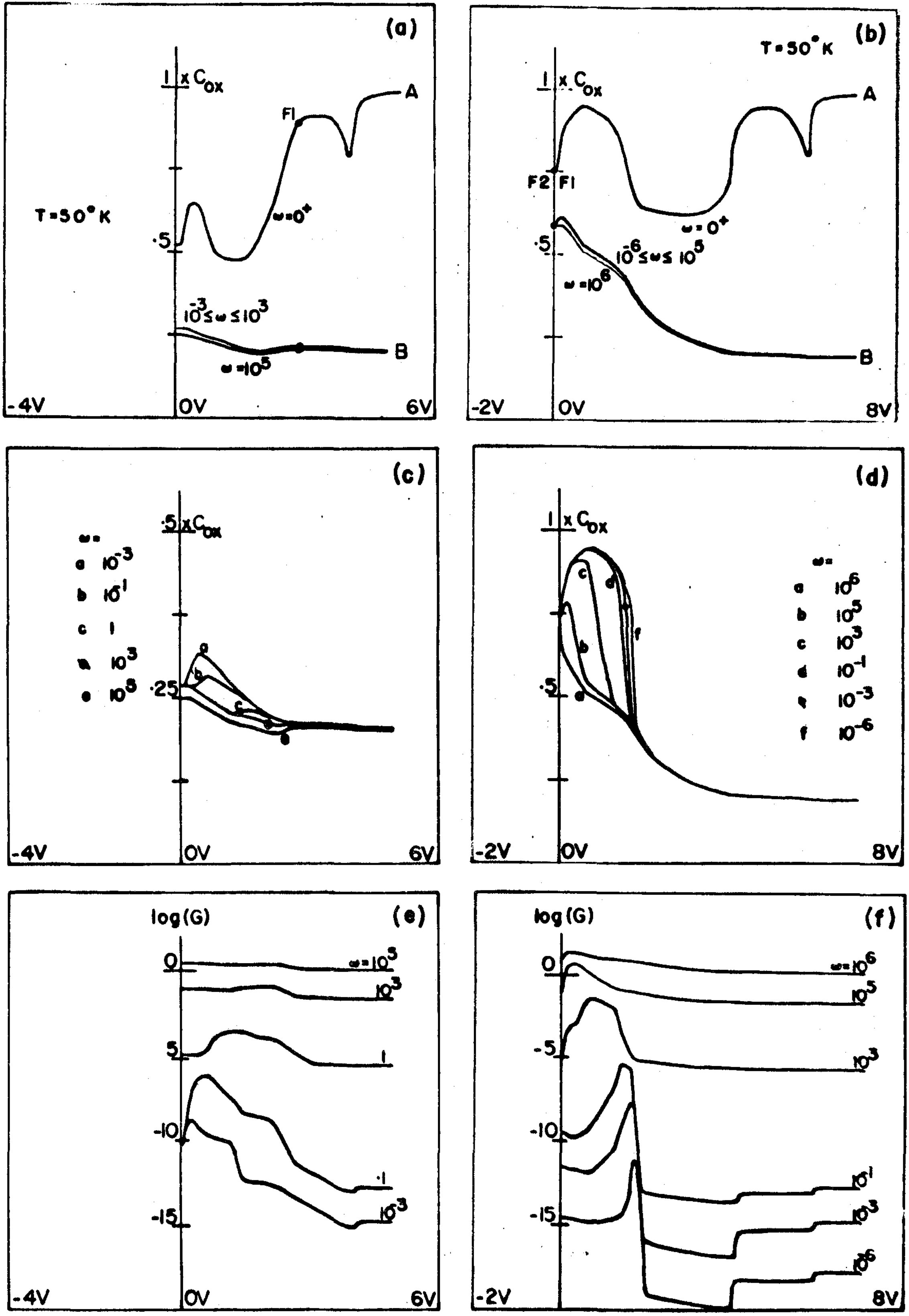
(a)
1 x C_{ox}
F1
A
T=50°K
·5
$\omega=0^+$
$10^{-3} \le \omega \le 10^3$
$\omega=10^5$
B
-4V
0V
6V
(b)
T=50°K
1 x C_{ox}
A
F2 F1
·5
$\omega=0^+$
$10^{-6} \le \omega \le 10^5$
$\omega=10^6$
B
-2V
0V
8V
(c)
·5 x C_{ox}
ω=
a 10^{-3}
b 10^{-1}
c 1
d 10^3
e 10^5
·25
a
b
c
d
e
-4V
0V
6V
(d)
1 x C_{ox}
ω=
a 10^6
b 10^5
c 10^3
d 10^{-1}
e 10^{-3}
f 10^{-6}
·5
a
b
c
d
e
f
-2V
0V
8V
log(G)
(e)
0
$\omega=10^5$
10^3
5
1
-10
·1
-15
10^3
-4V
0V
6V
log(G)
(f)
0
$\omega=10^6$
10^5
-5
10^3
-10
10^1
-15
10^3
10^{-6}
-2V
0V
8V

Figure 33

The conductance irregularities, such as in the $\omega = 10^3$ curve of fig. 33(f) are the result of surface state response from the Gaussian shaped majority band side peak of the surface state distribution (see fig. (13)).

11. Summary of SIS Admittance Behaviour

The exact solution for the small signal complex admittance, applied previously to the MIS device, has been utilized to generate exact C-V and G-V characteristics for the SIS device. The response has been investigated as a function of frequency, temperature, doping density, surface states, fixed charge and SRH center density. In addition, one non-equilibrium case has been presented with light stimulated hole-electron pair generation. For this case the accuracy is dependent on the assumption made in solving the d.c. problem.

Widely differing C-V characteristics can be obtained depending on the relative position of the depletion wells (See the cases given schematically in fig. 23). Some of these characteristics are unusual and could be useful in new types of varactor diodes. For example, fig. 25(e) shows a bell shaped high frequency response. This response could be broadened and raised by inserting appropriate fixed charge, or it could be made to fall off more rapidly to lower base values by decreasing the doping densities.

The G-V characteristics are complicated to analyze and have mainly been explained with the help of the approximation that either one or both of the semiconductor conductances are negligible with respect to the semiconductor reactances (ie., $\omega C_{S1} >> G_{S1}$ and/or $\omega C_{S2} >> G_{S2}$). This is generally the case as was shown in Table 2. The relative position of the depletion wells, the inversion layer cutoff frequencies, ω_1^{inv} and ω_2^{inv}, and the a.c. surface state response are the most important variables in determining the over all response. Understanding how these variables are affected by parameters such as temperature, SRH density, fixed charge and illumination with light allows one to qualitatively predict the various effects illustrated in figs. 26 to 33.

Both the G-V and C-V characteristics have been observed experimentally(59). Examples of fixed charge and surface state effects presented there show general agreement with the 'ideal' (ie., planar, no edge effects, etc.) theoretical results given in this chapter.

CHAPTER V

SIS D.C. TUNNELLING CURRENT EQUATIONS

1. Introduction

Because of their importance in device applications, considerable attention has been focussed on various types of tunnelling systems. Both theoretical and experimental investigations of such structures as the PN junction(36,37), the MIM (Metal-Insulator-Metal)(38-42) and the MIS (Metal-Insulator-Semiconductor)(43-47) have already been reported. On the other hand, the SIS device proposed by Shewchun(12) has received little attention. However, recent advances in the fabrication and analysis(59,34) of the thick insulator SIS device indicate that a theoretical treatment of the SIS thin insulator tunnelling device may have great practical significance.

This chapter deals with the theoretical problem of calculating the d.c. tunnelling characteristics of various SIS devices. To simplify the calculation, the semiconductors and the insulator were all assumed to be described by E(k) relationships with conduction band minima and valence band maxima at $\underline{k}_\perp = 0$ (where $\underline{k}_\perp$ is the component of $\underline{k}$ vector parallel to the IS interface and perpendicular to the electric field). Current components are assumed to result from allowed direct transitions conserving $\underline{k}_\perp$ as well as the energy E. With these assumptions* the problem is soluble in the independent particle approach(38). This method is adopted rather than a refinement of Shewchun's simple application of Fredkin and Wannier's(48) version of internal field emission(37). The assumptions Shewchun finds necessary to perform the calculations are difficult to justify(12). In addition, it is doubtful that his theory can be applied(49) across boundaries where the crystal structure changes. Shewchun's paper has merit, however, since it presents good arguments for the existence of the SIS negative resistance feature with a valuable comparison of its probable characteristics with those of the p-n junction.

Band-to-band and surface state-to-band tunnelling currents are calculated in this chapter using the WKB method (following the development of Freeman and Dalke(45)) or by a modification of Harrisson's(38) wave function matching treatment. The effective mass model of BenDaniel and Duke(50) will be applied throughout but in a somewhat trivial way. That is, the hole and electron band effective masses will be allowed to change, but only at the IS interfaces.

Momentum vectors, $\underline{k}$, for energies in the insulator (or semiconductor) bandgap are found by applying a two band barrier propagation approach. That is, wave propagation via the barrier conduction

---

*These conditions are satisfied in a number of important semiconductor systems provided they are correctly oriented, for example, the Si(1 0 0) orientation discussed in reference 47.

and valence bands are both taken into account. This is done by extending both the electron and hole bands into complex 'k' space(37,51,44) and writing the two band barrier propagation vector as a simple symmetric (for holes and electrons) analytic expression which will assymptotically approach the appropriate one band values near the barrier band edges(44). This leads to an E($\underline{k}$) insulator bandgap function which is hyperbolic in k^2 and is exactly that used by Freeman and Dalke(45) for surface state propagation at energies in the bandgap of the semiconductor. For SIS structures with high dopant impurity densities,the tunnelling current must be modified to include tunnelling through the space charge region of either one or both of the semiconductors. As will be shown, this is particularly important in the negative resistance region of the degenerate p-i-n device.

The solution of the d.c. bias problem (ie. the solution of the semiconductor band bending as a function of distance into the semiconductor) is done by the method of Temple and Shewchun(1) outlined in Chapter II. This method has a number of advantages. First, for the low d.c. current region, it has a prescribed accuracy. Second, it uses Fermi integrals over bands with arbitrary densities of states and can thus be applied confidently at bias voltages where the Fermi level is in the conduction or valence band. (This will be particularly important in considering the negative resistance region of the degenerate p-i-n device.)

However in regions of large tunnelling current, the solution breaks down unless a self-consistent solution of d.c. hole and electron band quasi Fermi level shifts can be found throughout the semiconductor. Because this problem is so complex, the d.c. bias solution will always assume that the tunnelling currents are too low to greatly disturb the thermal equilibrium charge distribution. Hence I-V characteristics in regions of large tunnelling current will be suspect, particularly if they contain large minority band components(47).

Even with all the options provided by the tunnelling solutions given in this chapter, there are still a number of valid points of criticism. Some of these concern the use of WKB wave functions(44,49). Others involve the use of the independent particle model,(38,43,49) and the implicit assumption of an effective mass model in (or even near) the insulator barrier region(49). Many alternative solutions have been proposed. Feuchtwang(49) has developed a generalized WKB approximation which does not require the effective mass formalism. Other researchers have tried a form of wave function matching with various adaptations for many particle effects(42,54). Still other investigators have attempted to utilize various forms of scattering theory(48,55,56). All of these theories give insight into the tunnelling problem in real materials but none have yet proved soluble for realistic systems. In order to obtain some insight into the present problem, we are forced to use a generalization of a combination of methods which, though criticized, have been used in the literature to date for the simpler MIS tunnelling system. When applied (in Chapter VI), some of the tunnelling characteristics obtained are quite different from those of other tunnelling structures. One such feature is the predicted(12) negative resistence region for the degenerate p-i-n case.

2. Band-To-Band Tunnelling

Following the usual approach(38,45,57) the tunnelling current for direct transitions of electrons through the barrier can be written as

$$I_{S1,S2} = \frac{me\ A}{2\pi^2\hbar^3} \int_{\substack{E \\ \text{allowed} \\ \text{bands}}} \int_{E_1=0}^{E_1\ \text{max}} (f_{S1}-f_{S2})\tau(E,E_1)\ dE_1\ dE \qquad (34)$$

where m is the electron mass, e is the charge, $2\pi h$ is Planck's constant, and A is the cross sectional area. The product of the occupation difference, $f_{S1}-f_{S2}$, times the barrier penetration probability, τ, is integrated over the transverse component of kinetic energy, E_1, and the total energy, E, of the allowed (direct) transitions. S1 and S2 are semiconductor 1 and 2 respectively.

This expression can be further broken down into individual current components, 8 of which will be considered as important when generating the I-V characteristics in Chapter VI. These are depicted in fig. 34 and include four band-to-band currents: I_{ee} (electron

Figure 34 Qualitative Energy Band Diagram of the SIS Device Showing the Various Band-to-Band and Band-to-Surface-State Current Components in an n-i-n System.

(a) Large negative bias applied to S1 (Arrows in direction of electron flow). I_{ee}, electron band of S1 to electron band of S2; I_{eh}, electron band of S1 to valence band of S2; I_{hh}, valence band of S1 to valence band of S2; I_{es}, electron band of S1 to surface states of S2; I_{sh}, surface states of S1 to valence band of S2.

(b) Large positive bias applied to S1 (arrows in direction of electron flow). I_{ee}; I_{hh}; I_{he}, valence band of S1 to hole bend of S2; I_{se}, interface states of S1 to electron band of S2; I_{hs}, valence band of S1 to interface states S2.

Note that ϕ_s is the electron work function (3.2 eV for Silicon) E_I is the insulator band gap (i. eV for SiO^2), E_G is the semiconductor band gap (1.121 eV for Si at T = 300° K) and ϕ_s' is the 'hole work function' defined by $E_i - E_G - \phi_s = 3.679$ eV for Si. X1 and X2 denote the IS interfaces of semiconductor 1 and 2 respectively.

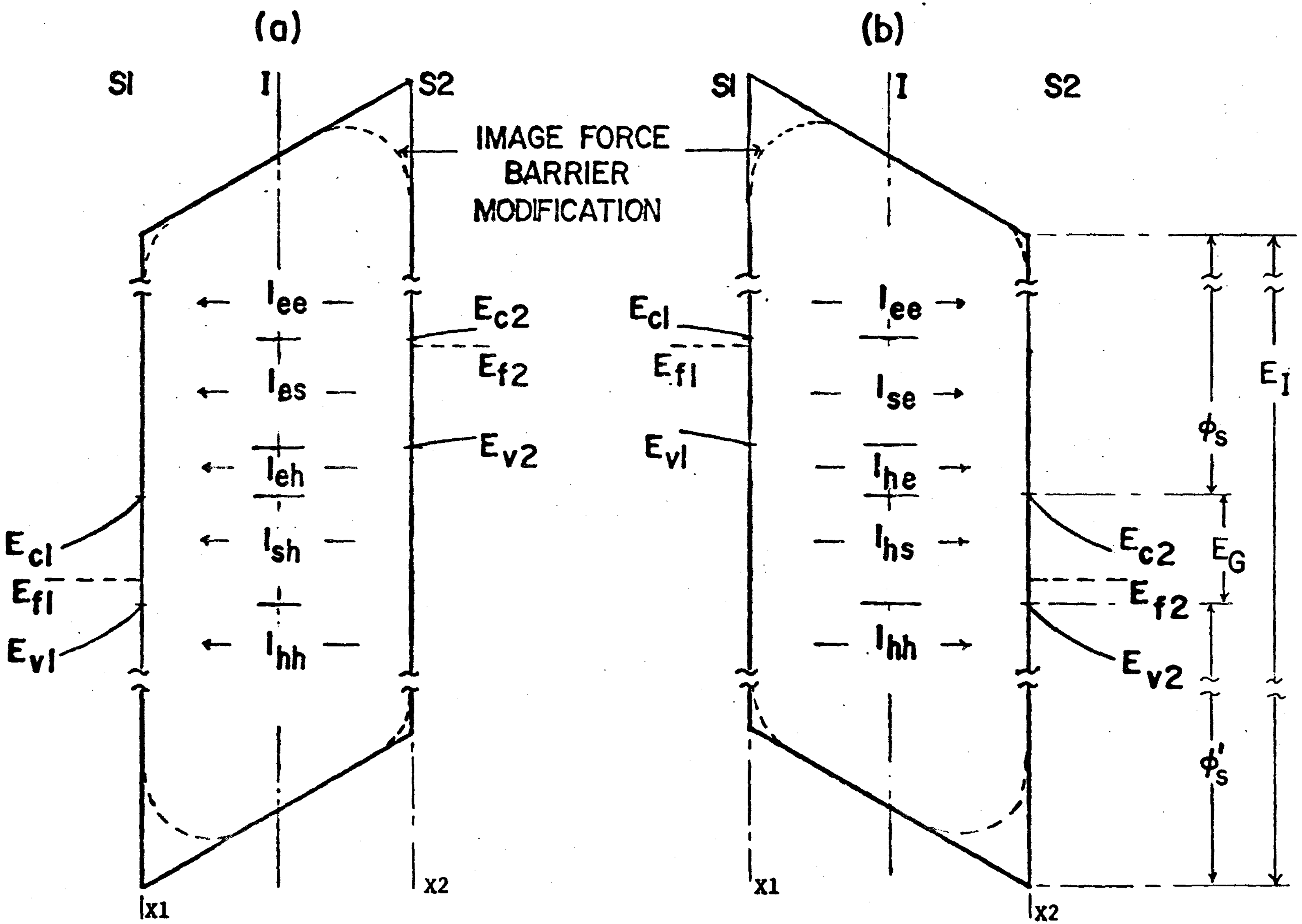
(a)
SI
I
S2
IMAGE FORCE BARRIER MODIFICATION
I_{ee}
I_{es}
I_{eh}
I_{sh}
I_{hh}
E_{c2}
E_{f2}
E_{v2}
E_{cl}
E_{fl}
E_{vl}
X1
X2
(b)
SI
I
S2
E_{cl}
E_{fl}
E_{vl}
I_{ee}
I_{se}
I_{he}
I_{hs}
I_{hh}
E_{c2}
E_{f2}
E_{v2}
ϕ_s
E_G
ϕ_s'
E_I
X1
X2

Figure 34

band of S1 to the electron band of S2), I_{eh} (electron band of S1 to the valence band of S2), I_{he} (valance band of S1 to the electron band of S2) and I_{hh} (valence band of S1 to the valence band of S2). To obtain the appropriate final current expression one, merely integrates over energies common to both bands with f_{S1} and f_{S2} being the Fermi functions appropriate to the bands being considered.

Four band-to-surface state currents are also considered: I_{se} (surface states at the S1 interface to the electron band of S2), I_{sh} (surface state of the S1 interface to the valance band of S2), I_{es} (electron band of S1 to surface states at the S2 interface) and I_{hs} (valence band of S1 to the surface states at the S2 interface). Expressions for these quantities are derived in Section 3 of this chapter.

Note that equation (34) can be applied to the MIS case by using the appropriate Fermi functions and integrating over the appropriate energy ranges.

The tunnelling probability is expressed in terms of the densities of initial and final states (at fixed E and E_1) and a matrix element, M_{LR}, of the current operator between left and right propagating states in the barrier. That is

$$\tau = 4\pi^2 \rho_{S1}\rho_{S2}|M_{LR}|^2 \tag{35}$$

where ρ_{S1} and ρ_{S2} are the semiconductor densities of states 1 and 2 at (E,E_1) and can be expressed for parabolic bands in the usual way

$$\rho_{S1} = \frac{L_1}{\pi} \frac{m_{S1}}{\hbar^2 k_{1x}} \; ; \; \rho_{S2} = \frac{L_2}{\pi} \frac{m_{S2}}{\hbar^2 k_{2x}} \tag{36}$$

where L_1 and L_2 are the extensions of semiconductors 1 and 2 perpendicular to the barrier, m_{S1} and m_{S2} are the effective masses at (E,E_1) and k_{1x} and k_{2x} are the x components of the wave vector $\underline{k}$.

(a) WKB Method

If left and right propagating waves in the barrier are written in the WKB format as

$$\psi_L = \frac{C_L}{\sqrt{\eta_b}} \exp - \int_{X1}^{x} \eta_b dx \; ; \qquad \psi_R = \frac{C_R}{\sqrt{\eta_b}} \exp - \int_{x}^{X2} \eta_b \, dx \tag{37}$$

where η_b is the x component of the barrier propagation vector, and X1 denotes the S1-I interface (see fig. 34 for schematic) and X2 denotes the I-S2 interface. Then

$$M_{LR} \equiv \frac{\hbar^2}{2m} \left(\psi_L^* \frac{d\psi_R}{dx} - \psi_R \frac{d\psi_L^*}{dx} \right)$$

$$= \frac{\hbar^2}{m} C_L^* C_R \exp - \int_{X1}^{X2} \eta_b \, dx \tag{38}$$

C_L and C_R are determined by matching to the wave function in semiconductors 1 and 2, and, upon normalization yield

$$C_L = \left[\frac{k_{1x}}{m_1^* \; 2L_1}\right] \text{and } C_R = \left[\frac{k_{2x}}{m_2^* \; 2L_2}\right] \qquad (39)$$

where m_1^* and m_2^* are effective mass ratios (ie. $m_1^* = \frac{m_1}{m}$ etc.).

Substituting for τ, equation (34) can be written as

$$I_{S1,S2} = \frac{me}{2\pi^2\hbar^3} \int\limits_{E} \int\limits_{E_1=0}^{E_{kinetic}} (f_{S1}-f_{S2})(\exp - \int\limits_{X1}^{X2} \eta(x)dx)dE_1 \, dE \qquad (40)$$

At fixed E, the barrier integral is strongly peaked at $E_1 = 0$ and several approximations can be made without loss of accuracy. Terms outside the exponential can be replaced by their values at $E_1 = 0$, η_b in the exponential can be expanded in a Taylor series about $E_1 = 0$, and the upper limit of integration of E_1 can be changed from E_{1max} to $E_1 = \infty$. The integration over E_1 is then trivial. That is

$$I_{S1,S2} = \frac{em\,A}{4\pi^2\hbar^2} \int\limits_{\substack{E \\ \text{allowed} \\ \text{bands}}} \left[\frac{(f_{S1}-f_{S2})(\exp-2 \int \eta_b \, dx)}{\int \frac{d\eta_b}{dE_1} \, dx}\right]_{E_1=0} dE \qquad (41)$$

To include propagation via both the barrier conduction and valence bands the propagation constant, η_b, is calculated as

$$\eta_b^{-2} = \eta_{CB}^{-2} + \eta_{VB}^{-2} \qquad (42)$$

where η_{CB} represents propagation via the barrier conduction band alone and η_{VB} represents propagation via the barrier valence band alone. These are given by

$$\eta_{VB}^2 = \frac{2m_{VB}}{\hbar^2} (E+E_1 - E_{VB}(x)) \tag{42a}$$

and

$$\eta_{CB}^2 = \frac{2m_{CB}}{\hbar^2} (-E+E_1 + E_{CB}(x)) \tag{42b}$$

where $E_{CB}(x)$ and $E_{VB}(x)$ are the barrier conduction and valence band edge energies as a function of x. Calculations given later in this work include image force modification$^{(40)}$ to both $E_{CB}(x)$ and $E_{VB}(x)$ (see fig. 34, for example).

(b) Wave Function Matching Method

If wave functions are matched across a barrier with a constant k_x vector, k_b, then τ becomes$^{(38)}$

$$\tau = 4\pi^2 \left|M_{LR}\right|^2 \rho_1\rho_2 = \frac{16 \frac{m_1}{k_1} \left(\frac{m_b}{k_b}\right)^2 \frac{m_2}{k_2}}{\left[\left(\frac{m_1}{k_1}\right)^2 + \left(\frac{m_b}{k_b}\right)^2\right] \left[\left(\frac{m_b}{k_b}\right)^2 + \left(\frac{m_2}{k_2}\right)^2\right]} \exp\left(-2\int_{X1}^{X2} \eta_b dx\right) \tag{43}$$

where k_1 and k_2 are the x components of vector $\underline{k}$ at X1 and at X2 respectively. (X1 and X2 denote the IS interfaces. See fig. 34.) k_b is taken as the x component of the propagation vector for a rectangular barrier of equal penetration probability. That is,

$$k_b = \frac{1}{X2-X1} \int_{X1}^{X2} \eta_b \, dx \tag{44a}$$

Similarly, m_b^* is an average two band effective mass ratio defined as

$$(m_b^*)^{1/2} = \left(\int_{X1}^{X2} \eta_b \, dx \right) \Big/ \left(\int_{X1}^{X2} \eta_b dx \Big|_{m_{CB}=m_{VB}=m} \right) \tag{44b}$$

Under the WFM (wave function matching) method, the tunnelling current becomes

$$I_{S1,S2} = \frac{4}{\pi^2} \frac{em}{\hbar^2} \int_{\substack{E \\ \text{allowed} \\ \text{bands}}} \frac{\frac{m_1}{k_1}\left(\frac{m_b}{k_b}\right)^2 \frac{m_2}{k_2} (f_{S1}-f_{S2}) \exp\left(-2\int_{X1}^{X2} \eta_b dx\right)}{\left[\left(\frac{m_1}{k_1}\right)^2 + \left(\frac{m_b}{k_b}\right)^2\right] \left[\left(\frac{m_b}{k_b}\right)^2 + \left(\frac{m_2}{k_2}\right)^2\right] \int_{X1}^{X2} \frac{d\eta_b}{dE_1} dx} \Bigg|_{E_1=0} dE \tag{45}$$

Note that this expression, unlike the WKB expression (41) for $I_{S1,S2}$, goes to zero at the band edges.

3. Band-to-Surface State Currents

(a) WKB Approach

Band-to-surface state currents, I_{es}, I_{hs}, I_{se} and I_{sh} are defined in Section 2 and are shown schematically in fig. 34. The current equations can be derived following the same steps as in Section 2. For a discrete level at the I-S2 interface, ρ_{S2} of equation (36) becomes

$$\rho_{S2} = 2N_i \, \delta(E-E_i) \tag{46}$$

where N_i and E_i are the density and energy of the i^{th} surface state level. Furthermore $|C_R|^2$ defined in equation (39) is now given by equation (47) below$^{(45)}$.

$$C_R^2 = 2\eta_b(X2)\eta_{ss} \tag{47}$$

where η_{ss} an average of the barrier propagation constant, $\eta_b(X2)$, and the two band semiconductor propagation constant, $\eta_s(X2)$. With E_i in the semiconductor band gap, η_s is given by

$$\eta_s^{-2} = \eta_C^{-2} + \eta_V^{-2}$$

with

$$\eta_C^2 = \frac{2m_c}{\hbar^2} \; (E_C-E_i) \text{ and } \eta_V^2 = \frac{2m_V}{\hbar^2} \; (E_i-E_V) \tag{48}$$

and

$$\eta_{ss} = \frac{\eta_b\eta_s}{\eta_b + \eta_s} \tag{49}$$

If a parameter σ_i is introduced such that $\sigma_i N_i$ represents the effective area of the i^{th} surface state level to tunnelling particles, then the band to surface state current for a surface state at interface 2 becomes

$$I_i = \frac{4eA}{\pi\hbar}\sigma_i N_i \frac{(f_{S1}-f_i)\eta_b(X2)\eta_{ss}(X2)}{\int \frac{d\eta_b}{dE}\,dx} \exp\left(-\int \eta_b\,dx\right)\Bigg|_{E_1=0} \qquad (50)$$

where f_i is the electron occupation of the i^{th} surface state level at the S2 interface.

Apart from the final result, this treatment is similar to that of Freeman and Dalke$^{(45)}$. Equation (50) represents an improvement in that it retains the exact denominator integral rather than an approximation.

(b) Wave Function Matching

By the wave function matching method, tunnelling from semiconductor 1 into the i^{th} level of the I-S2 interface requires k_2 and m_2 in equations (43) and (45) to be replaced by effective values η_{ss} and m_{ss}. η_{ss} has already been given in equation (49) and m_{ss} is a two band semiconductor effective mass, analogous to the two band barrier effective mass given in equation (44b). Hence

$$m^*_{ss} = \left(\frac{\eta_{ss}}{\eta_{ss}\big|_{m_C=m_V=m}} \right)^2 \qquad (51)$$

The resulting band-to-surface state current I_i becomes

$$I_i = \frac{32eA}{\pi\hbar} \; \frac{\sigma_i N_i (f_{S1} - f_i)\eta_b(X_2)\eta_{ss}(X_2)(\exp - \int \eta_b dx)\left[\frac{m_1}{k_1}\left(\frac{m_b}{k_b}\right)^2 \frac{m_{ss}(X2)}{\eta_{ss}(X2)} \right]}{\left[\left(\frac{m_1}{k_1}\right)^2 + \left(\frac{m_b}{k_b}\right)^2 \right] \left[\left(\frac{m_b}{k_b}\right)^2 + \left(\frac{m_{ss}(X2)}{\eta_{ss}(X2)}\right)^2 \right] \left[\int \frac{d\eta_b}{dE_1}\, dx \right]} \tag{52}$$

Current component I_{es}, for example, from the electron band of semiconductor 1 to the surface states of semiconductor 2, requires a summation over I_i over the allowed range of energy using the electron band values of f_{S1}, m_1 and k_1.

CHAPTER VI

TYPICAL SIS I-V TUNNELLING CHARACTERISTICS

1. Introduction

The SIS I-V characteristics presented in this chapter consider the effect of such parameters as temperature, insulator thickness, semiconductor doping density, interface states and fixed charge at the IS interfaces. However, the curves shown do not reflect the important problem of semiconductor carrier supply to the IS interface. This in effect assumes no d.c. quasi Fermi level shifts for the semiconductor carrier bands and automatically limits the current range* over which the analysis is valid. Fortunately, many of the interesting I-V features occur within one or two volts of zero bias where the currents are indeed small. In considering current components which tunnel to or from a minority carrier band, some sort of saturation effect should be expected in the high current region. The semiconductor has either an excess or a lack of minority carriers. If the semiconductor is biased in

---

*An accurate estimate of the upper limit for the various current components can be calculated utilizing the solution of the semiconductor a.c. transmission line model. This procedure is described in Chapter VII.

inversion a highly non-equilibrium charge density results which changes the voltage distribution throughout the semiconductor. This change in voltage distribution affects all of the current components including the majority band-majority band component(47).

Section 2 of this chapter is devoted to a study of the non-degenerate SIS system while Section 3 is devoted to the degenerate case. All of the I-V characteristics are calculated using the k dependent, and thus energy dependent, prefactor (see equation (43) of Chapter V) associated with the WFM (Wave-Function-Matching) method rather than by the WKB method which has no energy dependent prefactor*. Clarke(47) did not find any significant change in MIS electron band-to-metal I-V curve shape when calculated by either method. This is largely due to the generally overwhelming dominance of the exponential factor in $\tau(E)$ (see equation (43)). Only at energies near a band edge, where the WFM prefactor goes to zero, does the WFM prefactor dominate. However, this effect is masked by the much larger contribution to the current from energies further into the band which have smaller effective tunnelling barriers. What does occur is a reduction in total current. Unfortunately this difference cannot be capitalized upon since, in experimental situations, the effective tunnelling area is generally unknown(47,58), particularly in the thinner insulator cases.

Figure 35 shows a comparison of the total current in a typical

---

*This is one of the criticisms of the independent particle method when calculated with the WKB approximation and is commented upon by Harrison(38), Shewchun(12) and others.

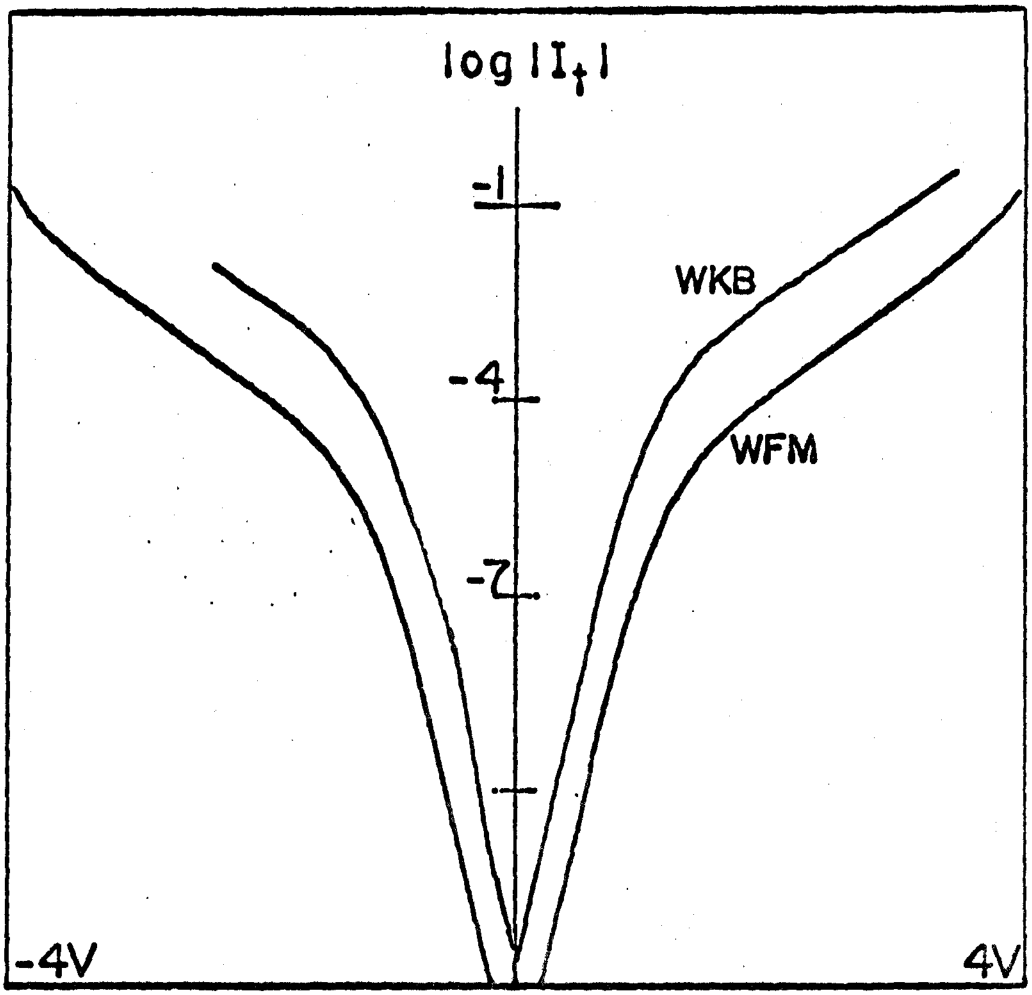

Figure 35 Comparison of the WKB and WFM (Wave Function Matching) Calculation of a Typical SIS I-V Characteristic (Semiconductor 1 is p-type doped at 10^{15}/cc while Semiconductor 2 is n-type doped at 10^{15}/cc. Both IS interfaces have "Surface State Distribution 3" as shown in fig. 13. Oxide thickness is 30 Å and T = 300° K).

non-degenerate p-i-n device when calculated with and without the WFM energy dependent prefactor. The change in current magnitude with little or no change in curve shape serves to illustrate the comments made and would, in fact, justify neglecting the prefactor, provided an arbitrary current scale was used(47). Though more difficult to solve, current equations (43) and (52) with the WFM prefactor do answer some of the criticisms of the simple WKB solution and are used for the calculation of all other SIS tunnelling current components in this chapter.

2. SIS I-V Characteristics for the Non-Degenerate Case

(a) Effect of Thickness (n-i-n and p-i-n cases)

Figure 36 shows the four band-to-band currents and the total device current, I_t, for the n-i-n and p-i-n configurations at 25, 30 and 35 Å. Increasing the thickness increases the effective tunnelling barrier and reduces the current magnitude with little or no effect on the shape of the I-V characteristics. With a combination of thinner barriers and larger biases one might expect to see differential effects due to image force barrier reduction. Such effects, however, are unlikely to be observed experimentally since they would entail high current densities unsupportable by the semiconductor carrier supply.

(b) General I-V Features

A general discussion of the I-V characteristics as typified by fig. 36 is useful at this point. Consider first the intraband currents I_{ee} and I_{hh} in figs. 36(a) and (b). The current I_{ee} goes

Figure 36 Effect of Oxide Thickness on the I-V Characteristics of a Typical SIS Tunnelling Diode. ('S1' and 'S2' are both doped at 10^{15}/cc with 'Surface State Distribution 3' (see fig. 13) at the IS interfaces. There is no fixed charge and T = 300° K. I is in amps and the device area is 1 m^2.)

'c' denotes the n-i-n case with insulator thickness of 25 Å.
'e' denotes the p-i-n case with insulator thickness of 25 Å.
'a' denotes the n-i-n case with insulator thickness of 30 Å.
'b' denotes the p-i-n case with insulator thickness of 30 Å.
'd' denotes the n-i-n case with insulator thickness of 35 Å.
'f' denotes the p-i-n case with insulator thickness of 35 Å.

Letters a to f on a dashed section line indicate the order that it intersects the I-V curves. Letters A and B mark features which are discussed in the text.

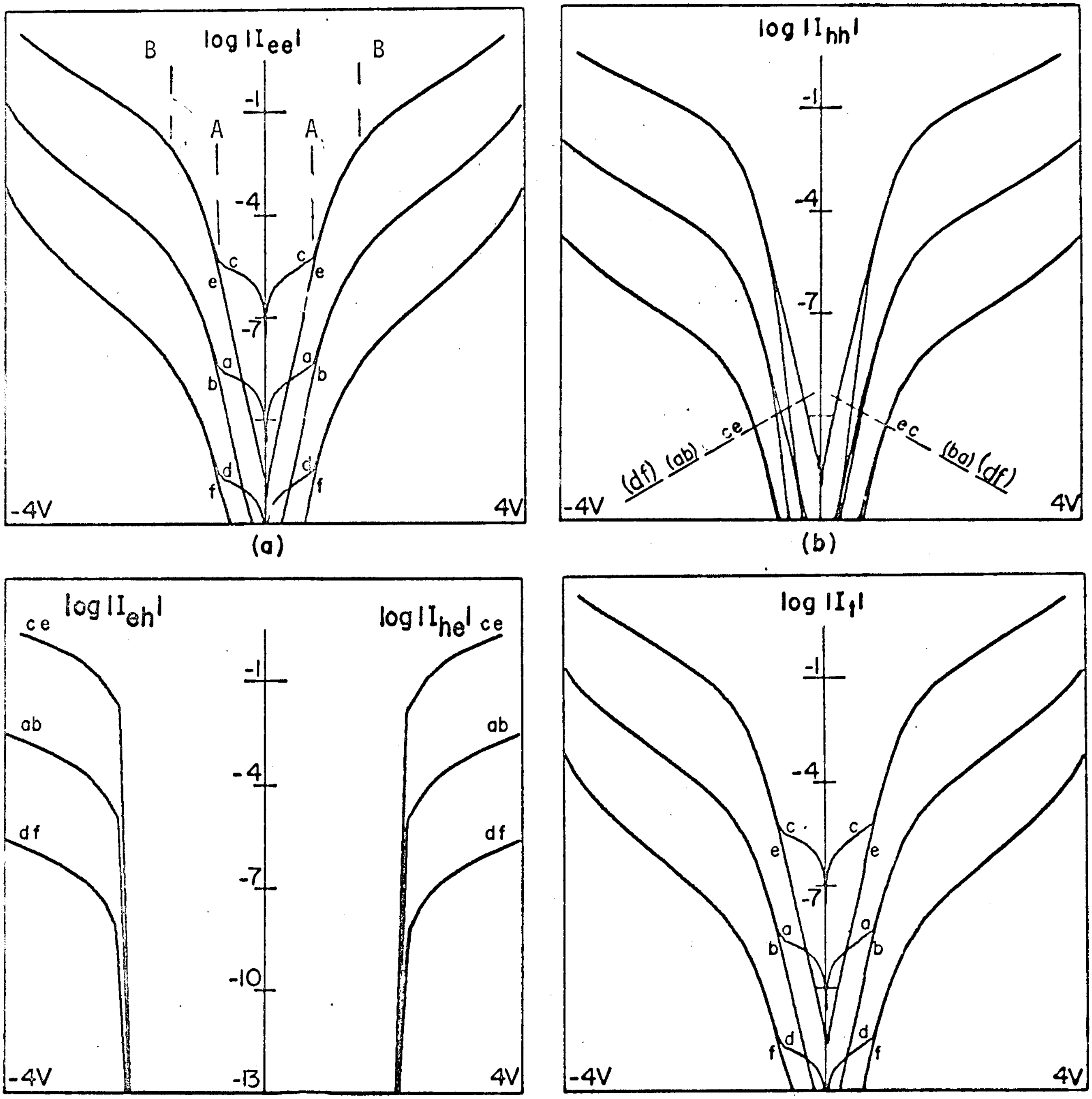

(a) (b)

(c) (d)

Figure 36

through zero at zero bias where $f_{e1} - f_{e2} \equiv 0$. For voltages between $\pm$ "B" (as marked in fig. 36) $f_{e1} - f_{e2}$ is increasing rapidly* for those electrons which see the smallest barrier. For voltages greater than + 'B' and less than - 'B', f_{e1} and f_{e2} change very little and the increase in current depends mostly on the decrease in effective barrier. In the p-i-n case between zero and "B" and in the n-i-n case between 'A' and 'B', log $|I|$ exhibits its most rapid change with voltage through the conbined effect of barrier reduction and increase in $f_{e1} - f_{e2}$. In the n-i-n case between zero and "A", log $|I|$ changes quite slowly with voltage. This is due to the fact that both semiconductor interface charge densities are quite low as both interfaces are biased fairly close to flat band. Thus, when the voltage changes across the device , a large fraction of the change drops across the semiconductor leaving a smaller fraction to fall across the insulator. Hence the effective barrier is a much less sensitive function of applied voltage. In the p-i-n case, however, there is a considerable interface charge density at zero bias as both interfaces are biased well into depletion.

The same properties are seen in the I_{hh} characteristics with the difference being that the p-i-n currents are larger than the n-i-n currents. This is due to the far greater values of f_{h1}

---

*This change is approximately exponential in $\frac{\Delta V_{int}}{kT}$ where ΔV_{int} is the portion of the change in applied bias which falls across the semiconductor, ie. the change in interface band bending.

and f_{h2} at low biases in the p-i-n case.

Interband currents, I_{eh} and I_{he} (fig. 36c),are not allowed until a bias at which the hole band edge of one semiconductor is at a higher value of energy than the electron band edge of the other semiconductor. A considerable amount of band bending is generally required. Hence, for larger biases, all changes in voltage appear almost entirely across the insulator. $f_{S1} - f_{S2}$ is approximately unity. The observed characteristics thus depend chiefly on the variation of the effective barrier with voltage.

(c) The Effect of Temperature (n-i-n and p-i-n Cases)

Figure 37 shows the four band to band currents and the total current I_t for the n-i-n and p-i-n configurations at T = 200°K and T = 400°K for an insulator thickness of 30 Å. (Note that the T = 300°K curve for the same system is shown in fig. 36 as cases 'a' and 'b'). The general characteristics pointed out in subsection (b) are all evident in the I-V curves of fig. 37. As expected, the voltage range over which the I-V curves are sensitive to temperature is the region in which the temperature dependent Fermi function factor, $f_{S1} - f_{S2}$, plays a role. All of the T = 400°K currents are larger. The voltage point at which the n-i-n and p-i-n characteristics separate shifts with temperature in the appropriate manner. That is, the higher the temperature, the greater the semiconductor charge densities and the lower the bias at which the voltage change appears entirely across the insulator.

The point at which the interband currents, I_{eh} and I_{he}, turn on differs. For the low temperature case, more applied

Figure 37 Effect of Temperature on the I-V Characteristics of a Typical SIS Tunnelling Diode (Both semiconductors are doped at 10^{15}/cc with "Surface State Distribution 3" (see fig. 13) at the IS interfaces. Insulator thickness is 30 Å. I is in amps and device area = 1 m^2).

'a' denotes the n-i-n case at T = 200°K.

'b' denotes the p-i-n case at T = 200°K.

'c' denotes the n-i-n case at T = 400°K.

'd' denotes the p-i-n case at T = 400°K.

Note that the T = 300° cases are given in fig. 36.

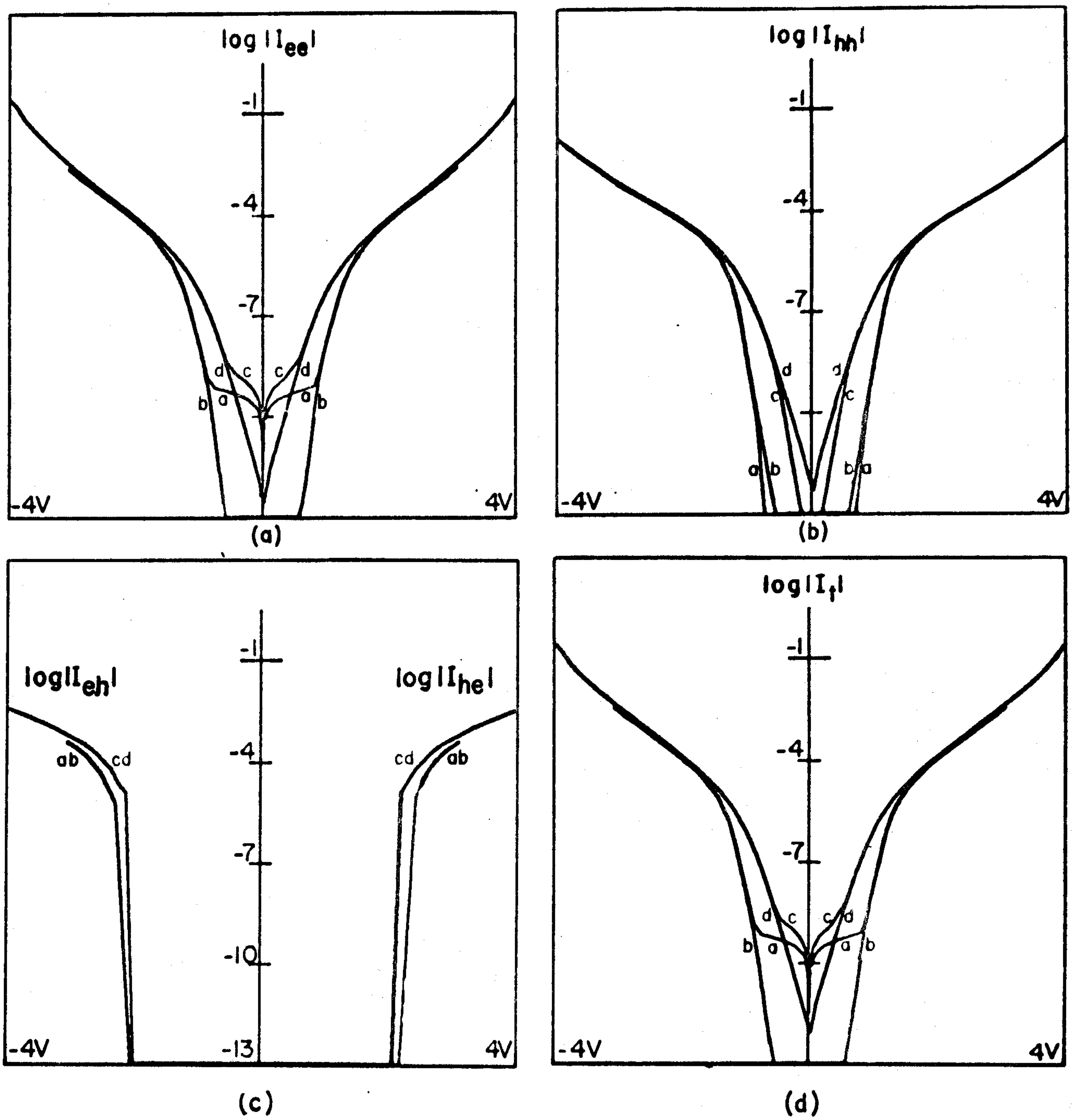
log|I_ee|
-1
-4
-7
d c c d
b a a b
-4V
4V
(a)
log|I_hh|
-1
-4
-7
d d
c c
a b b a
-4V
4V
(b)
log|I_eh|
ab
cd
log|I_he|
cd
ab
-1
-4
-7
-10
-13
-4V
4V
(c)
log|I_t|
-1
-4
-7
d c c d
b a a b
-4V
4V
(d)

Figure 37

voltage is required for the same value of insulator voltage drop since more semiconductor band bending is required to establish the same electric field in the oxide. The turn-on voltage changes by just this difference.

(d) Effect of Surface States

Surface states contribute to the overall I-V characteristics in two ways. First, they affect the d.c. bias solution. This is reflected in a change of the band-to-band current components shown in figs. 38 (a,b,c). The low voltage solution biases the interfaces with either more or less semiconductor band bending (affecting the size of the Fermi functions) depending on the total value of the surface state charge. Second, the greater the surface state density at the Fermi level, the greater the proportion of insulator to semiconductor voltage drop for any change in applied bias. These two points explain why the larger surface state density (Distribution '1' of fig. 13) causes the higher value of I_{ee} over the low voltage range as well as the smaller rate of increase with applied bias. Note also that the n-i-p characteristics are no longer approximately symmetric in voltage.

The surface state currents from the surface states at interface 1 to the hole and electron bands of semiconductor 2, I_{sh} and I_{se}, are shown in fig. 38 (e), while the surface state currents from the surface states at interface 2 to the hole and electron bands

Figure 38 Effect of Different Surface State Distributions on the I-V Characteristics of a Typical SIS Tunnelling Diode ('S1' and 'S2' are both doped at 10^{15}/cc. Insulator thickness is 30 Å and T = 300°K. I is in amps and device area = 1 m^2).

'a' denotes the n-i-n case with "Surface State Distribution 1" at both IS interfaces.

'b' denotes the p-i-n case with "Surface State Distribution 1" at both IS interfaces.

'c' denotes the n-i-n case with "Surface State Distribution 2" at both IS interfaces.

'd' denotes the p-i-n case with "Surface State Distribution 2" at both IS interfaces.

Note that "Surface State Distributions 1 and 2" are given in fig. 13. Letters a to d on a dashed section line indicate the order that it intersects the I-V curves. Letters A mark features discussed in the text.

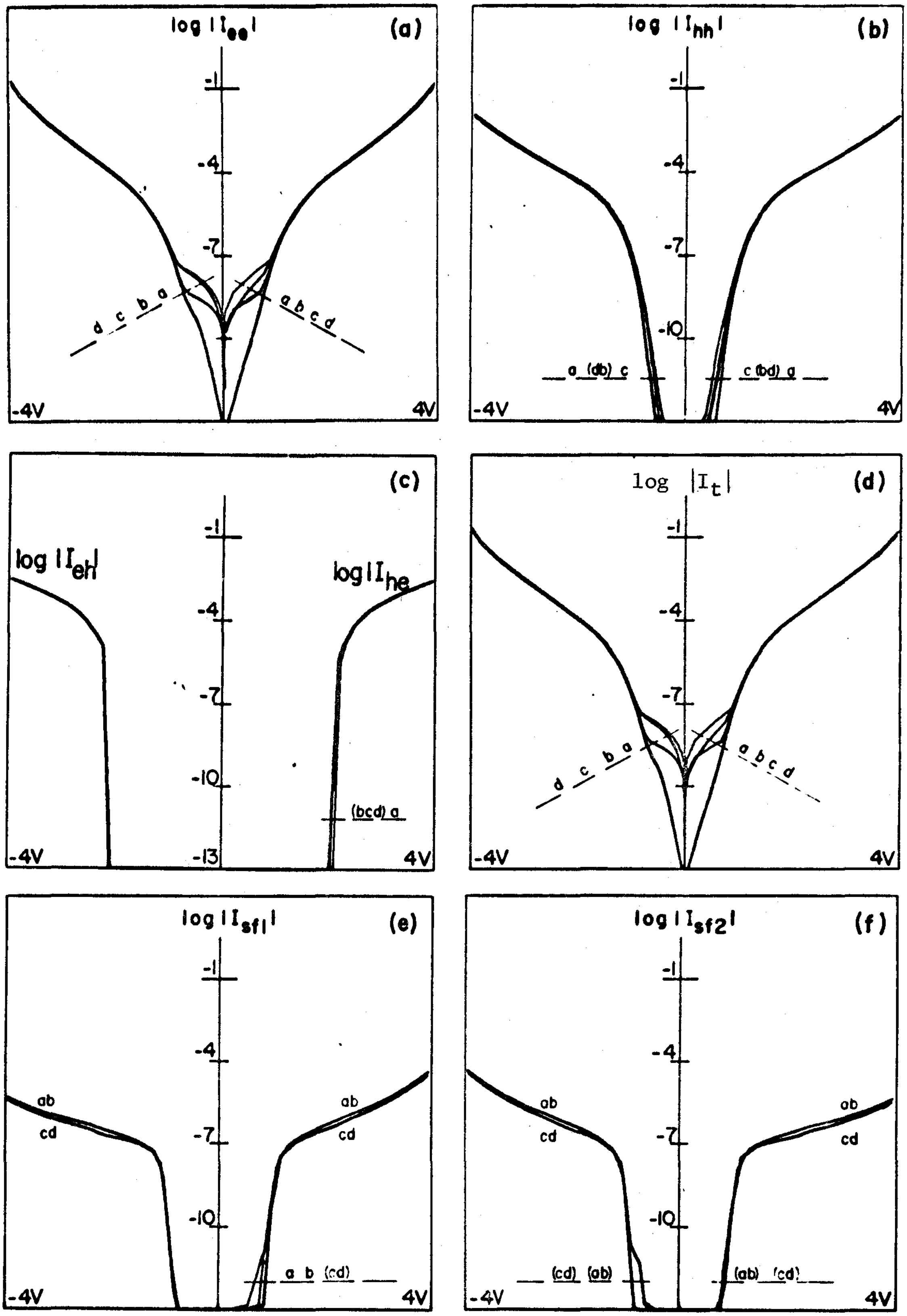
log |I_ee|
(a)
-1
-4
-7
d c b a
a b c d
-4V
4V
log |I_hh|
(b)
-1
-4
-7
-10
a (db) c
c (bd) a
-4V
4V
(c)
log |I_eh|
log |I_he
-1
-4
-7
-10
-13
(bcd) a
-4V
4V
log |I_t|
(d)
-1
-4
-7
d c b a
a b c d
-4V
4V
log |I_sf1|
(e)
-1
-4
-7
-10
ab
cd
ab
cd
a b (cd)
-4V
4V
log |I_sf2|
(f)
-1
-4
-7
-10
ab
cd
ab
cd
(cd) (ab)
(ab) (cd)
-4V
4V

Figure 38

of semiconductor 1, I_{es} and I_{hs}, are shown in fig. 38 (f). These currents can be expected to exhibit extra energy dependences on N_{ss}, η_{ss} and $\eta_b(X2)$ in equation (52) in addition to the regular dependence on $f_{S1} - f_{S2}$, $\tau(E)$ and on the requirement of direct transitions. For small voltages the tunnelling currents are low due to the high barrier and due to the fact that the tunnelling is into the low density midgap region of the surface state distribution. I_{es} in fig. 38(f) best illustrates the current change in going from Surface State Distribution 1 (cases 'a' and 'b') to Distribution 2 (cases 'c' and 'd').

The slower increase in surface state current at large bias values as compared to that of the band-to-band currents is explained by the variation near the band edge of N_{ss_i} (see fig. 13) and η_{ss} (see equation (49)). For voltages $\gtrsim 1.3$ volts or $\lesssim -1.3$ volts, the surface state current is from (or into) an increasing number of surface state levels in a region where η_{ss} and N_{ss} are slowly varying. At larger voltages currents become "allowed" from the Gaussian peaked portions of the distribution where first an increase in N_{ss} outweighs the decrease in η_{ss} and then both quantities decrease rapidly. Since these particular components face the smallest effective tunnelling barrier, the effect is a relatively sharp elbow in the surface state-to-band current components.

(e) Effect of Fixed Charge on the IS Interfaces

Figure 39 shows the four band-to-band currents for both the

Figure 39 The Effect of Fixed Interface Charge on the I-V Characteristics of a Typical SIS Tunnelling Diode. (Both semiconductors are doped at 10^{15}/cc with "Surface State Distribution 3" (see fig. 13) at the IS interfaces. Oxide thickness is 30 Å and T = 300°K. I is in amps and the device area is 1 m^2).

'a' denotes the n-i-n case with no fixed charge at either IS interface.

'b' denotes the p-i-n case with no fixed charge at either IS interface.

'c' denotes the n-i-n case with 6×10^{-3} coulombs/m^2 at each IS interface.

'd' denotes the p-i-n case with -6×10^{-3} coulombs/m^2 at each IS interface.

Letters a to d on a dashed section line indicate the order that it intersects the I-V curves.

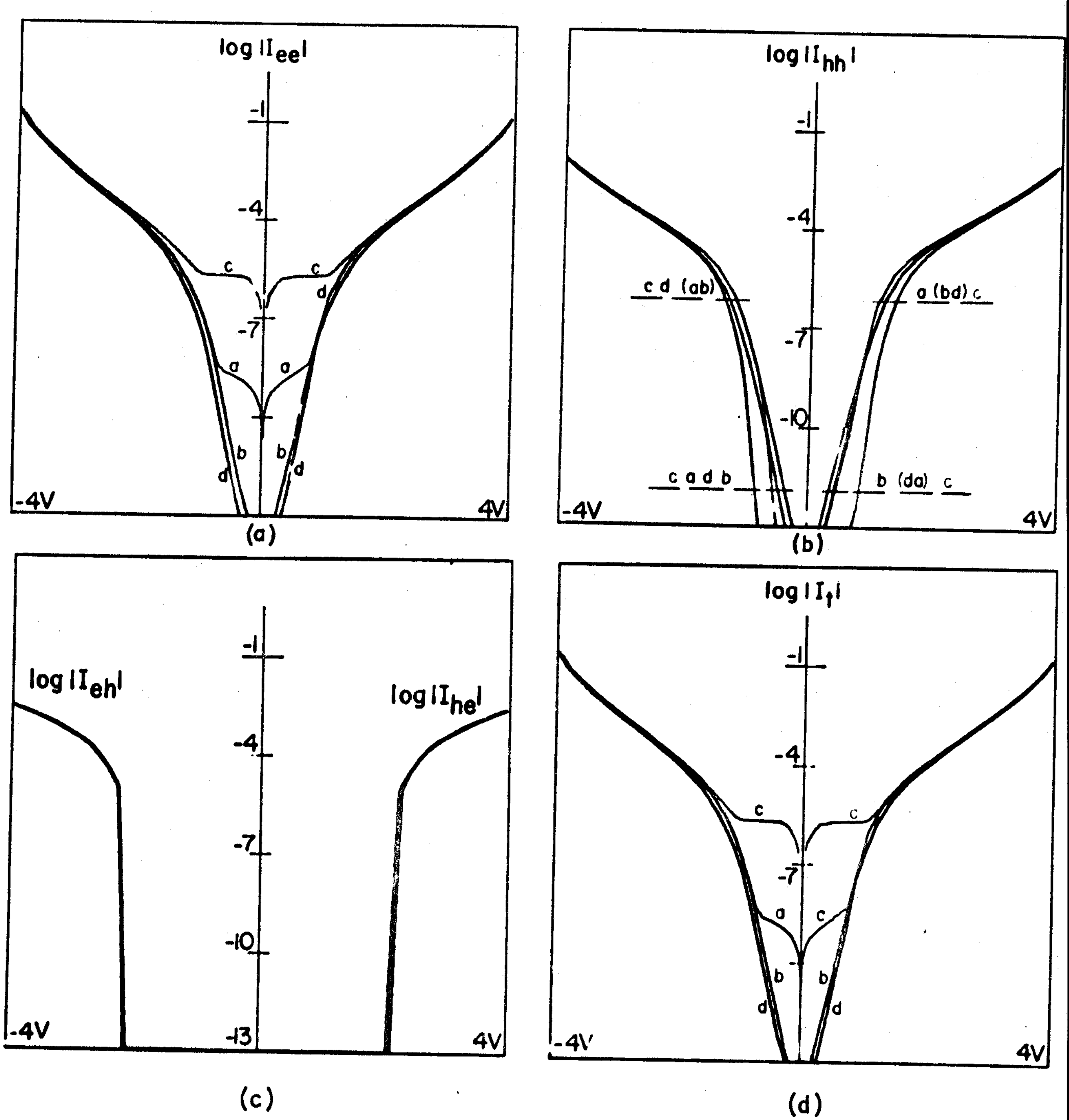
log |I_ee|
-1
-4
-7
c
d
a
b
-4V
4V
(a)
log |I_hh|
c d (ab)
a (bd) c
c a d b
b (da) c
-10
(b)
log |I_eh|
log |I_he|
-13
(c)
log |I_t|
(d)

Figure 39

n-i-n and p-i-n configurations with and without fixed charge densities at the IS interfaces. Cases 'a' and 'b' show typical curves without fixed charge,while cases 'c' and 'd' show the effect of + 1.6 x 10^{-3} coulombs/m^2 at the n-semiconductor interfaces and -1.6 x 10^{-3} coulombs/m^2 at the p-semiconductor interface. The effect is quite striking in the low voltage region. The n-i-n interfaces are biased into accumulation at zero bias, giving a larger I_{ee} current due to a larger value of $f_{e1} - f_{e2}$. The p-i-n I_{ee} value also increases as both the 'n' and 'p' interfaces, normally deeply depleted at zero bias, are now less depleted with larger electron band Fermi functions. The I_{hh} currents are also affected in the low voltage region with lower hole band Fermi functions and lower current magnitudes. The interband currents, I_{eh} and I_{he}, are shifted only slightly since only slightly more voltage is required before a direct interband transition is available.

(f) Effect of the Insulator Barrier Height and Semiconductor Work Functions

The effect in increasing barrier height is to increase the effective tunnelling barrier and reduce the magnitude of the tunnelling current components. The more interesting effects arise from varying the relative size of the various current components by changing the work functions. Up to this point no comments have been made concerning the relative importance of the various current components in figs. 36 to 39. Note that in all of these, I_{ee}, the electron band to electron band component, is dominant over the entire range of applied bias. Fig. 34(b) shows that the effective barrier height for the I_{ee} transition is approximately ϕ_s while the effective barrier height for the I_{hh} transition is ϕ_s'. In the p-i-n Si-SiO^2-Si system, ϕ_s' is greater than ϕ by approximately .5 eV. Hence the dominant I_{ee} component sees a relatively smaller effective tunnelling barrier. Naturally if ϕ_s and ϕ_s' were interchanged the I_{hh} component would dominate. Unfortunately the only hope for seeing a dominant I_{hh} component in Silicon is in the low bias p-i-p case with the semiconductors slightly accumulated. If the barrier were thin enough, or the temperature low enough, f_h might be large enough with respect to f_e to give the desired effect.

To see a voltage region in the Si - SiO^2 - Si system in which the currents I_{eh} or I_{he} dominate, requires the degenerate p-i-n system proposed by Shewchun(12). This system will be discussed in detail in the following section.

The observation of dominant surface state currents requires only a sufficiently large product for N_{ss_i} σ_i far enough from the semiconductor band edges so as not to be masked by the band-to-band components. One feature worth emphasizing in connection with surface state currents is the difficulty in separating their large d.c. bias effects from their actual tunnelling current contribution.

3. The Degenerate p-i-n System

(a) General Aspects

One of the problems associated with the independent particle approach is the range of integration for a particular tunnelling integral. In the pure WKB model, the only semiconductor band parameters in the band-to-band current equation (equation (42)) are the limits of integration. In the non-degenerate case these limits are well defined. However, in the degenerate case the "electron band"-"impurity centre" interaction leads to considerable band tailing effects and with a high enough impurity density, the "impurity centre"-"impurity centre" interaction causes a broadening of the impurity band. This problem has been treated approximately by Bonch-Bruyevich$^{(60)}$, and Kleppinger and Lindholm's equation$^{(25,30)}$ for the resultant Gaussian impurity band broadening has been adopted.

The description of the heavily doped semiconductor is difficult and open to question on a good many points. The most important of these is the question of whether some states can be considered localized while others cannot. In actual fact, the translational symmetry of the crystal is removed and all states suffer some degree of attenuation. In the non-degenerate system there can be at most one electron (hole) associated with each ionized impurity centre since, once an electron is localized in the vicinity, a second electron in the same vicinity is energetically unfavourable. In the degenerate system the electron is not bound to a single impurity centre. If its orbit is over a considerable number of unit cells there will tend to be two states, one for each spin, in the combined density of states function and there will be some finite probability of this electron tunnelling. For the degenerate p-i-n I-V calculations given in this section, some view must be taken to perform the calculations. The procedure adopted here is that of Kleppinger and Lindholm(25,30) and is described in the following paragraph. The actual equations used in the computer program to generate the density of states function of the combined band can be found in reference (25).

Figure 40 shows the conduction and impurity band merging to form one combined electron band. The Gaussian distribution associated with the impurity band broadening contains up to 2 N_{imp} non-localized states which can take part in the tunnelling process. It is important to be able to pick a value of the 'band edge', but there does not appear to be any good way to do this for a Gaussian distribution. The choice made in this chapter is shown in fig. 40(c) to be the energy $E = E_D - 2\sigma$ where σ is the variance of the distribution*. The small fraction of states (∿ 4%) below this value is considered 'localized' and unavailable for tunnelling.

Figure 41 gives the energy band schematic of a typical degenerate p-i-n device at zero bias. The range over which I_{he} transitions are allowed is shown as V_{-r}. With space charge tunnelling this range is extended to V'_{-r}. If the work functions of 'S1' and 'S2' are equal there is a voltage drop of magnitude $(E_{c1} - E'_{c2})/e$

---

*This choice coincides with that made by Morgan(62) and a plot of $E_D - 2\sigma$ versus doping concentration is given, for example, in reference 30.

Figure 40 Schematic Majority Band Density of States, g(E), in Degenerate and Non-Degenerate Semiconductors.

(a) The conduction band, showing a band tailing (the dashed curve) of β eV.

(b) The Gaussian broadening of the impurity bands (the dashed curve) to include 2 N_D electron states. This can be described by the form $\exp - ((\frac{E-E_D}{kT})^2/2\sigma^2)$.

(c) The resultant electron band (the solid curve) as compared to the old (non-degenerate) conduction band (the dashed curve).

Note that values of β and σ for figs. 42 to 45 are shown in Table 6.

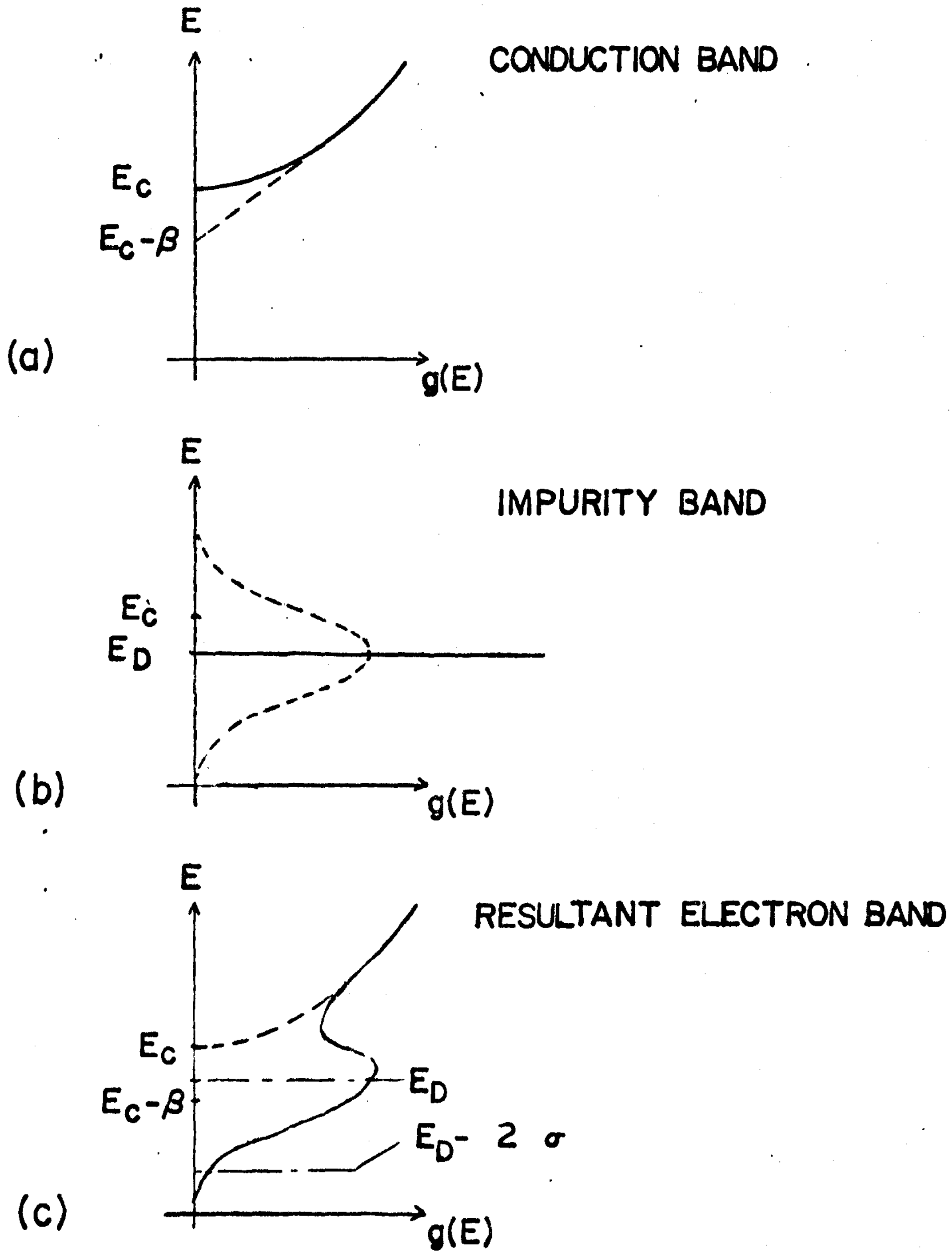
E
CONDUCTION BAND
E_c
$E_c-\beta$
(a)
g(E)
E
IMPURITY BAND
E_c
E_D
(b)
g(E)
E
RESULTANT ELECTRON BAND
E_c
E_D
$E_c-\beta$
$E_D-2\sigma$
(c)
g(E)

Figure 40

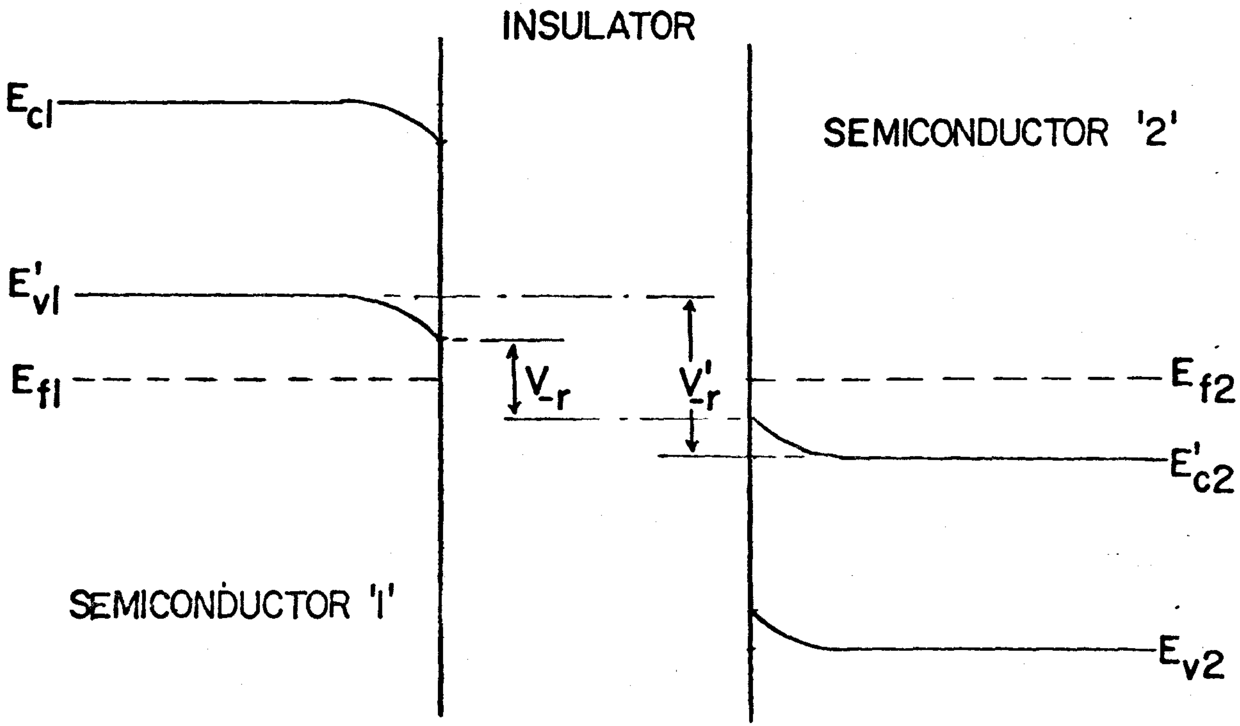

Figure 41 Schematic Energy Band Diagram of A Degenerate p-i-n Diode at Zero Bias. (V_{-r} and V'_{-r} indicate the expected voltage range of the negative resistance region with and without appreciable space charge tunnelling).

across the insulator. The resultant zero bias band bending in the semiconductors is required to match fields at the IS interfaces.

At zero bias the I_{he} current is zero since the Fermi functions are equal. Upon increasing the voltage, the electron occupation functions change, one increasing, the other decreasing. Hence a current flows. Increasing the voltage actually gives a slight increase in the effective barrier for states at E'_{v1}. But the more rapid increase in Fermi function difference results in an increasing I-V characteristics. At the same time, however, the range of allowed energy for the I_{he} transition decreases and I_{he} falls eventually to zero as the bands uncross, leaving the very small I_{ee} and I_{hh} components. The voltage required to eliminate the allowed 'he' transitions is approximately V'_{-r} (fig. 41), if there is large space charge region tunnelling, and approximately V_{-r}, if there is not. At a voltage of the order of the non-degenerate semiconductor bandgap, the I_{ee} current component becomes quite large and the net I-V characteristic returns to the normal sort discussed in Section 2 of this chapter.

(b) Effect of Thickness

The effect of four values of insulator thickness on the degenerate p-i-n negative resistance feature is shown in fig. 42. As was the case for the non-degenerate system the characteristics are merely displaced in amplitude, decreasing exponentially with increased thickness. Table 6 lists and compares amplitudes at .3 volts and at .95 volts. If there was no image force barrier

Figure 42 The Effect of Insulator Thickness on the Negative Resistance Region I-V Characteristics of a Typical Degenerate p-i-n Diode. (S1 is p-type, 10^{21}/cc. S2 is n-type, 10^{21}/cc. The temperature is 300°K. Both semiconductors have Surface State Distribution '3' (see fig. 13) at their respective IS interfaces. 'X' in the diagram indicates the log scale factor for each curve).

(a) Insulator thickness is 15 Å with X = 5.

(b) Insulator thickness is 20 Å with X = 2.

(c) Insulator thickness is 25 Å with X = -1.

(d) Insulator thickness is 30 Å with X = -4.

Note that log $|I|$ at .3 and .97 volts is tabulated in Table 6.

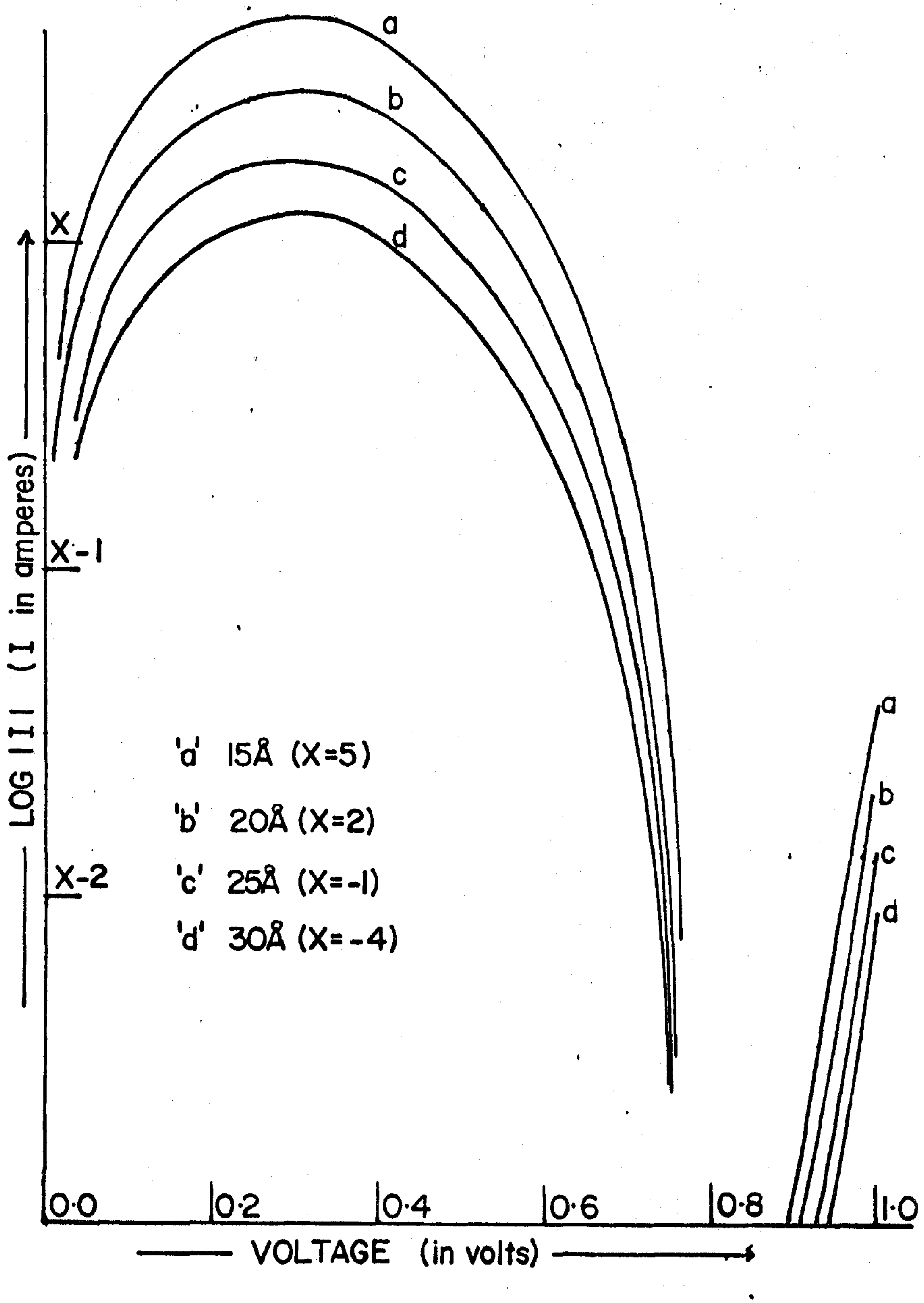
a
b
c
d
X
X-1
X-2
LOG | I | (I in amperes)
'a' 15Å (X=5)
'b' 20Å (X=2)
'c' 25Å (X=-1)
'd' 30Å (X=-4)
0·0
0·2
0·4
0·6
0·8
1·0
VOLTAGE (in volts)

Figure 42

TABLE 6

Comparison of Current Size at .30 and .95 Volts as a Function of Insulator Thickness (I in amps, see Fig. 42)

Thickness	Log |I| at .3 volts,	Δ log |I| (at .3 volts)	Log |I| at .97 volts,	Δ log |I| (at .97 volts)
15 Å	5.681		3.165	
		3.226		3.243
20 Å	2.455		$\bar{1}$.922	
		3.199		3.197
25 Å	$\bar{1}$.256		$\bar{4}$.725	
		3.181		3.171
30 Å	$\bar{4}$.075		$\bar{7}$.554	

modification, one might expect log |I| to increase linearly. Such is not the case, however, since, the thinner the oxide, the greater the relative image potential barrier reduction. This is seen in Table 6.

(c) Effect of Temperature

Figure 43 shows degenerate SIS I-V curves for three temperatures. The negative resistance region is relatively insensitive to temperature as $f_{s1} - f_{s2}$ is near unity and varies slowly with temperature. The voltage at which the I_{ee} current becomes dominant depends on temperature in the expected way. That is, the higher the temperature the greater the electron Fermi functions difference $f_{e1} - f_{e2}$.

(d) The Effect of Doping Impurity Density With and Without Space Charge Tunnelling

Figure 44 shows the I-V characteristics of a typical degenerate p-i-n system as a function of dopant impurity concentration. Both semiconductors were doped at 10^{22}/cc (case 'a'), 5 x 10^{21}/cc (case 'b'), 10^{21}/cc (case 'c'), 5 x 10^{20}/cc (case 'd') and at 10^{20}/cc (case 'e'). In order to discuss the important features illustrated in fig. 44, Table 7 was constructed. It shows energy band data (band tailing-β, and impurity band variance-σ) along with data obtained from the d.c. bias solution (interface band bending and the bulk energy of the impurity dopant band with respect to the Fermi level) and an estimate of the cutoff voltage of the negative resistance feature with and without space charge

Figure 43 The Effect of Temperature on the Negative Resistance Region of a Typical Degenerate p-i-n Diode. (S1 is p-type, 10^{21}/cc. S2 is n-type 10^{21}/cc. Insulator thickness is 25 Å. Both semiconductors have Surface State Distribution '3' (see fig 13) at their respective IS interfaces.

(a) T = 450° K.

(b) T = 300° K.

(c) T = 150° K.

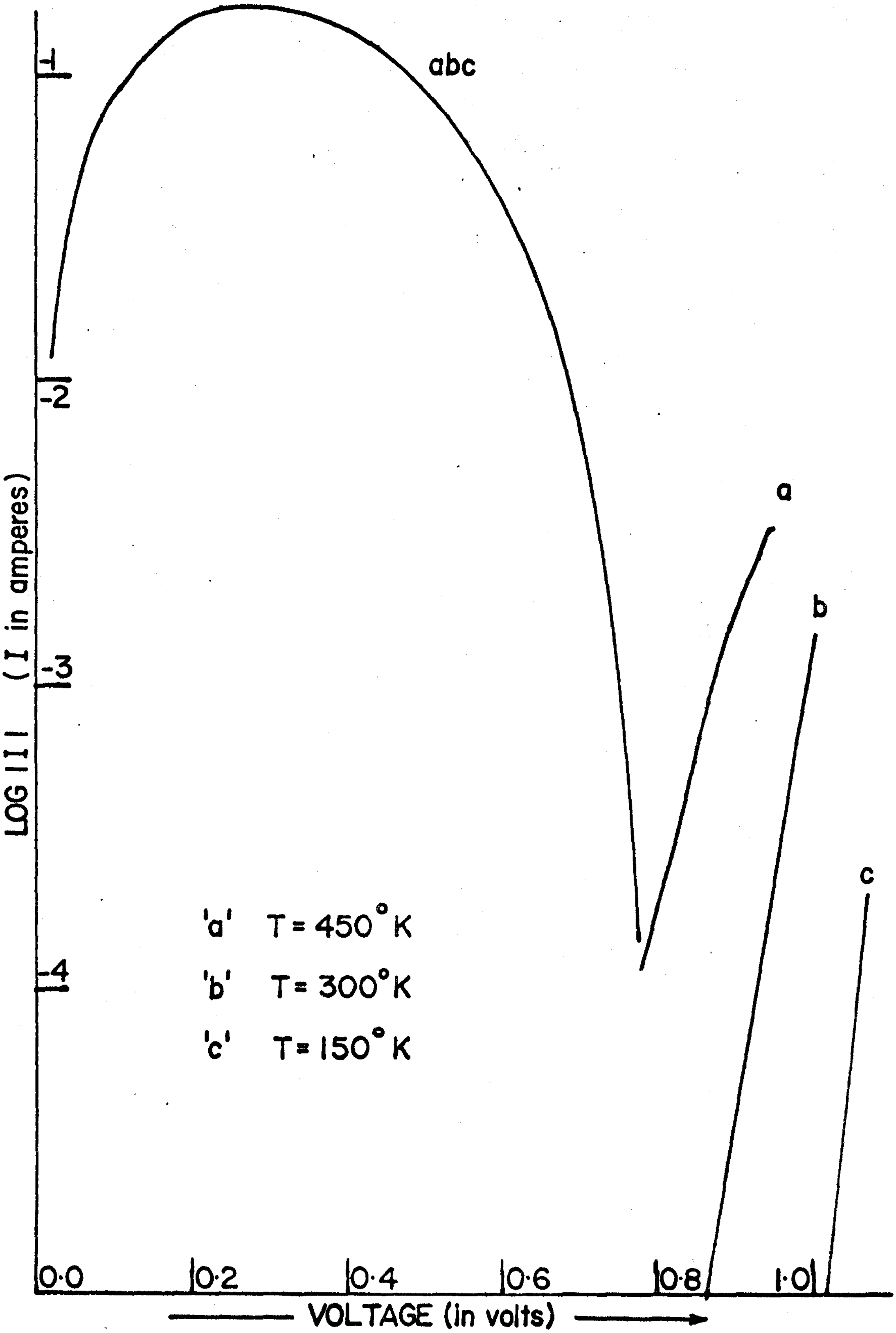
abc
a
b
c
-1
-2
-3
-4
LOG | I | (I in amperes)
'a' T = 450° K
'b' T = 300° K
'c' T = 150° K
0·0
0·2
0·4
0·6
0·8
1·0
VOLTAGE (in volts)

Figure 43

Figure 44 The Effect of Doping on the Negative Resistance Region I-V Characteristics of the Degenerate p-i-n Diode (Both Semiconductors have 'Surface State Distribution 3' (see fig. 13) at their respective IS interfaces. The insulator thickness is 25Å and the temperature is 300°K.) Note that solid circles ∘ denote the no space charge tunnelling case while open circles ∘ denote the space charge tunnelling case.

(a) 'p' type Si, 10^{22}/cc - SiO^2-'n' type Si, 10^{22}/cc.
(b) 'p' type Si, 5 x 10^{21}/cc - SiO^2 - 'n' type Si, 5 x 10^{21}/cc.
(c) 'p' type Si, 10^{21}/cc - SiO^2 - 'n' type Si, 10^{21}/cc.
(d) 'p' type Si, 5 x 10^{20}/cc - SiO^2 - 'n' type Si, 5 x 10^{22}/cc.
(e) 'p' type Si, 10^{20}/cc - SiO^2 - 'n' type Si, 10^{20}/cc.

Note that other semiconductor data pertaining to these degenerate systems is listed in Table 7.

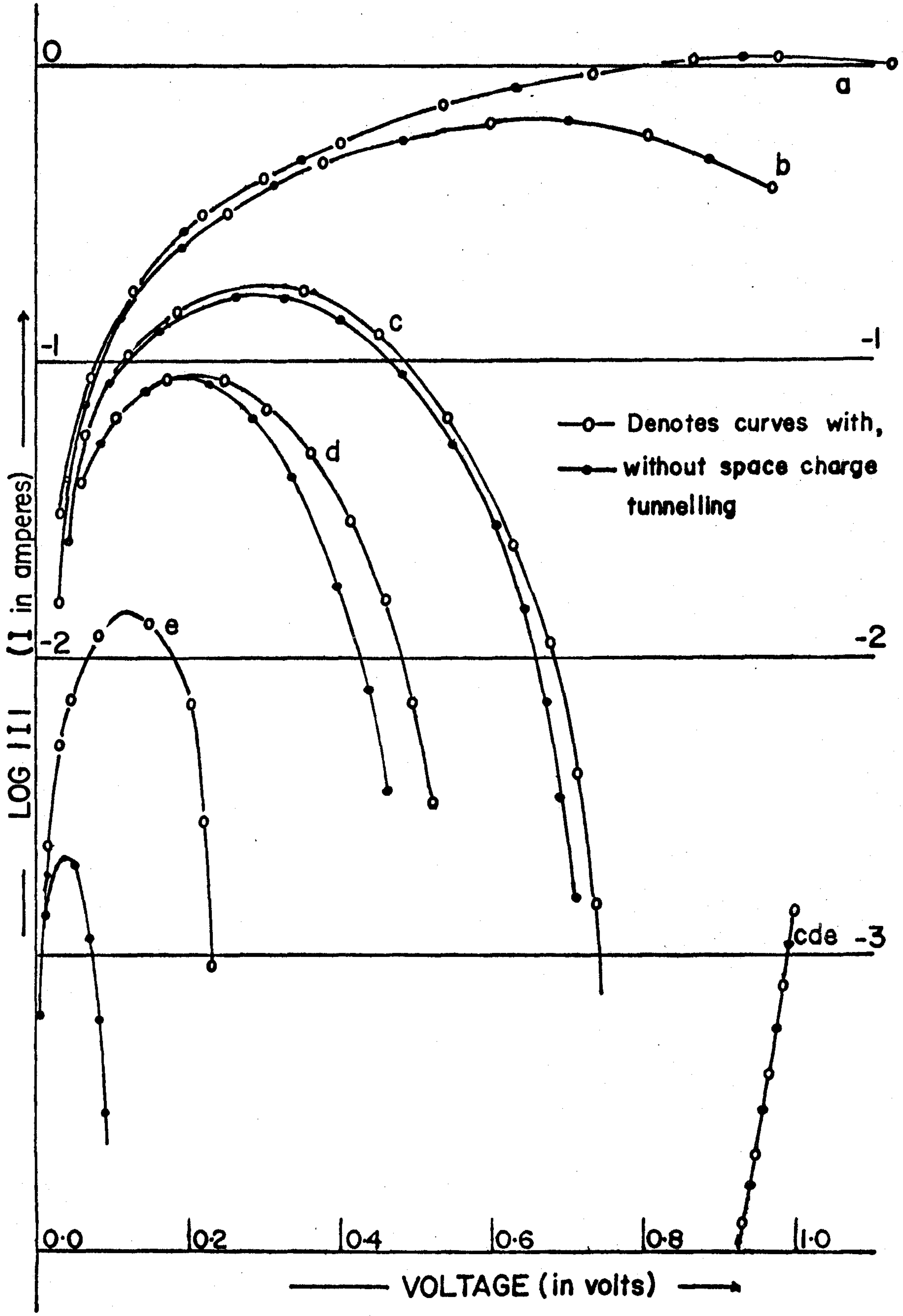
0
-1
-2
-3
a
b
c
d
e
cde
—o— Denotes curves with,
—●— without space charge tunnelling
LOG |I| (I in amperes)
0·0
0·2
0·4
0·6
0·8
1·0
VOLTAGE (in volts)

Figure 44

tunnelling (V'_{-r} and V_{-r}). These values are shown for cases 'a' to 'e' of fig. 44 and for case 'f' with semiconductors 1 and 2 both doped at 10^{19}/cc.

Table 7 shows that in all of these cases the bulk Fermi level was approximately at the dopant impurity energy level. With large values of current due to space charge region tunnelling one would expect a negative resistance region cutoff near V'_{-r} as defined in fig. 41. For cases 'c', 'd', and 'e' of fig. 44 this is just what happens. In each case a well defined negative resistance region is seen. In cases 'a' and 'b' the negative resistance feature is obscured by the interband current, I_{ee}, which becomes dominant at about 1 volt.

For the low doping density case, tabulated as 'f' in Table 7, there was no observed negative resistance region even though a positive value is shown for V'_{-r}. This indicates that there is no significant space charge tunnelling current component at this density. Similarly for the high doping density cases, 'a' and 'b', the curves with (denoted in fig. 44 by open circles) and without (denoted by the solid circles) space charge tunnelling are identicle, again indicating no significant space charge tunnelling contribution. At low impurity densities (eg. case 'f' of Table 7), the additional barrier area presented by the electrostatic potential is large and extends a long distance into the semiconductor (for case 'f', about 5 times the width of the insulator). Hence there is little or no space charge tunnelling. As the doping density

TABLE 7

Semiconductor Data for the Degenerate p-i-n Diode of Figure 44

Case		Impurity Consentration	2σ (See fig. 40)	β (see fig. 40)	Bulk Impurity Energy w.r.t. Fermi Level	Interface Band Bending at Zero Bias	V_{-r} (See fig. 40)	V'_{-r} (see fig. 40)
(a)	S1	p, 10^{22}/cc	.974 eV	.466 eV	-.020 eV	.027 eV	2.027 volts	2.083 volts
	S2	n, 10^{22}/cc	1.069	.513	.020	-.029		
(b)	S1	p, 5 x 10^{21}/cc	.801	.382	-.020	.035	1.501	1.569
	S2	n, 5 x 10^{21}/cc	.729	.349	.020	-.033		
(c)	S1	p, 10^{21}/cc	.410	.225	-.020	.053	.722	.824
	S2	n, 10^{21}/cc	.373	.205	.021	-.049		
(d)	S1	p, 5 x 10^{20}/cc	.353	.168	-.021	.067	.596	.725
	S2	n, 5 x 10^{20}/cc	.320	.153	.022	-.062		
(e)	S1	p, 10^{20}/cc	.154	.0751	-.023	.117	.115	.217
	S2	n, 10^{20}/cc	.139	.0658	.026	-.110		
(f)*	S1	p, 10^{19}/cc	.073	.029	-.025	.205	-.231	.239
	S2	n, 10^{19}/cc	.057	.026	.033	-.255		

* Not shown in fig. 44 as there was no negative resistance region.

increases, the width of the space charge barrier becomes smaller and the space charge tunnelling current increases. However, at very high doping densities (cases 'a' and 'b' of fig. 44 and Table 7), the increase in the allowed range of energy for the I_{he} transition is a very small fraction of the total range. Consequently, the space charge tunnelling contribution to the total current is relatively small and no effect is observed.

In the three cases, 'c', 'd' and 'e' of fig. 44, in which the negative resistance region is well defined, the actual cutoff voltages of the negative resistance region compare fairly closely with those predicted from the zero bias band picture. For the space charge tunnelling cases, V'_{-r} was not as good an estimate of the cutoff voltage, being an overestimate in all cases. There are two reasons why this might be expected. First, the effective area of the semiconductor space charge region barrier varies rapidly with energy so that energies close to E'_{c2} or E'_{v2} (in fig. 41) see a larger space charge barrier. Second, the effect of the WFM k-dependent prefactor (see equation (43)) must be considered. Near the cutoff voltage, I_{he} transitions are to (or from) states very near the band edge. For these transitions the WFM prefactor varies rapidly with energy and causes a more rapid drop in current near the cutoff voltage. This indicates that degenerate p-i-n I-V characteristics might conceivably be able to test the validity of the WKB calculation relative to the WFM calculations outlined in Chapter V. Fig. 45 shows the WKB calculation for the p-i-n case corresponding to 'd' in fig. 44. Unlike the non-degenerate

Figure 45 The Negative Resistance Region of a Typical Degenerate p-i-n Diode With and Without the WFM (Wave Function Matching) Prefactor. (S1 is p-type 5 x 10^{20}/cc. S2 is n-type, 5 x 10^{20}/cc. Both semiconductors have Surface State Distribution 3 (see fig. 13) at their respective interfaces. The insulator thickness is 25 Å and the temperature is 300° K).

(a) With the WFM factor

(b) Pure WKB solution, no WFM factor.

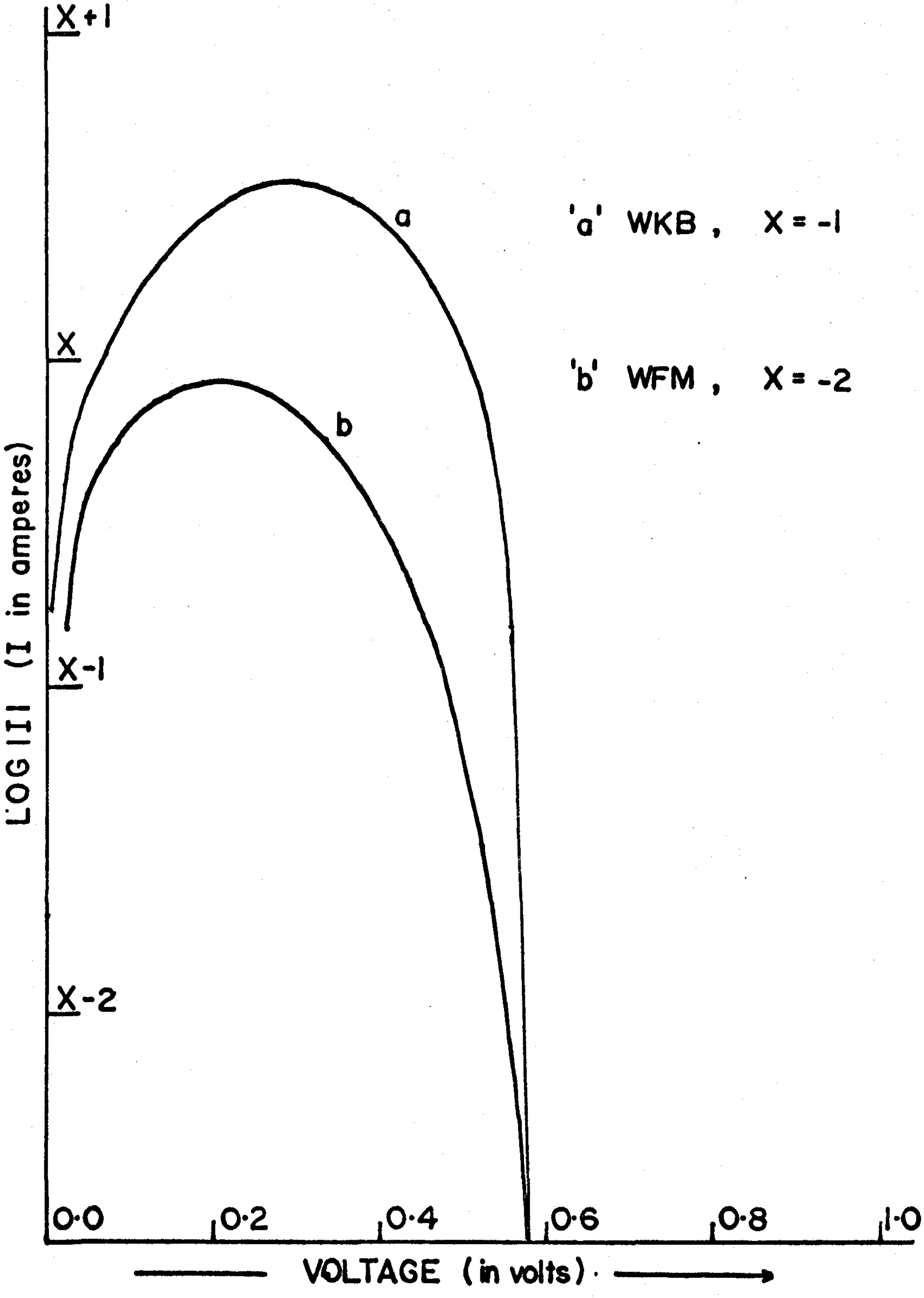
X+1
X
X-1
X-2
LOG |I| (I in amperes)
a
b
'a' WKB , X = -1
'b' WFM , X = -2
0·0
0·2
0·4
0·6
0·8
1·0
VOLTAGE (in volts)

Figure 45

case, where the interband currents are never dominant, there is a marked difference in curve shape.

4. Summary of SIS Tunnelling Features

The SIS I-V tunnelling characteristics are considerably more complex than the corresponding MIS ones. There are essentially two more band-to-band currents (I_{he} and I_{hh}) and three additional band-to-surface state currents (I_{hs}, I_{se} and I_{sh}). This complexity allows for a wide range of characteristics including a negative resistance region in the degenerate p-i-n case where the intraband current I_{he} dominates.

The variation with voltage of $f_{S1} - f_{S2}$, the fraction of bias change which appears across the semiconductor, and the effective tunnelling barrier are the three most important factors for determining the shape of the I-V characteristic. Generally $f_{S1} - f_{S2}$ changes most rapidly in the low voltage region where the Fermi level is somewhere near midband at one or both of the IS interfaces. For low voltages the semiconductor charge density at one or both interfaces is generally small,and a significant fraction of the bias change falls across the semiconductor. This results in a smaller reduction of the effective barrier. In the high voltage region, $f_{S1} - f_{S2}$ approaches unity and all of the change in applied bias goes into a lowering of the barrier. Consequently there is little or no dependence on the details of the semiconductors (or temperature) of the I-V characteristics in that region.

The effect of such factors as space charge tunnelling, image force barrier reduction and the WFM prefactor were generally less important and could be distinguished only in special cases. The understanding of how temperature, doping density, insulator thickness, surface states and fixed charge affect these factors is vital in understanding the I-V behaviour of the various band-to-band and band-to-surface state current components. These effects have been investigated for the technologically important Silicon-Silicon Dioxide-Silicon system. Considerations (such as work function difference) which would arise in other SIS systems have not been investigated and are worth considering in future work.

The special attention paid to the degenerate p-i-n system is warranted by its attractive negative resistance feature. This feature is distinct and large over a wide range of semiconductor doping concentration. It depends on the interband I_{he} current component being dominant in the low voltage region. I_{he} increases from zero at zero bias as $f_{h1} - f_{e2}$ increases. As the voltage increases the allowed energy range of the I_{he} transition decreases so that I_{he} goes through a maximum and then is cutoff once the 'he' transition is forbidden. There will be no negative resistance feature if the cutoff voltage is greater than the voltage at which the current component I_{ee} begins to dominate.

The cutoff voltage is very dependent on the 'degree of degeneracy', ie. how far the band edge is above the Fermi level.

This was largely determined by the assumption of non-localized electron (hole) states for most of the energy range of the combined electron band. Since the assumptions made about the combined band properties have a significant effect on the tunnelling current, it has been suggested(12,60) that tunnelling experiments be used to investigate these properties. In this respect the degenerate p-i-n diode is distinctly more attractive(12) than the degenerate p-n tunnel diode(60) since the interpretation of the experimental results depends on gross features such as whether or not the negative resistance region exists and, if it does, what its cutoff voltage is.

Alternative assumptions are of course possible. It would be interesting, for example, to investigate the effect on the I-V characteristics of varying the 'localized' fraction of the Gaussian impurity band. If this fraction were unity there would be N_{imp} rather than 2 N_{imp} states in the Gaussian distribution with no tunnelling into these states. The conduction 'band edge', in so far as tunnelling is concerned, would be at $E_c - \beta$ to include tunnelling into the tail of the conduction band (see fig. 40). The bulk Fermi level would shift to higher energies since there are fewer states associated with the impurity band. Work is currently being done on this problem.

The controversy(50,61) over the effect of space charge tunnelling could conceivably be resolved in that this effect is quite large in certain instances (case 'e' of fig. 44). Similarly, the validity of the WFM prefactor might be considered as the shape of certain portions of the negative resistance region are sensitive to this factor.

In terms of applications, the use of the negative resistance feature will depend on its reproducibility and on its advantages over other tunnelling systems.* Silicon SIS tunnelling devices of the order of 100 Å are probably attainable by present techniques(59) but would have very low tunnelling currents and might be complicated by an uncharacterized trap region in the oxide.

---

*For example, the insulator barrier reduction of the 'forward diffusion' current, prevalent in the p-n junction tunnel diode.

CHAPTER VII

A.C. TRANSMISSION LINE MODEL FOR THE TUNNELLING SIS DEVICE

1. Introduction

Measurements of the d.c. I-V characteristics are not the only useful measurements which can be made on a tunnelling SIS (or MIS) device. The a.c. conductance and capacitance measurements can still be made. The a.c. C-V and G-V curves can be expected to be modified in a manner which sheds more light on the tunnelling problem. Extra a.c. current paths are now available to carriers at the interface. These paths are represented by resistive connections between the two bands (or between a surface state and a band) involved. This is illustrated in fig. 46 where R_{ee}, R_{eh}, R_{he} and R_{hh} represent the resistance to a.c. band-to-band currents and R_{es} and R_{hs} represent the resistance to a.c. current between the carrier bands of semiconductor 1 (SI) and a surface state on the interface of semiconductor 2 (S2).

2. Definition of the a.c. Tunnelling Resistances

The a.c. band-to-band tunnelling resistances and the a.c. band-to-surface state resistances can be defined simply using the derivative of the d.c. I-V characteristics defined in Chapter V. That is,

Figure 46 Modification of the SIS A.C. Transmission Line Model for Low Values of D.C. Tunnelling Current (No Space Change Tunnelling).

(a) Addition of resistive paths, R_{ee}, R_{eh}, R_{he} and R_{hh}, for the a.c. band-to-band currents.

(b) Addition of a surface state at interface 2 (Node S_i) with band-to-surface state a.c. resistances R_{eh} and R_{he}. Elements C_{ox}, G_{PS}, G_{NS} and C_S are part of the thick oxide model shown in fig. 7. Nodes P1, K1, and N1 label the hole, displacement and electron current nodes on the interface of semiconductor 1. C1 labels the back contact node of semiconductor 1. P2, K2, N2 and C2 are the corresponding nodes of semiconductor 2.

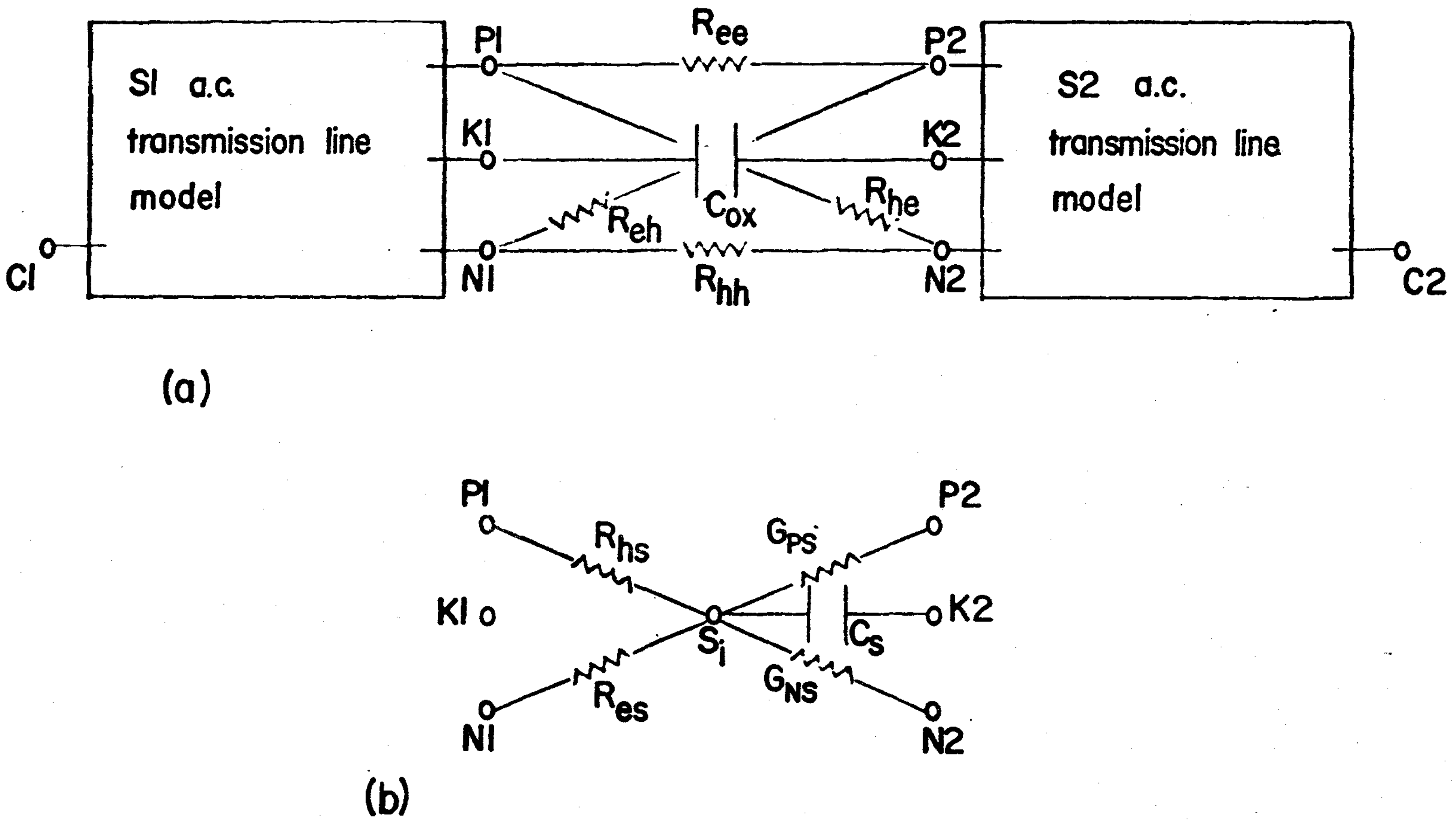
S1 a.c. transmission line model
S2 a.c. transmission line model
C1
C2
P1
K1
N1
P2
K2
N2
R_{ee}
R_{hh}
R_{eh}
R_{he}
C_{ox}
(a)
P1
K1
N1
P2
K2
N2
R_{hs}
R_{es}
G_{PS}
G_{NS}
C_S
S_i
(b)

Figure 46

$$R_{ab} = \frac{dI_{ab}}{dV_{dev}} \frac{dV_{dev}}{dV_{ox}} \Bigg|_{V_{ox}, V_{dev}} \qquad (53)$$

where V_{dev} is the applied bias and V_{ox} is the d.c. the part of the d.c. bias which falls across the insulator (oxide). 'a' and 'b' run through the band labels 'e', 'h' and 's'.

dI_{ab}/dV_{dev} is simply evaluated at V_{dev} while dV_{dev}/dV_{ox} is available from the d.c. bias solution given in Chapter II.

3. Problems Involved in Obtaining an Accurate a.c. Solution

The model given in fig. 46 is applicable for small a.c. signal voltages over which the a.c. tunnelling resistance parameters are constant. For larger signals a first order correction term can be added to each of the resistances in the form of an active element (current source) which compensates for the fixed R_{ab} values evaluated at the d.c. bias voltage. The model will give accurately all the small signal a.c. effects provided an accurate d.c. solution is available. In the thick oxide case, with no light illumination, this solution was a straightforward solution of Poisson's equation. For low d.c. tunnelling currents this solution is still more or less valid.

For higher currents a self consistent solution of the d.c. quasi Fermi level shifts (as a function of distance from the interface) for each of the bands is required. This problem is not an impossible one given modern computing facilities. It does, however, require lengthy iterative procedures which prohibit solutions of great accuracy. For the MIS device it is suggested that approximate solutions in the semiconductors be sought for the high current range, where it would be possible to fix the d.c. quasi fermi level for the semiconductor minority carrier band precisely opposite the metal conduction band. A more complicated procedure is described by Clarke(47) in his study of non-equilibrium MIS tunnelling in which a minority carrier band charge density is assumed. This density (as a function of distance from the interface) will give a non zero d.c. quasi Fermi level at points in the semiconductor where it differs from the thermal equilibrium solution of Poisson's equation.

4. Summary

The difficulties discussed in the previous sections exist in addition to the question of how to properly solve the d.c. tunnelling problem. They amount to nothing more than a solution of the non-equilibrium problem in the semiconductor which, in principle, can be solved with reasonable accuracy. This solution is required in interpretting any high current d.c. tunnelling problem involving semiconductors. Given a reasonably accurate non-equilibrium d.c. solution, the exact solution of the a.c. transmission line model can be utilized to interpret the extra data available in the a.c. admittance characteristics of tunnelling MIS and SIS structures.

CHAPTER VIII

CONCLUSION

The work presented in this thesis has been concerned with some fundamental problems in semiconductor physics, particularly as applied to the important class of thin-film, insulator-dominated semiconductor device structures.

The problem considered in Chapter II was merely the solution of Poisson's equations as a function of applied bias. The solution of this problem is the starting point of any general semiconductor problem and considerable effort was expended in formulating a general program, of prespecified accuracy, applicable to any bandgap material. To date this generality and accuracy have been utilized(47,59) in improved analysis of several experimental semiconductor systems. In addition, Chapter II presents the first solutions for the low frequency SIS (semiconductor-insulator-semiconductor) system(1) and predicts one or two unusual features which may be useful from the point of view of device applications.

The exact solution of the small signal a.c. transport equations for band gap materials is discussed in Chapter III. The system of nonlinear differential equations is solved using Sah's(2) equivalent transmission line model. Surface states, SRH centre and impurity band frequency response are included. Furthermore, the model is still exactly soluble in the non-equilibrium case with the addition of active elements in the transmission line. This solution is both more convenient, more accurate and more general than the lumped model equivalent circuits approaches previously required(17,4,21,35). In the lumped-model equivalent-circuit approach, different models must be used in different voltage regions and for 'high' and 'low' generation-recombination rates. In each of these models there is at least one 'extra' parameter which requires experimental fit. In addition, the models do not apply in intermediate ranges, nor do they predict such features such as the frequency response of the impurity band at low temperature.

The exact solution, on the other hand, needs no experimental definition of 'extra' parameters and can, therefore, be used to predict device behaviour over ranges and combinations of device variables which would be otherwise prohibitive. The second advantage of an exact solution of the a.c. transport equations lies in the ability to use comparison with experiment to investigate the basic physical parameters and assumptions used in the formulation of the equations themselves. While the first application is attractive to device oriented research, the second is of greater interest to the researcher who is investigating such questions as impurity band and SRH centre effects, surface state characterization, or high doping density effects. For this reason a number of a.c. C-V (capacitance-voltage) characteristics are given in Chapter III for the simpler MIS case. It is pointed out, for example, that improved analysis of surface states can be obtained by separating the conductance contribution of the semiconductor space charge region from that of the surface states. Note also that a frequency dependent dopant impurity band is calculated for the first time.

The a.c. solution was applied to give the first calculation of the frequency dependent complex admittance characteristics of the SIS device. The characteristics are given for typical SIS devices as a function of temperature, doping density, SRH centre density, fixed oxide charge and surface states. The calculations predict an interesting device possibility, namely a peaked high frequency C-V response. This response has recently been observed and explained(59) using the a.c. solution of Chapter IV.

Chapters V and VI deal with the important problem of tunnelling current in the SIS device. This problem was investigated first by Shewchun(12) where some arguments are given for the existance of a negative resistance region in the degenerate p-i-n device. Actual calculation of the four band-to-band current components and the four band-to-surface state current components are given in Chapter VI for the first time in both the degenerate and the non-degenerate structures.

The tunnelling equations are derived in Chapter V using methods developed (or suggested) for the MIS tunnelling case. These equations thus can be applied to the MIS tunnelling problem as a special case. The tunnelling solution is not highly accurate when contrasted with the completeness and accuracy of the d.c. bias solution of Chapter II and the a.c. solution of Chapters III and IV. It relies on an independent particle solution and on the effective mass formulation, both weak points(49) in tunnelling theory. The WKB formalism is also known to be inadequate in the vicinity of the barrier. Nonetheless the approach has the advantage of being readily soluable and is known to predict reasonably well the I-V characteristics of the simpler MIS tunnelling systems.

I-V characteristics are given for different temperatures, barrier thickness and doping densities. Fixed charge and surface states are also considered. In the degenerate p-i-n device the negative resistance region is observed to be very dependent on doping density and dependent to a lesser extent on space charge region tunnelling in the semiconductors.

Chapter VII is included as an indication of how the d.c. tunnelling solution and the a.c. small signal admittance solution could be used to predict the effect of d.c. tunnelling current on the a.c. admittance characteristics. With a sufficiently accurate solution of the non-equilibrium d.c. problem (simultaneous solution of the d.c. transport equations and Poisson's equation), experimental a.c. admittance measurements could be used to advantage in investigating the complicated tunnelling problem.

APPENDIX 1

Semiconductor Data

(a) Semiconductor Data (Nominally Silicon*)

ε_S, semiconductor dielectric constant = 11.7 ε_o

ε_I, insulator dielectric constant = 3.8 ε_o

t, oxide thickness = 1000 Å (The insulator is SiO^2.)

Impurity band doping density is designated on the some figures.

For example in Fig. 19,

P-17 is P-type, $10^{17}/cm^3$;

5N-15 is N-type, $5 \times 10^{15}/cm^3$

Metal work function** = 3.2 eV; Semiconductor work function = 3.2 eV.

E_{gap} (T = 300°K) = 1.121 eV*

N-type donor level = 1.079 eV above valence band.

P-type acceptor level = .042 eV above valence band.

m_e = electron effective mass* = 1.180 with a resultant

N_c (at T = 300°K) = $3.207 \times 10^{19}/cm^3$

m_h = hole effective mass* = .810 with a resultant

N_v (at T = 300°K) = $1.824 \times 10^{19}/cm^3$

μ_e, electron mobility = .04 m/volt/sec, μ_h = .02 m/volt/sec.

(b) Surface State Data

$$\sigma^p\theta_p = 1.11 \times 10^{-14}\ m^3/sec.$$

$$\sigma^n\theta_n = .921 \times 10^{-14}\ m^3/sec.$$

---

*Data has been taken from curves given in reference 29.

**Figs. 9 to 15 are uncorrected for work function effect. All other figures are corrected. Comparing figs. 15 and 16, this correction is seen to be about 1 volt.

(c) SRH Data

$$\sigma^p\theta_p = \sigma^n\theta_n = 5 \times 10^{-13}\ m^3/sec$$

(d) Temperature Data

$$E_{gap}(T) = E_{gap}(300°K) - (T-300) \times 2.8 \times 10^{-4}*.$$

All other energies are scaled from the T = 300°K data above by the factor $E_{gap}(T)/E_{gap}(300°K)$.

With the same effective mass values, N_c and N_v are $(T/300)^{3/2}$ times the 300°K values.

(e) Data for the Low Temperature Tests

T	m_e	m_h	N_c	N_v	E_{gap}
50°K	1.065	.640	1.87×10^{18}/cc	8.72×10^{17}/cc	1.178 ev
63°	1.065	.650	2.65×10^{18}	1.26×10^{18}	1.165
88°	1.065	.660	4.37×10^{18}	2.13×10^{18}	1.163
112°	1.065	.669	6.27×10^{18}	3.12×10^{18}	1.159

Mobility data as a function of doping density N_{imp} and electric field $\underline{E}$.

$$\mu_1 = (\mu_{max} - \mu_{min})/(1 + N_{imp}/N_{ref})^{\alpha} + \mu_{min} \qquad (A1)$$

$$\mu_2 = \mu_1/(1 + (\underline{E}/\underline{E}_{crit})^{\beta})^{1/\beta} \qquad (A2)$$

with reference 27 giving

μ^e_{max} = .0133 m/(volt sec) μ^e_{min} = .0065 m/(volt sec)

μ^h_{max} = .0495 m/(volt sec) μ^h_{min} = .00477 m/(volt sec)

$N^e_{ref} = 8.6 \times 10^{20}/m^3 \qquad N^h_{ref} = 6.3 \times 10^{20}/m^3$

$\alpha^e = .720, \ \beta^e = 2 \qquad \alpha^h = .760, \ \beta^h = 1$

$\underline{E}^e_{crit} = 8.0 \times 10^5 \ v/m \qquad \underline{E}^h_{crit} = 1.95 \times 10^6 \ v/m$

APPENDIX 2

Definition of Transmission Line Elements

In this appendix equations for the parameter values of the transmission line shown in fig. 7 will be listed. To allow for Fermi statistics, the parameters of the basic or 'bare' transmission line have been changed in form from the original formulation given by Sah[2,21]. For this reason a few comments are included which apply to the elements shown in fig. 7(a).

In the semiconductor, charge is transported from one position to another by the two band currents and by the displacement current. The a.c. current flows, in the semiconductor conduction and valence bands, are given in equation (24). In the model, the voltage between nodes j and j + 1 divided by Δx_j corresponds to ∇v. Hence, to have the model correctly reflect the a.c. band currents, requires conductances G_{P_j} and G_{N_j} to be defined as the coefficient of $(v_{j+1} - v_j)$ as indicated in equation (24). Similarly, to have an a.c. displacement current flow in the model of $\epsilon_s \nabla \dot{v}_k$ requires the definition of C_{K_j} as $\epsilon_s/\Delta x_j$ Clearly equation (22) for the total current as a function of x is satisfied provided that $v_k(x,t)$ is defined as the a.c. potential as in equation (21) and v_n and v_p are taken to be the a.c. potentials of the electron and hole bands as measured from the static potential due to the d.c. bias.

The evaluation, at a fixed x, of the a.c. charge stored in each of the bands depends on the difference from the instantaneous a.c. semiconductor potential, $v_k(x,t)$, of the a.c. voltage of each band. This charge, $\Delta\rho_{band}$, is equal to $\frac{d\rho}{dV}\,\Delta V$ where ΔV is small and given by $v_{band} - v_k$. The mathematical statement of this condition is given by equation (23), and, when the time derivative of both sides is taken, is equivalent to conservation of charge. In our model, to satisfy conservation of charge thus requires the definition of C_{N_j} and C_{P_j} as $C_n(x)\ \Delta x_j$ and $C_p(x)\ \Delta x_j$ where C_n and C_p are defined* in equation (24).

To prove that the model will give a v_k satisfying equation (21) is now all that is required to show that the model is self consistent and obeys all the equations of the real system. The charge stored on each plate of C_{K_j} is just $C_{K_j}\,(v_k(x_{j+1})-v_k(x_j))$ and the charge stored on each plate of $C_{K_{j-1}}$ is $C_{K_{j-1}}\,(v_k(x_j)-v_k(x_{j-1}))$. The difference in these two a.c. charge quantities must equal the negative sum of the a.c. charge on capacitors $C_{P_j}$and C_{N_j}. Hence, recognizing $(v_k(x_{j+1})-v_k(x_j))/\Delta x_j$ as ∇v_k, the equivalent mathematical statement is

$$\epsilon_s \left\{ \nabla v_k(x_j)-\nabla v_k(x_{j-1}) \right\} = -\delta\rho(x,t)\ \Delta x_j$$

where $\epsilon_s/\Delta x_j$ has been inserted for C_{K_j}. This result corresponds to equation (21) as required, ie. $\nabla^2 v_k(x,t) = -\delta\rho(x,t)$.

For the parameter values of the model segments in figs. 7(b) to (d), the equations are taken from reference 32 where a complete derivation of the single level SRH centre and the single level surface state models are given. A somewhat briefer derivation can also be found in reference 21. Note that the equations for the non-equilibrium

---

In Sah's original formulation, $\frac{dN}{dV}$ is written assuming Boltzmann statistics as $-\frac{e}{kT}\,N$ and $\frac{d\rho}{dV}$ as $+\frac{e}{kT}\,P$.

case of fig. 7(d) assume that the ratio of capture to emission cross sections is unchanged for small deviations from the equilibrium condition.*

In fig. 7(a)

$$G_{P_j} = e\mu_p P(x_j)/\Delta x_j \qquad G_{N_j} = e\mu_n N(x_j)/\Delta x_j$$

$$C_{P_j} = - e\,\Delta x_j \left.\frac{dP}{dV}\right|_{V=V(x_j)}, \qquad C_{N_j} = - e\,\Delta x_j \left.\frac{dN}{dV}\right|_{V=V(x_j)}$$

$C_{K_j} = \epsilon_s/\Delta x_j$ where Δx_j is the j^{th} slice width.

In fig. 7(b) for the j^{th} semiconductor slice:

$$G_{PR} = \Delta x_j P(x_j) N_{R_i} f_i^n \sigma_i^p \theta_p e^2/kT, \quad C_{R_i} = \Delta x_j N_{R_i} f_i^n f_i^p e^2/kT$$

$$G_{NR_i} = \Delta x_j N(x_j)\, N_{R_i} f_i^p \sigma_i^n \theta_n e^2/kT$$

where N_{R_i} is the SRH density of the i^{th} trap level,

f_i^n and f_i^p its electron and hole Fermi functions,

σ_i^n and σ_i^p its electron and hole capture cross sections,

with θ_n and θ_p the electron and hole thermal velocities.

In fig. 7(c) at the IS interface;

$$G_{PS_i} = P(x=0) N_{S_i} f_i^n \sigma_i^p \theta_p e^2/kT, \quad C_{S_i} = N_{S_i} f_i^n f_i^p e^2/kT$$

$$G_{NS_i} = N(x=0) N_{S_i} f_i^p \sigma_i^n \theta_n e^2/kT$$

where N_{S_i} is the density of the i^{th} surface state band,

and σ_i^n and σ_i^p its electron and hole capture cross sections.

---

* This assumption is thought to be valid except for electric fields high enough to deform the potential well associated with the SRH centre.

In fig. 7(d) for the nonequilibrium condition and a single SRH band*,

$$g_{PR} = (e^2/kT) f_R^n \, R_L \, \Delta x, \quad g_{NR} - (e^2/kT) f_R^p \, R_L \, \Delta x$$

where R_L is a measure of the excess carrier recombination rate per unit volume through the SRH centre.

Reference 21 gives R_L

$$R_L = \frac{N_R \, \sigma_R^n \, \sigma_R^p \, \theta_n \, \theta_p \, (P(x_j)N(x_j) - n_i^2)}{\sigma_R^n \, \theta_n \, (N(x_j)+n_1) + \sigma_R^p \, \theta_p \, (P(x_j)+p_1)} \qquad \text{(A3)}$$

where n_1 and p_1 are the electron and hole densities when the Fermi level is at the SRH energy. Note $PN-n_i^2$ will be zero in thermal equilibrium.

$$g_{PK} = J_p \, e/kT \qquad\qquad g_{NK} = J_n \, e/kT$$

where J_p and J_n are the d.c. current flows, normally zero in thermal equilibrium but given in the non-equilibrium case by

$$\vec{J}_p = -e \, \mu_p \, P \, \nabla V - e \, D_p \nabla P$$

$$\vec{J}_n = -e \, \mu_n \, N \, \nabla V + e \, E_p \nabla N \qquad \text{(A4)}$$

where D_n and D_p are electron and hole diffusion constants and $-\nabla V$ the electric field.

---

*All band densities and Fermi functions include the quasi Fermi level shift, as for example, in equation (25) in Chapter III.

REFERENCES

1. V. A. K. Temple and J. Shewchun, IEEE Trans. ED-18, 235 (1971).
2. C. T. Sah, R. F. Pierrot, A. B. Tole, SEE 12, 681 (1969).
3. V. A. K. Temple and J. Shewchun, paper submitted to Solid-State Electronics, November, 1971 entitled "The Exact Frequency Dependent Complex Admittance of the MOS Diode etc." (In Press)
4. K. Lehovec and A. Slobodskoy, SSE 7, 59 (1964).
5. J. R. Hauser, M. A. Littlejohn, SSE 11, 667 (1968).
6. E. O. Kane, J. Phys. Chem. Solids, Vol. 1, 82 (1958).
7. L. Kleinman and J. C. Phillips, Phys. Rev. 118, 1153 (1961).
8. G. Dresselhaus, A. F. Kip, C. Kittel, Phys. Rev. 98, 368 (1955).
9. A. S. Grove, B. E. Deal, E. H. Snow and C. T. Sah, SSE 8, 145 (1965).
10. A. Geotzberger, V. Heine, E. H. Nicollian, Appl. Phys. Letters 12, 95 (1968).
11. P. V. Gray, D. M. Brown, Appl. Phys. Letters 8, 31 (1966).
12. J. Shewchun, JAP 38, 35 (1967).
13. R. H. Kingston and S. F. Neustadter, JAP 26, 718 (1955).
14. C. E. Young JAP 32, 329 (1961).
15. G. C. Dousmanis and R. C. Duncan Jr., JAP 29, 1627 (1958).
16. C. Goldberg, SSE 7, 593 (1964).
17. E. H. Nicollian and A. Goetzberger, Bell Syst. Tech. J. 46, 1055 (1967).
18. C. N. Berglund, IEEE Trans. ED-13, 701 (1966).
19. D. M. Brown and P. V. Gray, J. of the Electrochem. Soc. 115, 760 (1968).

20. L. M. Terman, Solid-State Electronics 5, 285 (1962).

21. C. T. Sah, Tech. Report #3, Electrical Eng. Res. Lab, U. of Illinois (1967).

22. R. N. Hall, Phys. Rev. 83, 228 (1951).

23. W. Shockley and W. T. Reed, Phys. Rev. 87, 835 (1952).

24. R. F. Pierret and C. T. Sah, Solid-State Electronics 13, 269 (1970).

25. D. D. Kleppinger and F. A. Lindholm, Solid-State Electronics 14, 199 (1971).

26. P. V. Gray and D. M. Brown, App. Phys. Lett. 13, 257 (1968).

27. D. M. Coughey and R. E. Thomas, Proc. IEEE Lett. 55, 2192 (1967).

28. N. S. Clayton, private communication, "Measurement and Behaviour of Discrete MOS Surface States", Can. Westinghouse Ltd., Hamilton, Ontario, Canada.

29. D. H. Barber, Solid-State Electronics 10, 1039 (1967).

30. D. D. Kleppinger and D. A. Lindholm, Solid-State Electronics 14, 407 (1971).

31. J. Dresner and F. V. Shollcross, J. of Appl. Phys. 34, 2390 (1963).

32. C. T. Sah, IEEE Proc. 55, 654 (1967).

33. C. T. Sah, IEEE Proc. 55, 672 (1967).

34. J. Shewchun and V. A. K. Temple, paper submitted to J. of Appl. Phys., December 1971 entitled "Exact Frequency Dependent Complex Admittance of the SIS Diode ... etc."

35. K. Lehovec, A. Slobodskoy and J. L. Sprague, Phys. Stat, Sol. 3, 447 (1963).

36. L. Esaki, Phys. Rev. 109, 603 (1958).

37. E. O. Kane, J. of Phys. Chem. Solids 12, 181 (1959).

38. W. A. Harrison, Phys. Rev. 123, 85 (1961).

39. K. H. Gundlach, Solid State Electronics 9, 265 (1966).

40. J. G. Simmons, J. Appl. Phys. 34, 265 (1963).

41. J. W. Gadzuk, J. Appl. Phys. 41, 286 (1970).

42. C. Caroli et al, J. Phys. C: Solid-St. Phys. 4, 2598 (1971).

43. P. V. Gray, Phys. Rev. 140, A179 (1965).

44. J. Shewchun, A. Waxman and G. Warfield, Solid State Electronics 10, 1165 (1967).

45. L. B. Freeman and W. E. Dalke, Solid State Electronics 13, 1433 (1970).

46. C. B. Duke, "Tunnelling Phenomena in Solids", Plenum Press (1969).

47. R. Clarke and J. Shewchun, Solid State Electronics 14, 957 (1971).

48. D. R. Fredkin and G. H. Wannier, Phys. Rev. 128, 2054 (1962).

49. T. E. Feuchtwang, paper manuscript entitled "Generalized WKB Approximation etc" (private communication) Physics Dept., Penn. St. Univ., U. S. A.

50. D. J. BenDaniel and C. B. Duke, Phys. Rev. 152, 683 (1966).

51. L. Esaki and P. Styles, Phys. Rev. Letters 16, 1108 (1966).

52. L. L. Chong, P. J. Styles and L. Esaki, J. Appl. Phys. 38, 4440 (1967).

53. H. H. Cohen, L. M. Falicov and J. C. Phillips, Phys. Rev. Letters 8, 316 (1962).

54. L. V. Keldysk, Sov. Phys. JETP 20, 1018 (1965).

55. Y. Takeuti and H. Funada, J. Phys. Soc. of Japan 20, 1854 (1965).

56. R. T. Shuey, Phys. Rev. 137, A1268 (1965).

57. R. Stratton, J. Chem. Phys. Solids 23, 1177 (1962).

58. S. R. Pollack and C. E. Morris, J. Appl. Phys. 35, 1503 (1964).

59. J. Shewchun, R. Clarke and V. A. K. Temple, "Experimentally Observed Admittance Properties of the SIS Diode" IEEE Trans. on Electron Devices,(In Press.)

60. V. L. Bonch-Bruyevitch, "Electronic Theory of Heavily Doped Semiconductors" American Elsevier Publishing Co., New York.

61. R. Putman and R. Van Overstraeten, paper manuscript entitled "Influence of Band-Bending on the Tunnelling Probability in MIS Structures" (private communication), Electrical Engineering Department, Kardinaal Mercierlaan 94, 3030 Heverlee, Belgium.

62. T. N. Morgan, Phys. Rev. 139, A343 (1965).